Vibrational Imaging at the Nanoscale: Surpassing the Diffraction Limit Using Tip-Enhanced Raman Spectroscopy

Farshid Pashaee
The University of Western Ontario

Supervisor
Francois Lagugné-Labarthet
The University of Western Ontario

Graduate Program in Chemistry
A thesis submitted in partial fulfillment of the requirements for the degree in Doctor of Philosophy
© Farshid Pashaee 2015

Follow this and additional works at: https://ir.lib.uwo.ca/etd

VIBRATIONAL IMAGING AT THE NANOSCALE: SURPASSING THE
DIFFRACTION LIMIT USING TIP-ENHANCED RAMAN
SPECTROSCOPY

(Thesis Format: Integrated Article)

by

Farshid <u>Pashaee</u>

Graduate Program in Chemistry

A thesis submitted in partial fulfillment of

the requirements for the degree of

Doctor of Philosophy

The School of Graduate and Postdoctoral Studies
The University of Western Ontario
London, Ontario, Canada

Abstract

A deep understanding of the chemical composition of surfaces, interfaces or nanoscale structure with a high spatial resolution is an important goal in nanoscience and nanotechnology. Structural information can be collected using a variety of high spatial resolution techniques such as atomic force microscopy (AFM), scanning tunneling microscopy (STM), scanning electron microscopy (SEM), or transmission electron microscopy (TEM). Nevertheless, these methods do not offer molecular information such as vibrational spectroscopy techniques that allow one to collect molecular or lattice vibrations yielding to a precise picture of the molecular interactions in bulk materials as well as in surfaces and interfaces. Unfortunately optical spectroscopy techniques are limited in terms of spatial resolution and sensitivity due to the poor signal/noise ratio of the localized measurement.

Surface- and tip-enhanced Raman spectroscopy (SERS and TERS) are advanced spectroscopic techniques, which are becoming widely used and show a great potential for the structural characterisation of biological systems. Surface-enhanced spectroscopy (SERS) was developed to improve the sensitivity of the chemical measurements by using rough silver or gold surfaces. The challenge of the simultaneous improvement of the spatial resolution and sensitivity was addressed by combining high resolution optical microscopy with the high sensitivity of surface-enhanced spectroscopy and was termed tip-enhanced Raman spectroscopy (TERS).

In this thesis, gap-mode TERS is developed for the study of a variety of materials. TERS is used in conjunction with gold nanoplates to serve as an ultraflat substrate that can possibly be functionalized. TERS investigation of monolayers adsorbed onto gold nanoplates such as alkoxy substituted azobenzene thiol and 4-nitrothiophenol is conducted. The monolayer is probed with a silver

coated AFM tip in order to obtain the largest electromagnetic field enhancement and the effect of the excitation (linearly or radially polarized) is conducted. TERS is also used to probe graphene flakes and differentiate the edges of a few-layer graphene flakes with a spatial resolution better than 20 nm. Last, TERS was used to investigate single DNA molecules deposited onto gold nanoplates. The DNA, cDNA and pure plasmid were investigated with TERS probing the distribution of nucleobases at a specific location with a spatial resolution which was, in the best conditions below 10 nm.

Keywords

Dedication

To my wife and my family

Co-Authorship Statement

The following thesis contains material from previously published manuscripts. Dr. François Lagugné-Labarthet was the corresponding author on the presented papers and was responsible for the supervision of Farshid Pashaee over the course of his studies.Farshid Pashaee was the primary author of the published papers presented in Chapters 4, 5 and 6. He was responsible for the majority of the experimental work in these papers as well as the writing and revision for all drafts, including final manuscripts. Some data were jointly acquired and analyzed by co-authors as summarized below:

In **Chapter 3**, P. Gobbo was involved in the synthesis of Gold nanoplate and purification of them. The purification of gold nanoplates were done in the research laboratory of Dr. M. Workentin in chemistry department at Western university.

In **Chapter 4**, 2-[4-(4-Decyloxylphenylazo)phenyl]ethyl thiol was synthesized in Dr. E. R. Gillies research group in chemistry department at Western university.
Pashaee F.; Hou R.; Gobbo P.; Workentin M.; Lagugne-Labarthet F.; "Tip-Enhanced Raman Spectroscopy of Self-Assembled Thiolated Monolayers on Flat Gold Nanoplates Using Gaussian-Transverse and Radially Polarized Excitations" *J. Phys. Chem. C,* 2013,117, 15639. Front cover

Graphene flakes in **Chapter 5** were synthesized by Dr. F. Sharifi in research laboratory of Dr. G. Fanchini in the department of Physics and Astronomy at Western university.
Pashaee F.; Sharifi F.; Fanchini G.; Lagugné-Labarthet F.; "Tip-Enhanced Raman Spectroscopy of few-layer Graphene platelets on ultraflat Gold Nanoplates" *Phys. Chem. Chem. Phys,* 2015, 17, 21315.

Additional collaborations were done in **Chapter 6** with Dr. S.S.G. Ferguson, Dr. F. Caetano for purification of DNA samples in Physiology and Pharmacology

at Western University as well as Dr. M. Tabatabaei in his enthusiastic involvement during the DNA project.

Pashaee F.; Tabatabaei, M.; Caetano F.A.; Ferguson S.S.; Lagugné-Labarthet F.; "Tip-Enhanced Raman Spectroscopy: plasmid-free vs. plasmid embedded-DNA" 2016, *in preparation*

Acknowledgments

I would like to express my special appreciation and thanks to my supervisor: Dr. François Lagugné-Labarthet. I would like to thank you for encouraging my research and for allowing me to grow as a research scientist. Also I am also very grateful to Dr. Mark S. Workentin and Dr. Giovanni Fanchini for their scientific advice and knowledge and many insightful discussions and suggestions.

Many thanks are extended to all researchers at Dr. Stephen Ferguson's research group at Robarts Research Institute in particular Dr. Fabiana A. Caetano.

I would like to thank the staff from Nanofabrication facility at the University of Western Ontario and my dear colleagues Dr. Nastaran Kazemi-Zanjani for technical support in TERS setup and Dr. Mohammadali Tabatabaei, Pierangelo Gobbo, Dr. Faranak sharifi and Renjie Hou, for the preparation of my samples and TERS probes.

I would also like to special thank my parents for the support, they provided me through my entire life and in particular, I must acknowledge my wife, without her love, encouragement and editing assistance, I would not have finished this thesis.

Table of Contents

List of Tables

List of Figures

List of Abbreviations, Symbols and Nomenclature

α	Polarizability of a molecule
β	Bending mode
λ	Wavelength of light
ν	Stretching mode/vibrational level
θ	Angle of incidence
Δx	Optical diffraction limit
3D	Three dimensional
4-NTP	4-nitrothiophenol
AFM	Atomic force Microscope
A	Adenine
AC	Alternating current
APTMS	3-Aminopropyl trimethoxysilane
CCD	Charge-coupleddevice
C	Cytosine
CTAB	Cetyl trimethylammonium bromide
D	Diameter of a nanosphere
DC	Direct current
DNA	Deoxyribonucleic acid
E	Electric field
Ef	Enhancement factor
G	Guanine
LSPR	Localized surface plasmon resonance
LC	Liquid crystal
MEF	Metal-enhanced fluorescence
n	Index of refraction
$N.A$	Numerical aperture of an microscope objective
NRS	Normal Raman scattering
NMR	Nuclear magnetic resonance
PALM	Photo activated localization microscopy
PRET	Plasmon resonance energy transfer
PVP	Polyvinylpyrrolidone
Ps	Picosecond
R_{laser}	Radius of the laser cross-section
r_{tip}	Radius of the TERS tip apex
RRS	Resonance Raman scattering
RNA	Ribonucleic acid
I	Light intensity
IR	Infrared
ITO	Indium tin oxide
SAM	Self-assembled monolayers

SEM	Scanning electron microscopy
SERS	Surface-enhanced Raman spectroscopy
SEIRA	Surface enhanced infrared absorption spectroscopy
SNOM	Scanning near-field microscopy
SP	Surface plasmon
SPM	Scanning probe microscopy
SS	Single-stranded
STORM	Stochastic optical reconstruction microscopy
STED	Stimulated emission depletion
STM	Scanning tunneling microscope
SWCNT	Single walled carbon nanotube
TERS	Tip-enhanced Raman spectroscopy
T	Thymine
UHV	Ultrahigh vacuum
XPS	X-ray photoelectron spectroscopy
TEM_{00}	Transverse Electromagnetic Mode

List of Appendices

Chapter 1

1   General Introduction

1.1   Overview of Raman Spectroscopy Applications

First observation of elastic light scattering was reported by Lord Rayleigh in the 19th century and in the early 1920's experimental measurements of inelastic light scattering of molecules in liquid phase was conducted by Chandrasekhara Raman.[1,2] At the same time, L. Mandelstam and G. Landsberg observed the similar effects in crystals. [3] C.V. Raman was later awarded the Nobel Prize in physics in 1930. Despite of interesting features of the newly discovered Raman effect, the very weak signal of inelastic light scattering made the experiment difficult mainly due to the lack of powerful light sources and efficient detectors. The application of Raman scattering remained entirely restricted until the 1960s when the first laser was developed by T. Maiman enabling an intense source of monochromatic light.

In parallel to the work of Raman, E.H. Synge proposed in 1928 to use the scattered light by a small particle illuminated from the back and scanned in vicinity of the sample as an excitation source for microscopy. This concept was shared with Albert Einstein who acknowledged the interest of this idea, but he further highlighted that this method was fundamentally and practically unusable.[4] Later, Synge came with another idea of using sharp quartz tip as a light source or a small aperture and this time Einstein encouraged him to further investigate this direction.[5]

In the 1980s, upon the invention of the scanning tunneling microscope (STM) and subsequent developments in ultra-high resolution positioning systems, Wessel proposed

to use the scattering from the small apex of an AFM tip to produce Raman scattering of molecules located in the vicinity of the nano-metric apex. [6] The local increase of the confined electromagnetic field in the vicinity of the tip would provide a spatially resolved signal originating from a nanometric object. In other words, excitation of surface plasmons of the metallic tip could be used to probe molecules and the STM tip would be used as an apertureless optical probe. A decade later, the development of scanning near-field optical microscopy (SNOM) was mainly applied to map fluorescence and luminescence from surfaces with 50 nm spatial resolution.[7]

While the work was mainly pursued by the groups of Batchelder[8,9] and Hallen[10,11] who developed SNOM-Raman imaging, Tsai et al. were able to measure for the first time near-field Raman signals.[12] Further progress in advanced nanofabrication methods and developments of combinations of SNOM with resonance Raman scattering and surface-enhanced Raman scattering (SERS) enabled applications of these techniques in biology, chemistry and other similar fields.[13-15] In the early 2000s, the groups of L. Novotny,[16] R. Zenobi,[17] M. Anderson,[18] and S. Kawata[19] published experimental results on a variety of nanomaterials using the so-called tip-enhanced Raman scattering (TERS).

1.2   Fields of Application of Tip-enhanced Spectroscopy: from Biology to Single Molecule Spectroscopy

Many different experimental techniques such as mass-spectrometry, fluorescence, nuclear magnetic resonance (NMR), infrared and Raman spectroscopy are used to understand biological and chemical information along with interactions of macromolecules and small size-molecules. With these methods, isolated cell components like proteins can be investigated in great detail and even the identification and

classification of cells can be made, albeit sample preparation like labelling or pre-concentration are necessary and can be cumbersome for small quantities of a sample.

Nanometer-scale materials developed over the past decade are of interest for a variety of applications but suffer from poor characterization such as the determination of crystallinity, the orientation of materials, the presence of active sites or defects in the nanoscale building blocks. Here, a critical parameter is the available spatial resolution of a given instrumentation to probe an isolated nano-object with a wealth of details.

Overall, molecular analysis on the nanoscale size is becoming more essential because of advances and new challenges in materials and biomaterial research. Advanced tools to investigate the nanoscale domains that can provide molecular information are therefore critical. Ideally, such techniques must allow one to: i) provide molecular fingerprints of molecules through the measurement of their vibrational spectra, ii) function without any need of labeling step and iii) provide spatial resolution with sub 10 nm resolution. Furthermore, the possibility to obtain simultaneously topographic and spectroscopic information is a valuable asset to correlate surface properties such as surface morphology with molecular information. Such methods such as scanning probe microscopy (e.g. AFM, STM), electron microscopy (EM), as well as super-resolution fluorescence microscopies including stochastic optical reconstruction microscopy (STORM), stimulated emission depletion (STED), and photo activated localization microscopy (PALM) can be used for study of nanoscale materials with high speed and sub 100 nm spatial resolution.[20-25] However, these pure optical techniques based on the measurement of fluorescence require labeling that can influence the native response of the non-labeled material.

In this context, TERS resolution has been evaluated for characterizing a large variety of samples by several leading research groups. For instance, L. Novotny et al.[30] demonstrated investigation of one-dimensional structure single-walled carbon nanotubes using TERS as shown in **Figure 1.1a. V.** Deckert's research group also showed that TERS is a powerful tool for characterizing of bio-molecules such as RNA strands (**Figure 1.1b**),[26] various nucleobases,[27] the lipids and protein domains of human cells,[28] viruses and malaria-infected cell which are presented in **Figure 1.1d** and **Figure 1.1e**.[29]

R. Zenobi *et al.* studied the distribution of two very similar non-resonant thiols within a single monolayer on a gold film as shown in AFM images of **Figure 1.1c.**[31] In a different study, in our group, we demonstrated that TERS can provide valuable information about the adsorption pattern of OPN (phospho-protein osteopontin) on calcium oxalate mono-hydrate crystals without any need to label the protein (**Figure 1.1f**).[33]
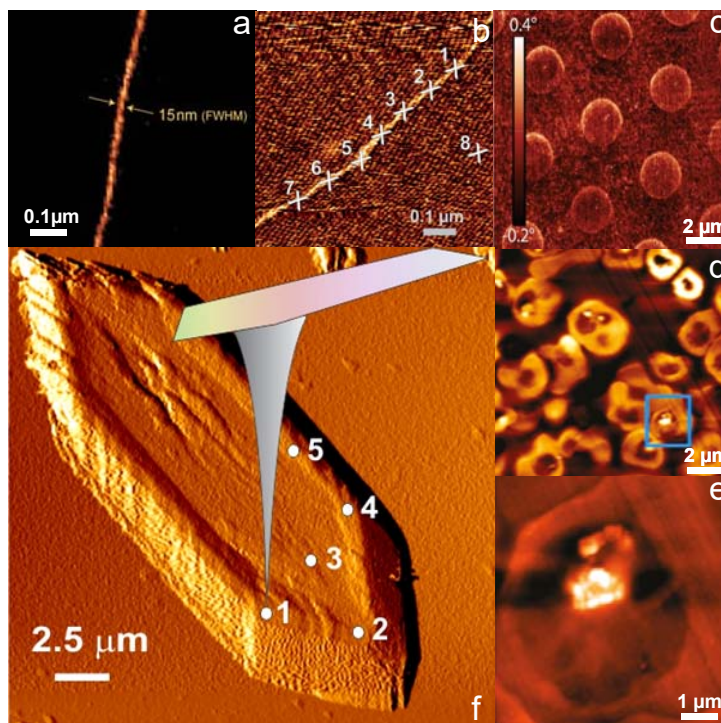
Figure 1.1 Examples of recent TERS studies (a). Near-field Raman imaging of single-walled carbon nanotubes, The image is adapted from reference 30 with permission from Annual Reviews.[30] (b) Topography of a single stranded RNA homo polymer of cytosine, The image is adapted from reference 26 with permission from The Royal Society of Chemistry.[26] (c) AFM tapping mode phase images of micro contact printed 2-mercaptopyridine (2-PySH) on a gold surface The image is adapted from reference 31 with permission from Beilstein-Institut.[31] (d) AFM image of malaria-infected and non-infected cells (e) AFM image of the highlighted area in (d) showing hemozoin crystals inside the infected cell along with TERS spectra acquired with tip approached to or retracted from the cell surface. These images are adapted from reference 32 with permission from American Chemical Society.[32] (f) TERS measurement of Osteopontin Adsorption to Calcium Oxalate Monohydrate Crystals. The image is adapted from reference 33 with permission from American Chemical Society.[33]

1.3   Scope of Thesis

The present thesis is organized as follows: In Chapter 1, the theoretical background on Raman spectroscopy is first introduced. The principles of TERS and underlying plasmonic effect occurring in metallic nanomaterials are then developed.

Experimental design and details associated with the TERS experiments developed in our laboratory are described in Chapter 2 providing technical details of the TERS setup and information on fabrication of the TERS probes. Importantly, this Chapter includes experimental details about the laser polarization consideration.

In Chapter 3 of this thesis, the chemical synthesis of gold and silver nanoplates is detailed. The synthesis was performed in our group in order to achieve the fabrication of ultraflat substrates with a roughness lower than 0.5 nm. We showed in particular that gold can be used to produce flat and large triangular nanoplates. Chapter 4 is a published study that presents the results of a TERS study of self-assembled monolayer of thiolated molecules (azobenzene thiol and nitrobenzenethiol) on gold nanoplate using 532 nm excitation. The polarization state of the input light is set to linearly polarized (Gaussian–transverse TEM00) or radially polarized and we report on the effect of the polarization on the collected Raman spectra.

Chapter 5 is a published study that focuses on the TERS experiments conducted on graphene layers deposited on gold substrate and on glass substrate using red laser (632 nm) excitation that is linearly (Gaussian–transverse TEM00) and radially polarized. The spectral position, width, and intensity of the G and D, 2D vibrational modes of graphene

are studied as a function of the incident light polarization and on the edges of the graphene sheet.

In the last chapter, we demonstrated that TERS is a technique of choice for the characterization of a plasmid free β_2AR cDNA along with its embedded cDNA in plasmid. This also provides us a lateral spatial resolution down to 8 nm obtained by TERS and is discussed in Chapter 6. This Chapter emphasizes that TERS technique provides not only a way to identify biological specimens with nanoscale resolution, but also an accurate localization of an ensemble of nucleic acids present on a selected region of the cDNA strand.

We finally conclude by providing a critical view of the emerging fields where TERS can be of interest as well as the possible technical improvements yielding better reproducibility and better sensitivity of the TERS setup.

1.4 Principles and Theory of Raman and Tip-enhanced Raman Spectroscopy

1.4.1 Raman Spectroscopy

Raman spectroscopy has been known for over 80 years as a powerful analytical method providing information about molecular vibrations fingerprint that can be used for sample identification and quantification. In most cases, it provides additional benefit over mid-IR and near-IR spectroscopy, such as minimal or no sample preparation, no interference from CO_2 or H_2O, and non-destructive analysis that is useful for many applications in art, archeology or forensic investigations.[34,35]

Indeed, a very wide selection of substances can be studied by Raman in either liquid, solid and gas states, sampling volumes can vary from μm^3 to a few dm^3 and the measurements can be done at distance ranging from nanometer dimensions to kilometers. However, the applicability of conventional Raman spectroscopy is limited by two main factors: one is the diffraction limit (Rayleigh criterion) that limits the spatial resolution of a given measurement to about $\lambda/2$ (λ being the wavelength of observation) and the other is the weak intensity of Raman signals. In nanoscience applications, this limited spatial resolution, makes the precise characterization of individual objects impossible in far-field conditions.

When light is impinged on molecules in solid, liquid or gas states, photons can be directly absorbed or scattered. In infrared (IR) or ultraviolet-visible (UV-Vis) spectroscopy, we generally observe the absorption of photons by the molecules. The IR absorption results in the excitation of vibrational modes of the molecules, while the UV-Vis absorption results in the excitation of an electronic transition which can be followed by either a non-radiative relaxation or a radiative emission such as fluorescence or phosphorescence.[36] In addition to absorption, a small portion of the incident light is scattered by the molecules irradiated by the excitation light. Most of these scattered photons will be scattered elastically (Rayleigh scattering) which implies that their energy is equal to the energy of the incident photons. A small portion of the scattered photons (approximately 1 out of 10^8 photons) are however scattered inelastically with frequencies higher or lower compared to the frequency of the incident photons.[36] Raman spectroscopy is indeed based on the detection of such inelastic scattering. In Raman, the molecular system is first promoted to a virtual energy state (with energies below the first

electronic transition but higher than a vibrational one) and then relaxes back to the ground state through scattering of photons with a higher or a lower energy compared to the excitation wavelength. This results in the anti-Stokes and Stokes scattering processes respectively. The anti-Stokes intensity is weaker than the Stokes because the anti-Stokes scattering happens from an excited energy state which, according to the Boltzmann distribution, is less populated than the ground state.[36] **(Figure 1.2)**
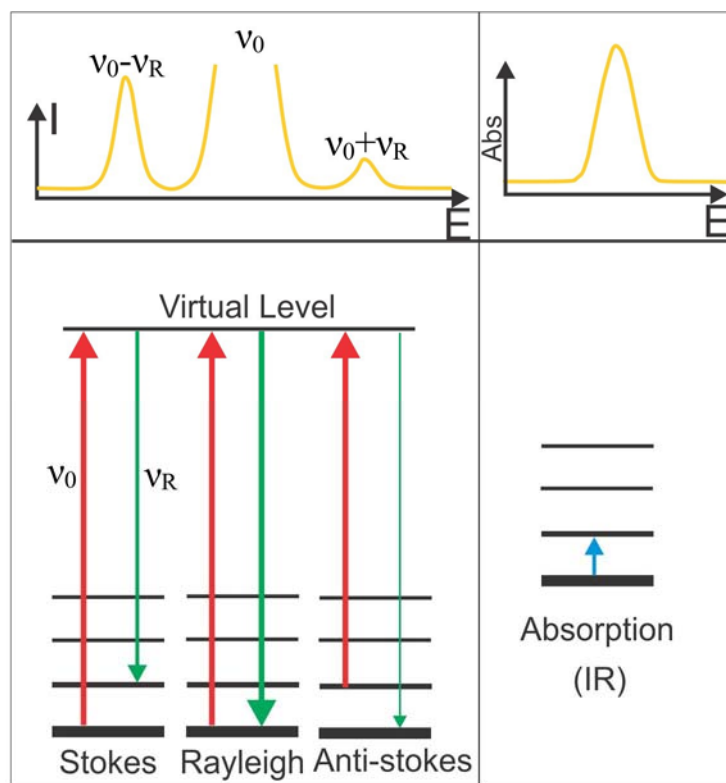
Figure 1.2 Energy level diagram for Raman scattering and IR.

Raman spectroscopy is based on the detection of inelastic scattering of a small quantity of photons and therefore the intensity of Raman signal is weak. Besides, the observation of the Raman scattering can be limited by possible fluorescence which is typically 10 orders of magnitude stronger than the Raman scattering. The masking of the Raman signal by

fluorescence arises specially in biological systems because of the presence of endogenous fluorophores. As a result, methods capable of enhancing the Raman signal are of tremendous interest, keeping modest irradiation energy and small integration time in performing Raman measurements of smaller and fainter molecular systems.

1.4.2   Properties of Plasmons

The irradiation of a metal surface with the proper wavelength of light induces the oscillation of the free electrons of the metal at the interface, which generates an EM wave and a charge motion termed as surface plasmon polariton (SPP).
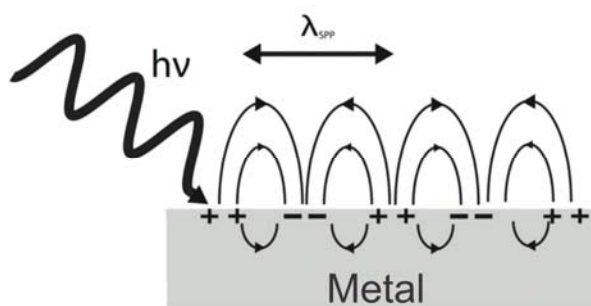
Figure 1.3 Schematic of surface plasmon polaritons at the interface between metal surface and a dielectric.

Although observed in the early 20th century by Zenneck (1907), Mie (1908) and Sommerfield (1909) such plasmon modes can be used for a variety of applications ranging from bio-sensing to metatronics[37] and have fostered a recent and very active field of research referred as "plasmonics". Metatronics aims at replacing electronic circuits by optical circuits that will accomplish all logical operations using the interaction of light with a nanostructured metallic surface, thereby enabling faster logical circuits. A variety of metals have shown to yield usable plasmonic properties for optical circuitry, sensing applications and spectroscopic purposes. Of those, gold and silver are of particular

interest since they have resonance in the visible range which makes them ideal for surface-enhanced Raman measurements.

SP resonance is one of the prominent optical properties of metallic nanostructures and one of the best examples that highlights the peculiar interaction of light with nanoscale metallic materials. Nanoscale hot spots generated due to the SPs effect opens the possibility to enhance the signal of a molecule of interest located in the vicinity of a plasmonic nanostructure.[38] As a result, SPs can be utilized to improve the detection in an extensive variety of fields including biomedical,[39-41] energy,[42-44] environment protection,[45-47] sensing and information technology.[38,48]

1.4.3 The Role of Localized Surface Plasmon Resonance in Raman Spectroscopy

One of the recent developments in nanoscience is the control over the opto-geometric parameters of nanomaterials in order to accurately tune their localized surface plasmon resonance (LSPR). LSPRs are non-propagating excitations generated by a light which trapped within conduction electrons of metallic material with size of smaller than the wavelength of light. **(Figure 1.4)**

LSPR is a result of the interactions between conductive surface electrons and the incident light (like a laser source) which strongly depends on the, geometry, composition, dielectric environment, size and distance between adjacent nanoparticles.[49,50]
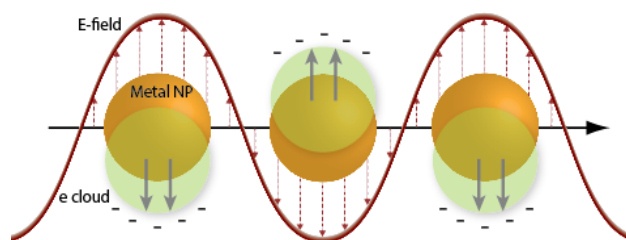
Figure 1.4 Schematic localized surface plasmon resonance (LSPR). Reprinted with permission from reference 51. [51]

The interaction between nanoparticles and light can be valued for a variety of applications such as photovoltaics, bio-imaging and laser photo thermal therapy.[49,52,53] The strong enhancement of electric field due to this effect in near-field is presently used for sub-wavelength resolution microscopic measurements as well as to increase the detection capabilities of spectroscopic methods such as surface-enhanced Raman spectroscopy (SERS), metal-enhanced fluorescence (MEF), plasmon resonance energy transfer (PRET),[53] near-field lithography, nano photonics and also in single-molecule detection on a nanostructure.[54,55]

1.4.4   Diffraction Limit in Optical Measurements

Optical spectroscopy provides significant information on structure and dynamic properties of materials. Since the energies of light quanta (photons) lie in the energy range of electronic and vibrational transitions in matter, combining optical spectroscopy with microscopy is therefore desirable because spectral features can then be spatially resolved. However, the diffraction limit has restricted researchers from investigating features smaller than half a wavelength of the applied radiation. Two decades ago, it was demonstrated that near-field optical microscopy was able to expand the range of optical measurements beyond the diffraction limit.[56] Although the accessible spatial resolution

does not presently compare to related scanning-probe techniques (e.g., scanning-tunneling microscopy), it is the combination of resolution and chemical information that makes near-field optical microscopy of great interest. (**Figure 1.5**)
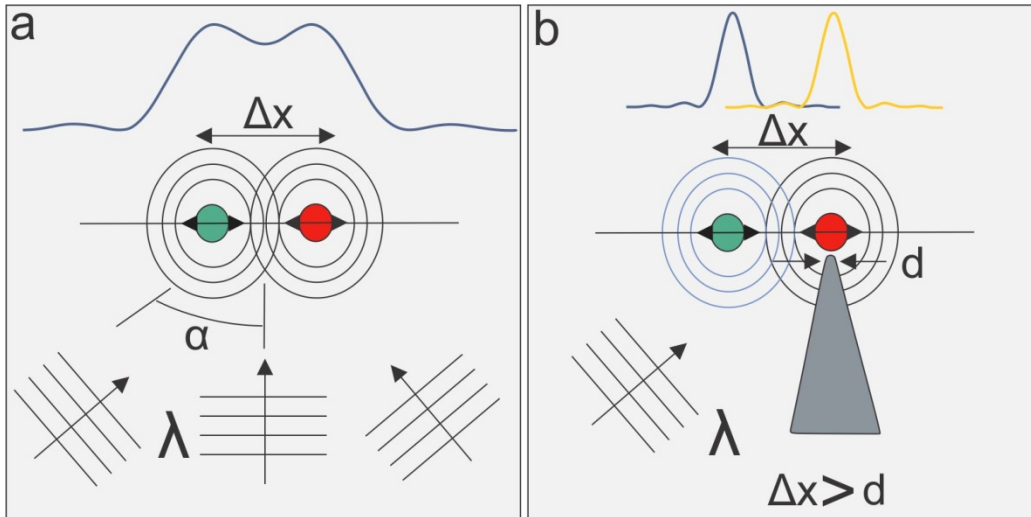
Figure 1.5 Comparison of diffraction-limited optical microscopy and near-field optical microscopy. (a) Diffraction-limited optical microsocopy; (b) Near-field optical microscopy

As illustrated in **Figure 1.5,** the spatial resolution Δx of a standard optical microscopy measurement can be described by the Abbe's criterion (Eq. [1]):

$$\Delta x = 0.61\lambda/N.A. \qquad [1]$$

Where, λ is the wavelength of the interacting radiation, and $N.A. = n\ sin\ \alpha$ is the numerical aperture ($N.A.$) of the objective lens. The $N.A.$ can be enhanced by a large index of refraction n of the surrounding medium or a large angle of acceptance α.

In near-field optical microscopy, the resolution Δx no longer depends on λ but on a characteristic length d (e.g., aperture diameter or tip diameter) of a local probe. Near-field

optical microscopy depends on a confined photon flux between a local probe and the sample surface. In Synge's original concept, the local probe including of a tiny aperture in an ideally reflecting metal screen.[57] Directly behind the irradiated screen, the light field is spatially limited to the size of the aperture (*d*). If a scatterer is within a distance *d* from the aperture, it will interact with the radiation field. Synge's concept was soon forgotten after its inception. This is due to the fact that the lack of nanofabrication techniques made it hard to follow. In the following decades, the idea was reinvented several times.

1.4.5   Tip-enhanced Raman Spectroscopy

Surface enhanced Raman scattering (SERS) is repeatedly used to improve the Raman signal intensity by 6 to 8 orders of magnitude.[17,58,59] In SERS, the sample must be deposited as a thin layer onto a rough noble metal film, [60] a metal electrode, [61] or a colloidal solution of metal particles.[62] Unfortunately, the SERS enhancement varies across the sample and depends critically on the substrate or colloidal solution preparation. This strongly limits its utility and quantitative measurements are very difficult to conduct.[17]

With the aim to circumvent such limitations, it was proposed to surpass the diffraction limit using a confined electromagnetic field at the end of a metallic tip.[63] As a result, the spectroscopic signal from vibrational modes of molecules located in the vicinity of the tip will be enhanced. TERS has been developed to acquire chemical information with very high spatial resolution,[64-66] or chemical information from very few molecules, and in some cases even single molecules when combined with resonant conditions.[67,68] Recently, single-molecule gap-mode TERS has been demonstrated by different groups separately. [67,69,70] Studies using TERS not only open the door for

nanoscale vibrational spectroscopy, but also could result in a better understanding of locally enhanced vibrational spectra from metallic surfaces.

Since TERS combines the use of an atomic force microscope with a confocal microscope, large enhancements from nanoscale dimensions can be achieved yielding a high optical contrast with an improved spatial resolution better than 50 nm.[71-73] Specific to metallic materials, the local field enhancement can be further increased in the range of 10^2-10^5 depending on the sample and the setup.[72,74,75] Likewise SERS, TERS is also a surface technique requires the immobilization of the molecules or nanostructure of interest to be deposited onto a surface. Many substrate types can be utilized such as rough or smooth substrates,[76] single crystalline,[77] metal,[78] semiconductor,[79,80] or an isolator.[17] In other words, TERS enables the controlled generation of an enhanced Raman at a specific location defined by the tip spatial position. The tip can be scanned across the surface of the sample yielding a spatial lateral resolution that is only limited by size of the tip apex (10-50 nm). As expected from a near-field contribution, the TERS signal from the tip apex decrease drastically with increasing distance between sample and tip. Beyond 10-20 nm, the TERS signal vanishes.[81]

The goal of TERS microscopy is therefore to acquire the spectral response from molecules adsorbed onto nanostructures with an optical resolution beyond the diffraction limitation. For this purpose, a sharp metal tip is accurately positioned near the sample surface.[30,82] The tip enables a channel through which the near-field components of the scattered light (evanescent waves) converts to propagated waves in the far-field zone that can be detected using conventional detectors. This implies that by using a confined source field with a large bandwidth of spatial frequencies, high spatial frequencies

produced from the sample are become available in the far-field, and the spatial resolution is only limited by the diameter of the tip apex.[83]

The scattered collected light consists of two spectra: the near-field spectrum originating from the tip apex and small sample region, the far-field background that was generated in the entire illuminated sample volume. In general, the two enhancement mechanisms accepted for SERS and TERS derive from (1) a mediated electromagnetic enhancement through the excitation of the localized surface plasmon and (2) a chemical enhancement due to the charge transfer in oriented molecules at a metal surface. **(Figure1.6)**

(1) The matching of the input laser wavelength with the proper polarization with the LSPR of the metallic tip induces a coupled excitation of the electron if the metal causing surface-charge-density oscillations. Since the surface-charge oscillations are intimately coupled to electromagnetic fields, surface plasmons are polaritons which means the antenna locally improves the density of electromagnetic states, thereby increasing the modes into which the source can radiate and vice versa.[26,51]

(2) The other mechanism involved in signal enhancement is chemical enhancement, which primarily involves charge transfer mechanisms, where the excitation wavelength is resonant with the metal-molecule charge transfer electronic states. The chemical mechanism is thought to be an enhancement in polarizability caused by direct interaction between the adsorbed molecule and the metal surface. Perturbations to the electronic structure of the molecule upon adsorption and charge-transfer effects result in an increase in the Raman cross-section for the adsorbed molecule relative to the solution phase. In general, it appears that, the contribution to overall enhancement from chemical effects is quite modest in comparison to electromagnetic effects.[26,51]
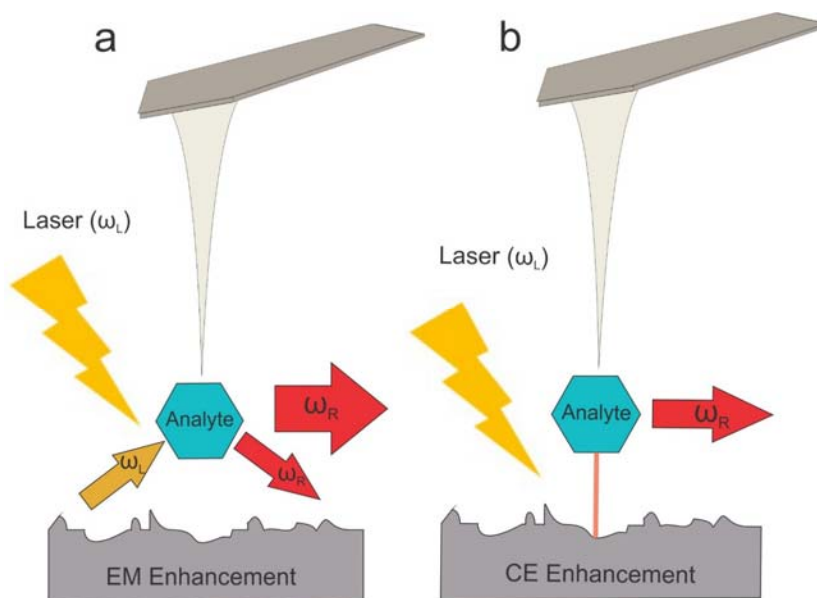
Figure 1.6 Schematic representation of (a) the electromagnetic effect (EM) and (b) chemical enhancements effect (CE) in TERS (ω_L: Excitation frequency, ω_R: Raman scattering frequency). These images are adapted from reference 84 with permission from The Royal Society of Chemistry.[84]

1.5   Summary

The mechanism and basic principles of TERS were reviewed, highlighting the optical effects that occur nearby nanoscale metallic structures. The excitation of the localized surface plasmon can be utilized for a variety of applications including tip-enhanced Raman spectroscopy yielding enhanced spatial resolution of optical measurements. The TERS technique will be detailed from a more experimental and technical point of view in the following Chapter.

1.6 References

(1)   Raman, C. V.; Krishnan, K. S., A new type of secondary radiation. *Nature (London, U. K.)* **1928**, *121*, 501.

(2)   Raman, C. V.; Krishnan, K. S., The optical analog of the Compton effect. *Nature (London, U. K.)* **1928**, *121*, 711.

(3)   Landsberg, G.; Mandelstam, L., A novel effect of light scattering in crystals. *Naturwissenschaften* **1928**, *16*, 557.

(4)   Novotny, L. In *Progress in Optics*; Wolf, E., Ed.; Elsevier: 2007; Vol. Volume 50, p 137.

(5)   Synge, E. H., A suggested method for extending microscopic resolution into the ultra-microscopic region. *Philos. Mag. (1798-1977)* **1928**, *6*, 356.

(6)   Wessel, J., Surface-enhanced optical microscopy. *J. Opt. Soc. Am. B: Opt. Phys.* **1985**, *2*, 1538.

(7)   Dunn, R. C., Near-Field Scanning Optical Microscopy. *Chem. Rev. (Washington, D. C.)* **1999**, *99*, 2891.

(8)   Smith, D. A.; Webster, S.; Ayad, M.; Evans, S. D.; Fogherty, D.; Batchelder, D., Development of a scanning near-field optical probe for localized Raman spectroscopy. *Ultramicroscopy* **1995**, *61*, 247.

(9)   Webster, S.; Batchelder, D. N.; Smith, D. A., Submicron resolution measurement of stress in silicon by near-field Raman spectroscopy. *Appl. Phys. Lett.* **1998**, *72*, 1478.

(10)   Jahncke, C. L.; Paesler, M. A.; Hallen, H. D., Raman imaging with near-field scanning optical microscopy. *Appl. Phys. Lett.* **1995**, *67*, 2483.

(11)   Jahncke, C. L.; Hallen, H. D.; Paesler, M. A., Nano-Raman spectroscopy and imaging with a near-field scanning optical microscope. *J. Raman Spectrosc.* **1996**, *27*, 579.

(12)   Tsai, D. P.; Othonos, A.; Moskovits, M.; Uttamchandani, D., Raman spectroscopy using a fiber optic probe with subwavelength aperture. *Appl. Phys. Lett.* **1994**, *64*, 1768.

(13)   Stockle, R.; Fokas, C.; Deckert, V.; Zenobi, R.; Sick, B.; Hecht, B.; Wild, U. P., High-quality near-field optical probes by tube etching. *Appl. Phys. Lett.* **1999**, *75*, 160.

(14)   Zeisel, D.; Deckert, V.; Zenobi, R.; Vo-Dinh, T., Near-field surface-enhanced Raman spectroscopy of dye molecules adsorbed on silver island films. *Chem. Phys. Lett.* **1998**, *283*, 381.

(15)   Zenobi, R.; Deckert, V., Scanning Near-Field Optical Microscopy and Spectroscopy as a Tool for Chemical Analysis. *Angew. Chem. Int. Ed.* **2000**, *39*, 1746.

(16)   Sanchez, E. J.; Novotny, L.; Xie, X. S., Near-Field Fluorescence Microscopy Based on Two-Photon Excitation with Metal Tips. *Phys. Rev. Lett.* **1999**, *82*, 4014.

(17)   Stockle, R. M.; Suh, Y. D.; Deckert, V.; Zenobi, R., Nanoscale chemical analysis by tip-enhanced Raman spectroscopy. *Chem. Phys. Lett.* **2000**, *318*, 131.

(18)   Anderson, M. S., Locally enhanced Raman spectroscopy with an atomic force microscope. *Appl. Phys. Lett.* **2000**, *76*, 3130.

(19)   Hayazawa, N.; Inouye, Y.; Sekkat, Z.; Kawata, S., Metallized tip amplification of near-field Raman scattering. *Opt. Commun.* **2000**, *183*, 333.

(20)   Engel, A., Scanning transmission electron microscopy: biological applications. *Adv. Imaging Electron Phys.* **2009**, *159*, 357.

(21)   Medalsy, I.; Hensen, U.; Muller, D. J., Imaging and Quantifying Chemical and Physical Properties of Native Proteins at Molecular Resolution by Force-Volume AFM. *Angew. Chem., Int. Ed.* **2011**, *50*, 12103.

(22)   Hell, S. W., Far-Field Optical Nanoscopy. *Science (Washington, DC, U. S.)* **2007**, *316*, 1153.

(23)   Berning, S.; Willig, K. I.; Steffens, H.; Dibaj, P.; Hell, S. W., Nanoscopy in a Living Mouse Brain. *Science (Washington, DC, U. S.)* **2012**, *335*, 551.

(24)   Vaughan, J. C.; Zhuang, X., New fluorescent probes for super-resolution imaging. *Nat. Biotechnol.* **2011**, *29*, 880.

(25)   Dempsey, G. T.; Vaughan, J. C.; Chen, K. H.; Bates, M.; Zhuang, X., Evaluation of fluorophores for optimal performance in localization-based super-resolution imaging. *Nat. Methods* **2011**, *8*, 1027.

(26)   Bailo, E.; Deckert, V., Tip-enhanced Raman scattering. *Chem. Soc. Rev.* **2008**, *37*, 921.

(27)   Treffer, R.; Lin, X.; Deckert-Gaudig, T.; Deckert, V., Distinction of nucleobases - a tip-enhanced Raman approach. *Beilstein J. Nanotechnol.* **2011**, *2*, 628.

(28)   Richter, M.; Hedegaard, M.; Deckert-Gaudig, T.; Lampen, P.; Deckert, V., Laterally Resolved and Direct Spectroscopic Evidence of Nanometer-Sized Lipid and Protein Domains on a Single Cell. *Small* **2011**, *7*, 209.

(29)   Cialla, D.; Deckert-Gaudig, T.; Budich, C.; Laue, M.; Moeller, R.; Naumann, D.; Deckert, V.; Popp, J., Raman to the limit: tip-enhanced raman spectroscopic investigations of a single tobacco mosaic virus. *J. Raman Spectrosc.* **2009**, *40*, 240.

(30)   Novotny, L.; Stranick, S. J., Near-field optical microscopy and spectroscopy with pointed probes. *Annu. Rev. Phys. Chem.* **2006**, *57*, 303.

(31)   Stadler, J.; Schmid, T.; Opilik, L.; Kuhn, P.; Dittrich, P. S.; Zenobi, R., Tip-enhanced Raman spectroscopic imaging of patterned thiol monolayers. *Beilstein J. Nanotechnol.* **2011**, *2*, 509.

(32)   Wood, B. R.; Bailo, E.; Khiavi, M. A.; Tilley, L.; Deed, S.; Deckert-Gaudig, T.; McNaughton, D.; Deckert, V., Tip-Enhanced Raman Scattering (TERS) from Hemozoin Crystals within a Sectioned Erythrocyte. *Nano Lett.* **2011**, *11*, 1868.

(33)   Kazemi-Zanjani, N.; Chen, H.; Goldberg, H. A.; Hunter, G. K.; Grohe, B.; Lagugné-Labarthet, F., Label-Free Mapping of Osteopontin Adsorption to Calcium Oxalate Monohydrate Crystals by Tip-Enhanced Raman Spectroscopy. *J. Am. Chem. Soc.* **2012**, *134*, 17076.

(34)   Raza, A.; Saha, B., Application of Raman spectroscopy in forensic investigation of questioned documents involving stamp inks. *Sci. Justice* **2013**, *53*, 332.

(35)   Bersani, D.; Madariaga, J. M., Applications of Raman spectroscopy in art and archaeology. *J. Raman Spectrosc.* **2012**, *43*, 1523.

(36)   Petry, R.; Schmitt, M.; Popp, J., Raman spectroscopy-a prospective tool in the life sciences. *ChemPhysChem* **2003**, *4*, 14.

(37)   Sun, Y.; Edwards, B.; Alù, A.; Engheta, N., Experimental Realization of Optical Lumped Nanocircuits at Infrared Wavelenght. Nature Mat. **2012**, *11*, 208.

(38)   Barnes, W. L.; Dereux, A.; Ebbesen, T. W., Surface plasmon subwavelength optics. *Nature* **2003**, *424*, 824.

(39)   Wolfgang, F.; Taton, T. A., Metal nanoparticles as labels for heterogeneous, chip-based DNA detection. *Nanotechnology* **2003**, *14*, R63.

(40)   Hu, M.; Chen, J.; Li, Z.-Y.; Au, L.; Hartland, G. V.; Li, X.; Marquez, M.; Xia, Y., Gold nanostructures: engineering their plasmonic properties for biomedical applications. *Chem. Soc. Rev.* **2006**, *35*, 1084.

(41)   Eustis, S.; El-Sayed, M. A., Why gold nanoparticles are more precious than pretty gold: Noble metal surface plasmon resonance and its enhancement of the radiative and nonradiative properties of nanocrystals of different shapes. *Chem. Soc. Rev.* **2006**, *35*, 209.

(42)   Pillai, S.; Catchpole, K. R.; Trupke, T.; Green, M. A., Surface plasmon enhanced silicon solar cells. *J. Appl. Phys.* **2007**, *101*, 093105.

(43)   Atwater, H. A.; Polman, A., Plasmonics for improved photovoltaic devices. *Nat Mater* **2010**, *9*, 205.

(44)   Narayanan, R.; El-Sayed, M. A., Catalysis with Transition Metal Nanoparticles in Colloidal Solution: Nanoparticle Shape Dependence and Stability. *J. Phys. Chem. B* **2005**, *109*, 12663.

(45)   Matheu, P.; Lim, S. H.; Derkacs, D.; McPheeters, C.; Yu, E. T., Metal and dielectric nanoparticle scattering for improved optical absorption in photovoltaic devices. *Appl. Phys. Lett.* **2008**, *93*, 113108.

(46)   Awazu, K.; Fujimaki, M.; Rockstuhl, C.; Tominaga, J.; Murakami, H.; Ohki, Y.; Yoshida, N.; Watanabe, T., A Plasmonic Photocatalyst Consisting of Silver Nanoparticles Embedded in Titanium Dioxide. *J. Am. Chem. Soc.* **2008**, *130*, 1676.

(47)   Larsson, E. M.; Langhammer, C.; Zorić, I.; Kasemo, B., Nanoplasmonic Probes of Catalytic Reactions. *Science* **2009**, *326*, 1091.

(48)   Ozbay, E., Plasmonics: Merging Photonics and Electronics at Nanoscale Dimensions. *Science* **2006**, *311*, 189.

(49)   Liz-Marzan, L. M., Tailoring Surface Plasmons through the Morphology and Assembly of Metal Nanoparticles. *Langmuir* **2006**, *22*, 32.

(50)   Clavero, C., Plasmon-induced hot-electron generation at nanoparticle/metal-oxide interfaces for photovoltaic and photocatalytic devices. *Nat. Photonics* **2014**, *8*, 95.

(51)   Martinsson, E. Linköping University,Sweden, 2015.

(52)   Lu, X.; Rycenga, M.; Skrabalak, S. E.; Wiley, B.; Xia, Y., Chemical synthesis of novel plasmonic nanoparticles. *Annu. Rev. Phys. Chem.* **2009**, *60*, 167.

(53)   Choi, Y.; Kang, T.; Lee, L. P., Plasmon Resonance Energy Transfer (PRET)-based Molecular Imaging of Cytochrome c in Living Cells. *Nano Lett.* **2009**, *9*, 85.

(54)   Jensen, T. R.; Malinsky, M. D.; Haynes, C. L.; van Duyne, R. P., Nanosphere Lithography: Tunable Localized Surface Plasmon Resonance Spectra of Silver Nanoparticles. *J. Phys. Chem. B* **2000**, *104*, 10549.

(55)   Yguerabide, J.; Yguerabide, E. E., Light-scattering submicroscopic particles as highly fluorescent analogs and their use as tracer labels in clinical and biological applications. I. Theory. *Anal. Biochem.* **1998**, *262*, 137.

(56)   Lewis, A.; Taha, H.; Strinkovski, A.; Manevitch, A.; Khatchatouriants, A.; Dekhter, R.; Ammann, E., Near-field optics: from subwavelength illumination to nanometric shadowing. *Nature Biotechnology* **2003**, *21*, 1378.

(57)   Inouye, Y.; Kawata, S., A scanning near-field optical microscope having scanning electron tunnelling microscope capability using a single metallic probe tip. *Journal of Microscopy* **1995**, *178*, 14.

(58)   Jeanmaire, D. L.; Van Duyne, R. P., Surface Raman spectroelectrochemistry. Part I. Heterocyclic, aromatic, and aliphatic amines adsorbed on the anodized silver electrode. *J. Electroanal. Chem. Interfacial. Electrochem.* **1977**, *84*, 1.

(59)   Nie, S.; Emory, S. R., Probing single molecules and single nanoparticles by surface-enhanced Raman scattering. *Science (Washington, D. C.)* **1997**, *275*, 1102.

(60)   Talaga, D.; Bonhommeau, S., Bare and protected sputtered-noble-metal films for surface-enhanced Raman spectroscopy. *Chem. Phys. Lett.* **2014**, *615*, 89.

(61)   Ren, B.; Lin, X.-F.; Jiang, Y.-X.; Cao, P.-G.; Xie, Y.; Huang, Q.-J.; Tian, Z.-Q., Optimizing Detection Sensitivity on Surface-Enhanced Raman Scattering of Transition-Metal Electrodes with Confocal Raman Microscopy. *Appl. Spectrosc.* **2003**, *57*, 419.

(62)   Li, X.; Xu, W.; Zhang, J.; Jia, H.; Yang, B.; Zhao, B.; Li, B.; Ozaki, Y., Self-Assembled Metal Colloid Films: Two Approaches for Preparing New SERS Active Substrates. *Langmuir* **2004**, *20*, 1298.

(63)   Wessel, J., Surface-enhanced optical microscopy. *J. Opt. Soc. Am. B.* **1985**, *2*, 1538.

(64)   Anderson, N.; Hartschuh, A.; Novotny, L., Chirality Changes in Carbon Nanotubes Studied with Near-Field Raman Spectroscopy. *Nano Lett.* **2007**, *7*, 577.

(65)   Steidtner, J.; Pettinger, B., Tip-Enhanced Raman Spectroscopy and Microscopy on Single Dye Molecules with 15 nm Resolution. *Phys. Rev. Lett.* **2008**, *100*, 236101/1.

(66)   Hartschuh, A.; Qian, H.; Georgi, C.; Boehmler, M.; Novotny, L., Tip-enhanced near-field optical microscopy of carbon nanotubes. *Anal. Bioanal. Chem.* **2009**, *394*, 1787.

(67)   Neacsu, C. C.; Dreyer, J.; Behr, N.; Raschke, M. B., Scanning-probe Raman spectroscopy with single-molecule sensitivity. *Phys. Rev. B: Condens. Matter Mater. Phys.* **2006**, *73*, 193406/1.

(68)   Domke, K. F.; Zhang, D.; Pettinger, B., Toward Raman Fingerprints of Single Dye Molecules at Atomically Smooth Au(111). *J. Am. Chem. Soc.* **2006**, *128*, 14721.

(69)   Zhang, W.; Cui, X.; Yeo, B.-S.; Schmid, T.; Hafner, C.; Zenobi, R., Nanoscale Roughness on Metal Surfaces Can Increase Tip-Enhanced Raman Scattering by an Order of Magnitude. *Nano Lett.* **2007**, *7*, 1401.

(70)   Zhang, D.; Domke, K. F.; Pettinger, B., Tip-Enhanced Raman Spectroscopic Studies of the Hydrogen Bonding between Adenine and Thymine Adsorbed on Au(111). *Chem.Phys.Chem* **2010**, *11*, 1662.

(71)   Kneipp, K.; Wang, Y.; Kneipp, H.; Perelman, L. T.; Itzkan, I.; Dasari, R. R.; Feld, M. S., Single molecule detection using surface-enhanced Raman scattering (SERS). *Phys. Rev. Lett.* **1997**, *78*, 1667.

(72)   Xu, H.; Aizpurua, J.; Kall, M.; Apell, P., Electromagnetic contributions to single-molecule sensitivity in surface-enhanced Raman scattering. *Phys. Rev. E: Stat. Phys., Plasmas, Fluids, Relat. Interdiscip. Top.* **2000**, *62*, 4318.

(73)   Notingher, I.; Elfick, A., Effect of sample and substrate electric properties on the electric field enhancement at the Apex of SPM nanotips. *J. Phys. Chem. B* **2005**, *109*, 15699.

(74)   Fleischmann, M.; Hendra, P. J.; McQuillan, A. J., Raman spectra of pyridine adsorbed at a silver electrode. *Chem. Phys. Lett.* **1974**, *26*, 163.

(75)   Demming, A. L.; Festy, F.; Richards, D., Plasmon resonances on metal tips: understanding tip-enhanced Raman scattering. *J. Chem. Phys.* **2005**, *122*, 184716/1.

(76)   Pettinger, B.; Picardi, G.; Schuster, R.; Ertl, G., Surface-enhanced and STM tip-enhanced Raman spectroscopy of CN- ions at gold surfaces. *J. Electroanal. Chem.* **2003**, *554-555*, 293.

(77)   Pettinger, B.; Ren, B.; Picardi, G.; Schuster, R.; Ertl, G., Nanoscale Probing of Adsorbed Species by Tip-Enhanced Raman Spectroscopy. *Phys. Rev. Lett.* **2004**, *92*, 096101/1.

(78)   Pettinger, B.; Picardi, G.; Schuster, R.; Ertl, G., Surface enhanced Raman spectroscopy: towards single molecule spectroscopy. *Electrochemistry* **2000**, *68*, 942.

(79)   Mehtani, D.; Lee, N.; Hartschuh, R. D.; Kisliuk, A.; Foster, M. D.; Sokolov, A. P.; Maguire, J. F., Nano-Raman spectroscopy with side-illumination optics. *J. Raman Spectrosc.* **2005**, *36*, 1068.

(80)   Steidtner, J.; Pettinger, B., High-resolution microscope for tip-enhanced optical processes in ultrahigh vacuum. *Rev. Sci. Instrum.* **2007**, *78*, 103104/1.

(81)   Hartschuh, A.; Sanchez, E. J.; Xie, X. S.; Novotny, L., High-Resolution Near-Field Raman Microscopy of Single-Walled Carbon Nanotubes. *Phys. Rev. Lett.* **2003**, *90*, 095503/1.

(82)   Cancado, L. G.; Hartschuh, A.; Novotny, L., Tip-enhanced Raman spectroscopy of carbon nanotubes. *J. Raman Spectrosc.* **2009**, *40*, 1420.

(83)   Hartschuh, A.; Beversluis, M. R.; Bouhelier, A.; Novotny, L., Tip-enhanced optical spectroscopy. *Philos. Trans. R. Soc. London, Ser. A* **2004**, *362*, 807.

(84)   Guerrini, L.; Graham, D., Molecularly-mediated assemblies of plasmonic nanoparticles for Surface-Enhanced Raman Spectroscopy applications. *Chem. Soc. Rev.* **2012**, *41*, 7085.

Chapter 2

2 Experimental Design and Technical Aspects for Tip-Enhanced Raman Spectroscopy

This Chapter provides details of the experimental setup developed in the Lagugné-Labarthet's research group and associated optimal parameters to achieve high sensitivity and high spatial resolution in TERS experiments. Several challenges that prevent the widespread application of this technique are also discussed. In particular, the fabrication of efficient and reproducible TERS probes is indeed one of the most critical challenges that face most TERS users. The nanometer spatial resolution in TERS measurements is mainly limited by the size and the shape of the probe apex which is critical to control, thus requiring an optimized fabrication method. Moreover, the polarization of the incident light is an important parameter to yield large enhancement in TERS. When using transmission geometry, a radially polarized light source is particular interest to have a longitudinally polarized component oriented along the tip axis. This Chapter reviews the polarization control of the excitation light that has been integrated in our TERS setup.

2.1 Technical Aspects

2.1.1 Typical TERS Optical Configurations

TERS setups are typically classified into transmission-mode and reflection-mode geometries as depicted in **Figure 2.1.** The setup of the transmission-mode TERS system usually utilizes an inverted microscope. **(Figure 2.1a)** The laser light is focused with a high numerical aperture (*N.A.*) objective on the tip apex and the back-scattered light is collected with the same objective. The transmission-mode has the advantage to have a single axis geometry where the propagation direction is along the tip axis. It is based on

the use of objectives with very high numerical apertures (typically 1.4) and short working distances yielding (typically 400 μm) very sharp focus at the focal plane. The transmission setup is however limited to transparent substrates.

Another mode of TERS is the reflection-mode which is more suitable for non-transparent substrates. (**Figure 2.1 b, c**). Because of the side geometry, long working distance objectives and lower N.A. can be used yielding larger and non-symmetric spot size at the focal plane giving larger background signal and lower signal/noise ratio. Importantly, one challenge in TERS optical configuration is to produce the strongest electromagnetic field enhancement in the vicinity of the tip probe. For this, the polarization can be altered in such a way that optimized confinement of the electric field is obtained. [1,2] Briefly, the polarization vector must have a large component along the tip axis which is trivial to achieve in a reflection geometry but more complex with a transmission geometry. This aspect will be discussed in detail in the following section.
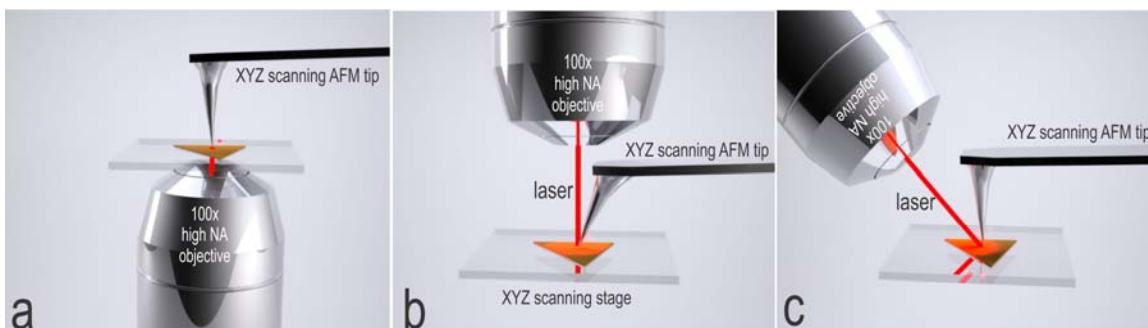
Figure 2.1 TERS optical configurations (a) bottom illumination (b) top illumination (c) side illumination geometry

Bottom Axial Illumination. In this setup **(Figure 2.1a)**, the excitation light source is located below the transparent substrate authorizing the use of immersion objectives with numerical apertures as high as 1.4 that are either oil or water immersion. [3-5] The TERS

signal is backscattered and collected by the same objective before spectral analysis and detection. This setup guarantees a high efficiency for light collection and the axial alignment of the tightly focused laser beam with the tip axis provides ideal configuration for alignment. The main limitation of this setup is the restriction to transparent samples and substrates. Thin substrates such as thin glass cover slips are generally used. Indium tin oxide (ITO),[6] quartz[7] or transparent gold plates[8] are other alternatives as transparent substrates as long as their thicknesses are compatible with a given microscope objective.

Top Axial Illumination. In the configuration with a top axial illumination, the microscope objective is on the same side of the AFM tip with a co-axial alignment. Such illumination geometry allows to work on both transparent and opaque samples.[9,10] The coated tips used for this particular mode have a bent geometry with a large opening angle as depicted in **Figure 2.1b** to avoid shadowing effect from the cantilever of the tip. Objectives with large numerical objective can be used but a long working distance is necessary since the tip and the tip holder are positioned between the objective and the tip thus requiring a minimum space of several millimeters. Consequently, the numerical aperture of the microscope objective must be selected to focus and collect the scattered photons around the tip as efficiently as possible. Typically, the numerical aperture of these reflection objectives is typically around 0.7.[11-13] Furthermore, such illumination geometry permit us to work on both transparent and opaque samples. One of the biggest challenges in this geometry is due to the tip position located between the objective and

the objective and blocks a certain amount of light during illumination giving a lower Raman signal.

Side Illumination. TERS instrument using side illumination setup has been presented as early as 2001 since they were based on commercial AFM that were not initially conceived to host a microscope objective in a transmission configuration. [14] In side illumination **(Figure 2.1c)**, the laser is focused on the tip apex from the side and by using microscope objectives to dominate the limitation of bottom illumination approach sample transparency. A few different the side-illumination approaches using AFM and STM setups followed shortly after.[15-20] In this geometry the tip is illuminated from the side by using microscope objectives with long working distance at an angle in 45-70° range relative to the tip axis.[20] The polarization of the excitation light is p-polarized with a half-wave plate in order to have a strong component along the tip axis. High laser power of several mW is usually used for side illumination because of the long working distance of the objective and its low numerical aperture limited to 0.3-0.6 N.A. The main advantage of this geometry is the ability to use on opaque samples. Despite a low numerical aperture, this configuration can yet yield strong enhancement in the gap between a metallic interface and the metallic TERS tip.[21,22]

2.1.2   TERS Experimental Setup

In the present thesis, the TERS setup is based on a commercial Raman spectrometer (600 gr/mm grating, HR LabRam, Horiba-Jobin-Yvon, Kyoto, Japan) connected to an inverted optical microscope (IX71, Olympus, Tokyo, Japan) and interfaced with a 5 axis atomic force microscope system (AFM, NanoWizard II Bioscience, JPK Instruments Inc., Berlin, Germany **(Figure 2.2)** to perform

measurements with a bottom illumination configuration and back-scattering collection geometry as shown in **Figure 2.3**.

The AFM is equipped with a high resolution piezoelectric xy sample scanner as well as an independent xyz piezoelectric actuator to independently control the tip position and to hold the tip a few nanometers above the sample surface during TERS measurements. The Raman signal of the sample is filtered from Rayleigh scattering by using an edge filter located prior to the spectrometer. With regards to the detection system, a 0.8 m spectrometer equipped with a 600 gr/mm grating disperses the collected light spectrally prior to detection. The spectral resolution achieved with this spectrometer is typically 3-4 cm^{-1}. Alternatively, a 1800 gr/mm grating can be used to increase the spectral resolution and diffraction efficiency albeit the detected intensities will be lower. A liquid nitrogen-cooled charge coupled device (CCD 1024x1600 pixels, Symphony Horiba) with close to single photon counting capacity and high efficiency in the visible range is used in this spectrometer. When 600 gr/mm grating is used, the obtained Raman spectra extends roughly over 1100 cm^{-1} spectral range in a single acquisition windows.
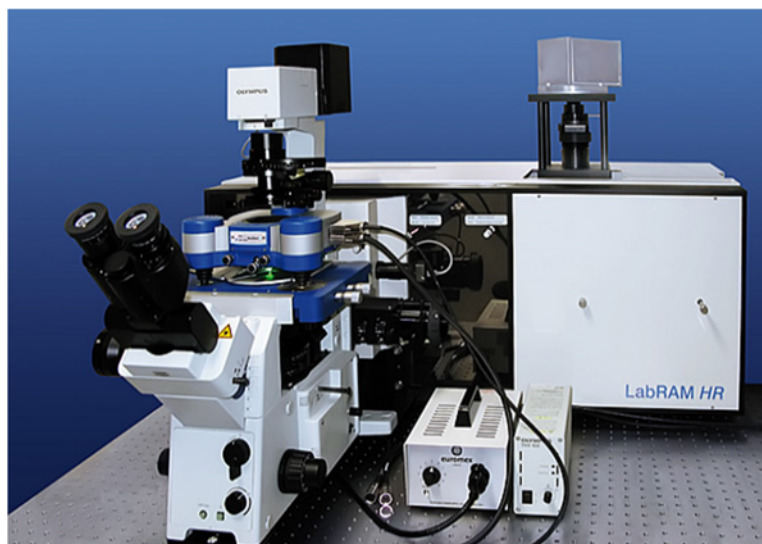
Figure 2.2 NanoWizard® 3 NanoOptics AFM system combined with a HORIBA Jobin Yvon Raman spectrometer for TERS
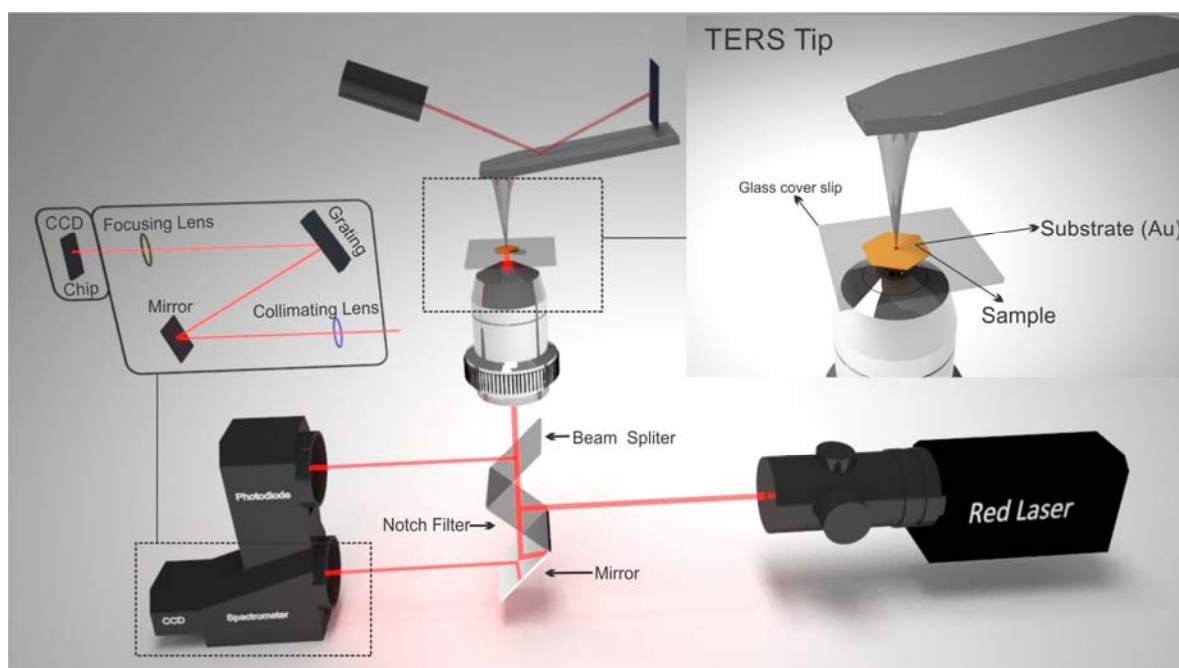
Figure 2.3 Scheme of the TERS setup used in this thesis. The backscattered light from the sample is collected using the same microscope objective, passes through the notch filter to reject the Rayleigh scattering and is final entering the spectrometer entrance slit prior to spectral analysis and detection.

2.2   Factors Affecting Raman Tip-enhancement

2.2.1   Fabrication of TERS Tips

The major challenge in performing successful TERS is to fabricate efficient and reproducible TERS active probes. Two factors should be considered when TERS probes are designed. First, the required conditions to excite localized surface plasmon should be fulfilled by choosing the right metal for a given excitation wavelength. Second, the shape and size of the tip apex should be optimized to improve the accessible spatial resolution.[23,24] The following sections discuss these issues in more detail. The selection of proper metal not only affects the excitation wavelength, but also the physical and chemical stability of the tip over time. Silver and gold are two suitable candidates for efficient enhancement on TERS experiment under visible light illumination. However, it should be noted that the dielectric functions of the two metals show significant difference in the UV-visible region under green (532 nm) and red (632.8 nm) excitation, respectfully. Silver is known to provide stronger enhancement compared to gold but it is quickly oxidized in air and need to be used rapidly after coating or protected using additional coating. [25,26] Most AFM tips used in TERS system are often based on commercial Si or Si_3N_4 tips that are subsequently coated by sputtering or evaporation methods. Typical layer thicknesses of 3-5 nm for the adhesion layer and 20-30 nm for the metallic layer are deposited to ensure a homogeneously coated tip.

2.2.2   Fabrication Methods

We describe here two fabrication methods of AFM tips including electrochemical etching of a metallic wire and physical deposition of a thin metal film over commercial

AFM tip.[27,28] We mainly used in this thesis coated tip but we have explored

electrochemical etching to fabricate gold tips.

Electrochemical Etching. Electrochemical etching has been widely used to

produce metallic probes for scanning force microscopy, in shear force microscopy and

STM, or even to produce whole gold cantilevers for AFM.[29] For TERS probe preparation,

gold or silver wires are materials that are generally sharpened using electrochemical

etching. To prepare gold tips, a voltage is applied between the gold wire (typically 100

μm diameter) and a gold ring electrode that surrounds the wire, while both wire and the

ring are immersed in concentrated hydrochloric acid and ethanol (1:1 V/V) electrolyte. In

a procedure proposed by Ren *et al.*[30] a gold ring of about 8 mm diameter made of 1 mm

thickness gold wire is placed on the surface of the etchant solution in a way that ¾ height

of the ring is immersed in the solution. Other than gold,[31] platinum[32,33] or carbon[34] rings

are also widely used in etching of gold wires. A gold wire of 0.25 mm thickness is then

immersed in the center of the gold ring so that 2-3 mm of the wire is inside the etchant

solution. Schematic of the etching reaction is presented in **Figure 2.4.** Upon applying the

voltage, a large surface tension is formed between the ring and the gold wire which

creates a meniscus on the surface[35] as depicted in **Figure 2.4.** The etching proceeds more

quickly within this meniscus region. During etching, a downward flow of $AuCl_4^-$ occurs

along the wire which results in a partial ion concentration gradient that decelerates the

etching of the lower portion of the wire. This leads into the necking of the wire near the

meniscus as shown in **Figure 2.4.**[36]
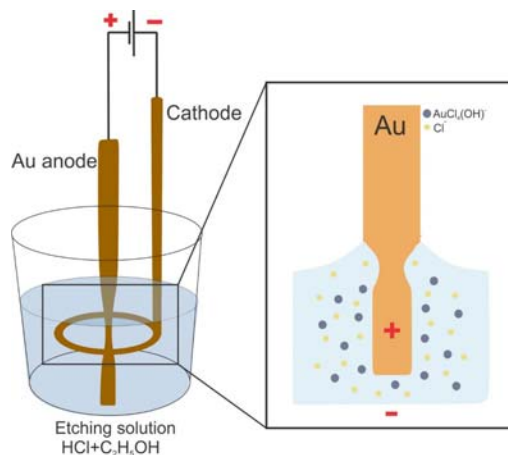
Figure 2.4 **The schematic diagram of the etching process for fabricating the gold tips. The gold wire is immersed through a floating cathode ring into the etching solution of HCl and ethanol[31].**

The mechanism of etching, which leads to dissolving of gold in concentrated HCl is shown in the following half-cell reactions:

Anode: (3.1) $2Au + 8Cl^- \longrightarrow 2AuCl_4^- + 6e^-$

Cathode: (3.2) $6H_3O^+ + 6e^- \longrightarrow 6H_2O + 3H_2$
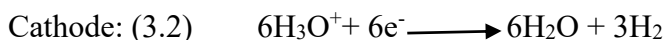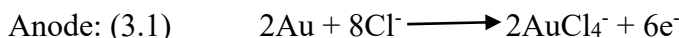
Near the interface between the gold wire and the etching solution, the half reaction at the anode results in consumption of a large amount and the depletion of Cl^-. Simultaneously, gold oxides will be formed on the wire, which passivates the gold surface and decreases the reaction current consequently. However, more Cl^- migrates from the bulk solution towards the gold wire, which enforces the dissolution of gold oxide as $AuCl_4^-$. This would expose the bare gold surface to HCl and thus increases the reaction current. For this reason the reaction current shows periodic changes upon the etching process. As the etching proceeds, the gold wire becomes thinner at a position below the meniscus until it breaks and the lower part of the wire falls down. The voltage should be shut off at this point. Fabrication of ideal TERS tip requires that a proper voltage is applied to the

etching reaction. Proper voltage causes a stable reaction current oscillation and higher

etching quality. Ren et al.[30] proposed that a positive voltage above 1.4 V with respect to a

standard calomel electrode should be applied. Nevertheless, higher voltages would

accelerate the reaction rates and lead to formation of O_2 and Cl_2 side products. Gaseous

species cause bubbling which roughens the surface of the tip. Addition of ethanol

however, decreases the chance of bubbling[34] because of the ethanol's low surface tension

(22.3 mN/m, for water this value is 71.9 mN/m) and results in formation of smoother

gold surfaces.[37]

For silver tips, two main etching methods are usually used. In the first method, the 0.25

mm diameter silver wire is immersed by 6 mm in 10-35% aqueous ammonia electrolyte

and a stainless steel plate is utilized as counter electrode. Etching reaction occurs when a

current flows through the electrolyte. No metal rings are required in this method. Here the

silver wire is manually removed with a 0.2 mm/min steps to form a cone on the body of

the wire. After 10 min the removal is stopped and the etching continues until the lower

part of the silver wire inside the etching solution drops. Tip apex radius of 50-100 nm can

be achieved by this method.[38] In the second method, 60% aqueous solution of perchloric

acid and ethanol (1:2 V/V) mixture is used. The silver wire is immersed at the center of a

silver ring that acts as cathode and as soon as a voltage of 1.5 V is applied the etching

reaction would begin. The apex size in this method ranges from 50 to 100 nm.[39] The

electrochemical etching of the tips can be performed by using alternating (AC) or direct

current (DC).[30-33,40-43] When DC voltage is applied, the electrochemical potential gradient

around the tip controls the etching process through controlling the ionic motion of the

electrolyte. Under DC voltage, mass transfer from the vicinity of the tip is controlled by

convection and electrochemical potential gradient such as diffusion and migration.[44] This process can however be haphazard and slow and therefore, sharpening of the tip may not necessarily occur in a clear and directional manner. On the contrary, under AC voltage a bubble will form during one half cycle which will be directionally forced upward by buoyancy. The etching rate is indeed controlled by the flow of this driving stream which removes the etched material from the vicinity of the tip. As opposed to normal etching where the bubble flow moves towards the tip shank, the flow moves away from the etched part of the tip which provides better conditions for formation of the tip. The presence of this bubbling flow has been evidenced through optical microscopy.[45] Nevertheless, when gold rings are used, AC voltages can be problematic due to the potential etching of the ring.[34] SEM image of a gold tip fabricated through AC and DC electrochemical etching of gold nanowires done by Marion Bouchet, a former undergraduate student in our research group, is presented in **Figure 2.5.**

The gold tip produced through applying 2.4 V AC voltage with 3 kHz frequency and 70 μsec/impulsion pulse rates is shown in **Figure 2.5a.** The method however yielded low reproducibility. Electrochemical etching of a gold wires using 2.4 V DC voltage resulted in fabrication of gold tip similar to the one shown in **Figure 2.5b** with good reproducibility. (1:1 V/V) mixture of HCl (37%) and ethanol (96%) was utilized as the etching solution in these series of experiments. Although these first results obtained in our group are promising, the integration of such AFM tips in an existing AFM holder is not trivial. Because of their wire-geometry these tips are usually mounted onto tuning fork requiring a specific feedback mechanism to maintain the tip close to the sample surface with minimized noise.
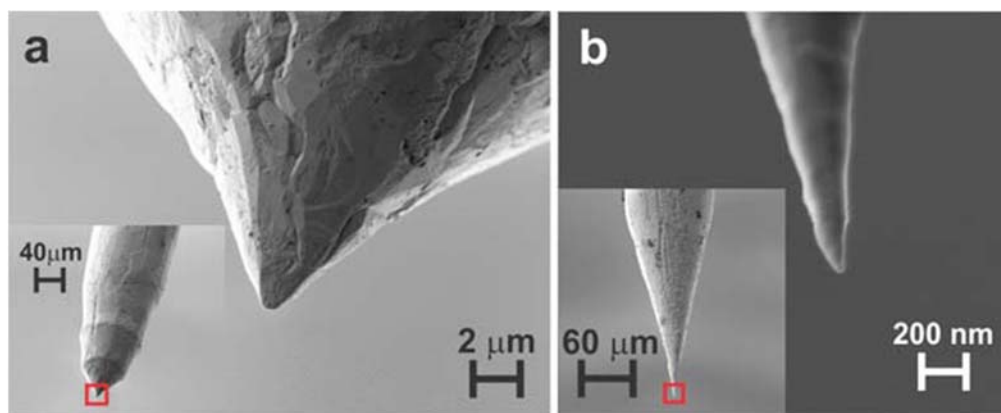
Figure 2.5 SEM image of gold tip etched inside the etching solution of (1:1 V/V) HCl and ethanol using (a) AC and (b) DC voltage

Metal Vapor Deposition. Using this approach, metal islands are created over a commercial AFM tip through thermal evaporation of the metal, which is induced by an electron beam inside a vacuum chamber.[9] Metal islands are essential for creating a "hot-spot" at the tip apex, which are necessary for TERS activity. Nevertheless, it has been shown that the presence of isolated metallic grain on the tip end may not guarantee the TERS activity and that a cluster of nanoparticles might be necessary.[24] However, if the cluster is too large it would have negative effects on the resolution of the TERS measurements even though the tips are TERS active. As a result there should be a balance between the thickness of the evaporated metal and the effort to get metallic islands at the tip end. 30 nm thicknesses have repeatedly resulted in good yield of producing active probes with proper apex sizes of sub-50 nm.[28,46-48] The deposition rate however should be experimentally tuned in accordance with the deposition conditions and more specifically the distance between the metal source and the tip inside the deposition chamber. This is due to the source temperature that can have a significant effect on the morphology and the quality of the resulting film through thermal annealing of the coating. In this thesis,

electron beam vapor deposition was utilized to coat non-contact tapping mode AFM

probes with gold or silver. The vapor deposition was done at the Western

Nanofabrication Facility at Western University. The coating of the tips was conducted by

electron beam induced thermal vapor deposition of around 5 nm titanium used as an

adhesion layer followed by 30 nm of gold or silver inside a vacuum chamber. The

deposition rate was set to 0.1 Å/sec to acquire a homogeneous layer of metallic grains.

Figure 2.6 shows the SEM images of the resulting coated tips.
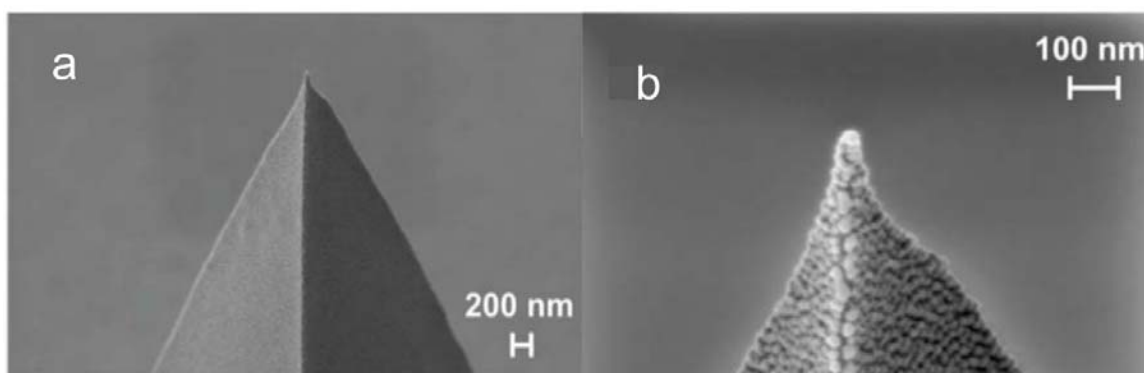
Figure 2.6 **SEM images of silver coated silicon tips (NCL tapping mode tips, Nano World TM. The coated layer includes 5 nm of titanium and 30 nm of silver. (a)- (b) present different magnification of the same image**

As shown in **Figure 2.6 b**, thermal vapor deposition provides a silver island at the tip

apex when optimized deposition conditions are applied. The silver grain size at the tip

apex has a diameter of around 30 nm. Typically one out of every five tips that got metal

coated for the TERS measurements exhibited TERS activity. This yield is acceptable and

comparable to the previously reported observations made by other research groups.[24,49,50]

2.2.3   TERS Tip Geometry

Sharper apexes should experience larger charge density which should leads to

larger local enhancement of the electric field. On the other hand, the size, shape and the

roughness of the metal coating deposited over the tip are parameters that also strongly

influence the enhancement of the electric field around the apex. Since in TERS the

spectral measurements originate from the tip apex, smaller tip apex results in

investigation of a smaller volume on the sample surface and therefore increased spatial

resolution.[21,51,52] The amount of defects and hence the sharpness of the apex could be

controlled during the tip preparation process only to some extent.[53] This explains the low

reproducibility of TERS active tips and variation of LSPR for the tips of similar

dimensions that are prepared using similar procedures. This could be problematic since

only stable plasmonic activity gives reliable and reproducible enhancement of the Raman

scattering and consequently a well resolved chemical imaging.[51] Two different tip

geometries are used in the current thesis depending on the experimental requirement. The

majority of the TERS measurements are conducted using tapping mode NCL50-silicon

tips from Nano-world[TM] **(Figure 2.7a)** or NSG-10 from NT-MDT **(Figure 2.7b)**

Typically, the shape of these tips is a polygon based pyramid with height of 10-16 μm

with radius of curvature of 6-10 nm.
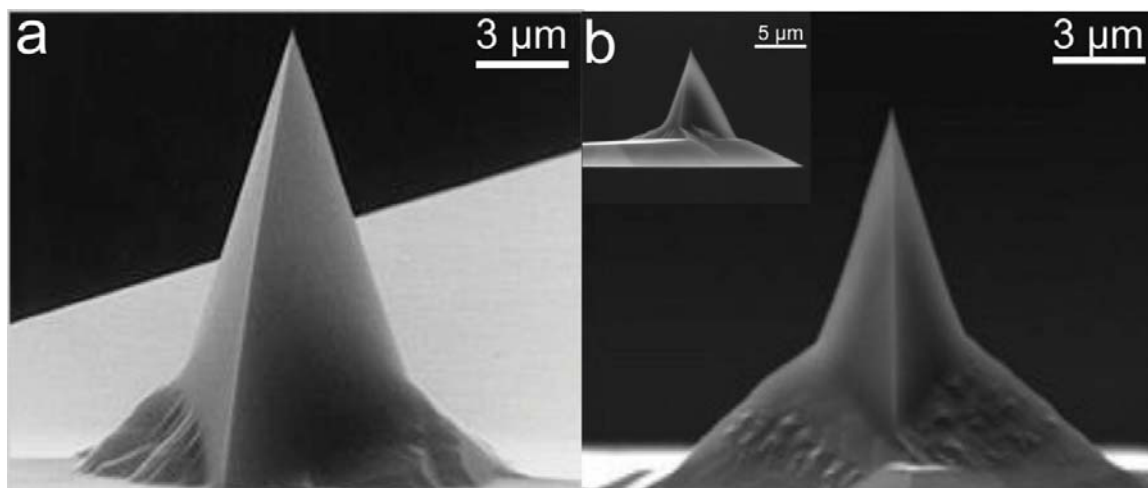
Figure 2.7 **SEM images of (a) silicon NCL tapping mode AFM tip (b) NSG-10**

2.2.4   Lifetime of a Tip: Chemical and Mechanical Degradation

Chemical degradations such as oxidation or adsorption of molecules or mechanical wear damages are two limiting factors of the lifetime of these probes. Chemical degradation is usually caused through reaction of ambient gases with the metal coating of the tip. For example, oxidation of silver with oxygen in the atmosphere typically lead to a decreasing of the enhancement within 24 h.[54] Other option to overcome this problem is using gold tips, but there is a trade-off of fewer enhancements. Coating with thin protection layer has also been investigated using protection with functionalization of the tip with organic monolayer or through the deposition of a thin film of silica or aluminum oxide.

To avoid chemical degradations, all the coated tips (silver or gold) used in current thesis were used within 24 h of preparation. In addition, after removal of the coated tips from the deposition chamber, the tips were stored in desiccators that were purged with nitrogen to minimize contact with more reactive ambient gases. Mechanical wear damages are typically caused upon usage and result in removal of the metal coating from the tip

apex.[55] Mechanical degradations can significantly alter the shape of the tip apex. An example is shown in **Figure 2.8**.
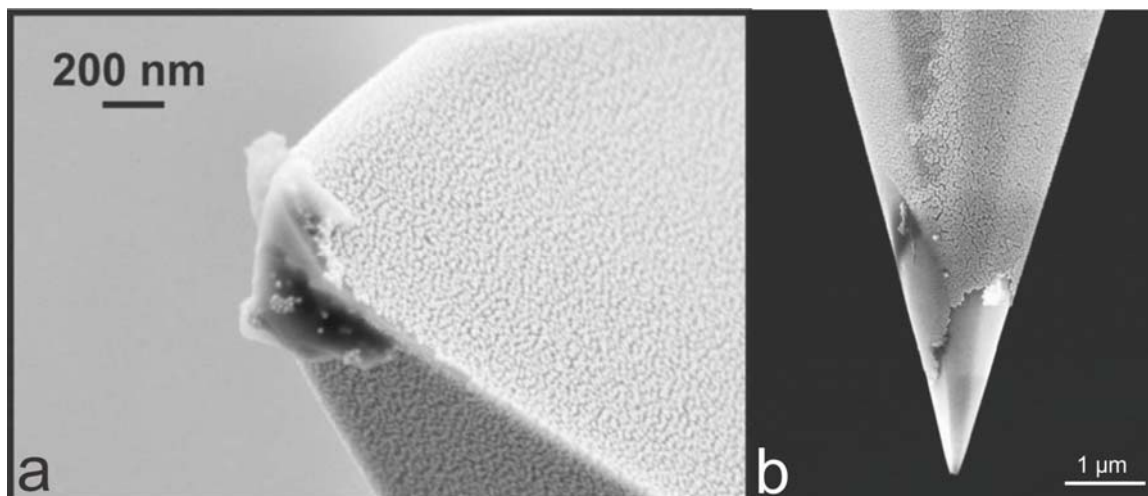
Figure 2.8 **Wearing off of the metal coating of a conventional silicon tip with (a) gold and (b) silver layer after the AFM-TERS experiment. The image (b) is obtained from reference 55 with permission from Review of Scientific Instruments.[56]**

The peeling of the metallic coat is usually due to the fact that the coating does not stick properly to the tip which results in the loss of sensitivity in TERS tip after conducting a few scans. Mechanical wear resistance of the tips could be enhanced upon coating with an additional thin layer of alumina or silicon oxide as reported in literature.[57,58] To decrease the chance of mechanical damages in the current thesis, AFM scans were conducted using certain parameters which minimize the tip-sample interaction. The AFM scan prior to TERS measurements were performed with low scan rates (~ 0.3 Hz/line) and low driving forces. Since these settings typically have negative influence on the resolution of the acquired AFM scans, higher quality AFM images were in some cases collected after the TERS measurements were completed. Other tip degradation source arises from laser-induced heating which, can effect in shape and morphology of the

nanostructure that well known in the literature.[56, 22] Overall, the TERS parameters must be adapted to the type of sample under investigation and spatial resolution may be affected by the type of sample as much as the type of tip used.

2.2.5   Substrate and gap-mode TERS

When using gap-mode TERS, the sample is sandwiched between two gold interfaces yielding better confinement and local enhancement in the order of 10^7.[59] This effect can only be observed if the tip-sample distance corresponds to the optical near-field region, i.e. within 10-20 nm from the surface.[60-64] The ideal substrate for gap-mode TERS must therefore be optically transparent, ultraflat and can be used for chemical immobilization.[65]

In this context, gold nanoplates have interesting optical properties, such as a plasmon mode that can couple with the localized surface plasmon of the tip upon proper excitation. Such plates initially used in combination with TERS experiment by the group of V. Deckert can be used as an ideal substrate for a variety of samples and applications.[66-69] The main issue when using gold substrate is opaqueness and absorption of the incident excitation light. The chemical synthesis of the gold nanoplates reported in Chapter 3 provides ultraflat plates together with ultra-smooth roughness which is ideal for the TERS experiments described hereafter.

2.3   Laser Polarization

As stated earlier the polarization of the excitation source must be correctly set to provide local enhancement in the vicinity of the metal tip. The magnitude of field enhancement strongly depends on the polarization of the incident laser with respect to the

tip axis thus requiring a large component of the polarized light along the tip axis.[70] In a

transmission setup with bottom illumination, the polarization component along the tip

axis when irradiated by a linearly polarized laser (Gaussian mode) is weak. Since the

polarization of the incident beam is perpendicular to the tip axis (**Figure 2.9a**), the free

electron of the metal are driven laterally with respect to the tip axis, providing no net

confinement of the changes at the tip apex. One way to overcome this problem is to

illuminate the tip with a linearly polarized beam coming from the side with a large

incident angle. With such polarization configuration, the changes are driven axially and

the results in a large accumulation of changes at the tip apex which in term provide a

large field enhancement.
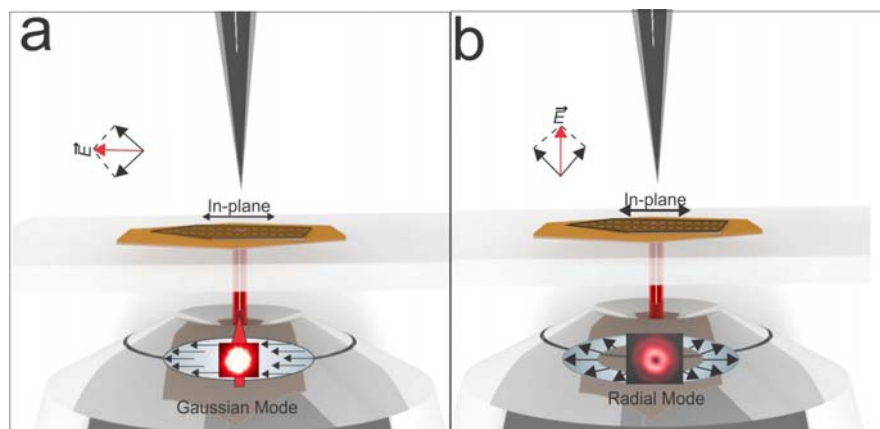
Figure 2.9 **(a) Interaction between a metalized tip and Gaussian transverse polarized mode creates no component along the tip axis (b) interaction between a metalized tip and radially polarized mode generates a field component along the tip axis**

In a transmission setup, it is possible to obtain a polarization component along the tip axis

when using radially polarized beam. A radially polarized beam is a beam whose electric

field vectors are radially polarized in the lateral plane perpendicular to the propagation

vector. At the center of the beam there is no net intensity and the cross section appears as

a ring as shown in **Figure 2.9b.** When such "doughnut" mode is focused with a high N.A.

objective, the radially polarized components recombine to yield a net polarization

component along the propagation direction at the focal plane. When such polarized

component interact with the metallic tip, at the excitation of the laser is confined at the

extremity of the tip yielding ideal experimental conditions for the TERS experiments.[71]

2.3.1   Experimental Setup to Generate Radial Polarization

Several approaches have been used to generate a radially polarized mode. Quabis

et al.[72] used four segmented half waveplates to generate a radially polarized beam. Each

of these four half waveplates are oriented in a way that their optical axis rotates the

incoming electric field to the points in the radial direction. Saito et al.[1] employed a radial

waveplate composed by orienting eight segmented half-wave plates with optical axes in

different directions in order to generate a radially polarized beam. These approaches

however, suffer from the complexity of fabrication including the cutting and assembly of

the wave plate segments. More importantly, the resulting wave plate is effective at a

single wavelength which restricts the application of the setup. Recently a liquid crystal

(LC) modulator was developed (Arcoptix^{TM}, Switzerland) to generate a radially polarized

beam that can be tuned for a wide range of wavelengths between 350 to 1700 nm. The

general configuration of LC modulators is shown in **Figure 2.10** LC modulators consist

of a polarization convertor (θ-cell), a phase compensator that allows $\lambda/2$ phase step

between the upper and the lower half of the θ-cell and a twisted nematic cell to rotate the

entrance polarization by 90° and permit to switch between an azimuthally and radially

polarized outputs.
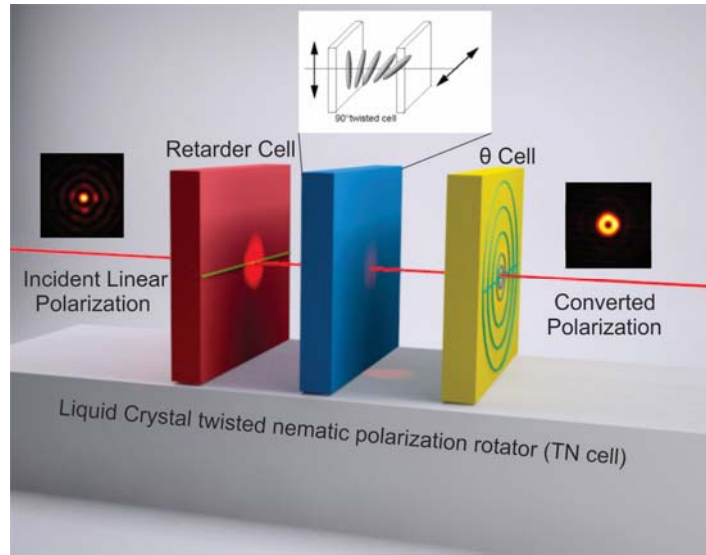
Figure 2.10 Liquid crystal polarization modulator configuration. A linearly polarized light enters from the left sidet into the phase compensator. The electric field vectors might be rotated by the nematic cell and the light will exit with a radially or azimuthally polarization from the θ-cell.

The top half of the phase compensator (black line across the phase compensator (retarder cell in **Figure 2.10**) has an electrode that permits changing of the inclination angle of its liquid crystal molecules, which changes its extraordinary refraction index. By applying a bias on the electrode the retardation is reduced compared to the bottom half where the retardance stays constant. As a result, the light phase in lower half of the compensator is different from the upper half by a λ/2 step. The function of the twisted nematic is also based on the precisely controlled alignment of liquid crystal molecules between different ordered molecular configurations under the action of operating voltages. When the nematic cell is switched off, light does not experience any polarization rotation. A switched-on nematic cell however, rotates the polarization by 90° angle.[73] In a θ-cell, the entrance and the exit plates are linearly and circularly rubbed, respectively, and the cell axis is at the direction of the linearly rubbed entrance plate. A linearly polarized beam that enters the θ-cell has an electric field parallel or perpendicular to the cell axis. The

polarization conversion for each of the two inputs is summarized in **Figure 2.11.** Light

with polarization perpendicular to the cell axis will be radially polarized when it exits the

cell **(Figure 2.11a).**[74] If the polarization of the input light is parallel to the cell axis, the

output light will be azimuthally polarized **(Figure 2.11b)**.
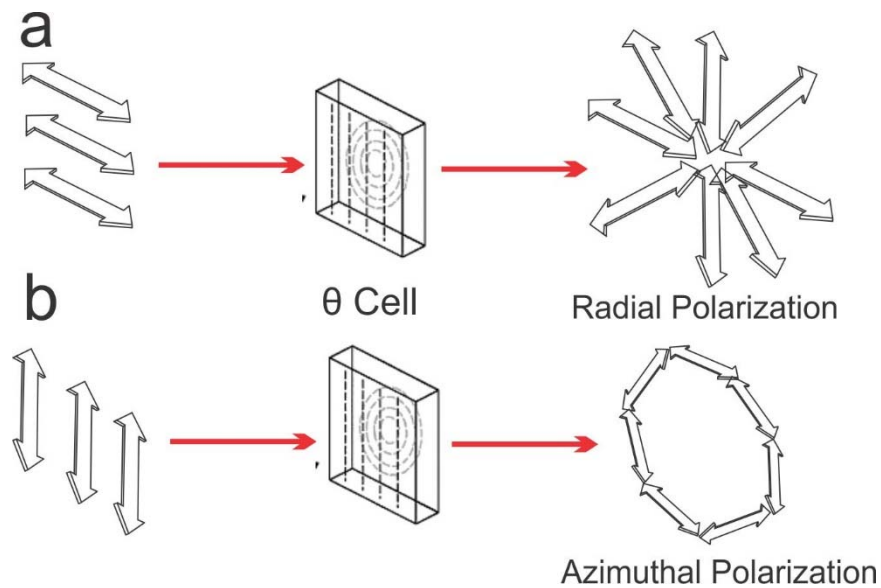
Figure 2.11(a) Radially (b) Azimuthally polarized light generated by θ-cell.

The experimental setup used in this thesis to generate radial and azimuthal polarization

consists in the following elements. A liquid crystal convertor along with other optical

elements such as mirrors, pinholes, lenses and optical spatial filters are utilized. An

optical spatial filter is a combination of a microscope objective and a pinhole. The

relative position of the objective and the pinhole should be optimized to create a

homogeneous Gaussian and parallel beam. Any convergence or divergence of the laser

beam must be corrected in the light path. A pair of converging and diverging lenses

(convex and concave lenses) is utilized to downsize the beam diameter by a factor of two.

Smaller beam cross sections are more easily matched with the entrance aperture of high

numerical aperture microscope objectives in TERS setup. Adjustable diaphragms are used to homogenize the beam by cutting out the interferences of back reflected light from the various optical elements. Additional lenses and pinholes might be necessary in order to adjust the size of the beam diameter before it enters the microscope. A CCD camera can be used to evaluate the quality of the laser beam during installation of the setup. An optical image of the radially polarized output of the above setup at the CCD camera and also at the focal point of a 1.4 N.A. oil immersion objective is presented in **Figure 2.12.** These images correspond to a radially polarized 632.8 nm red laser (**Figure 2.12a and c**) and 532 nm green laser **(Figure 2.12b and d).**
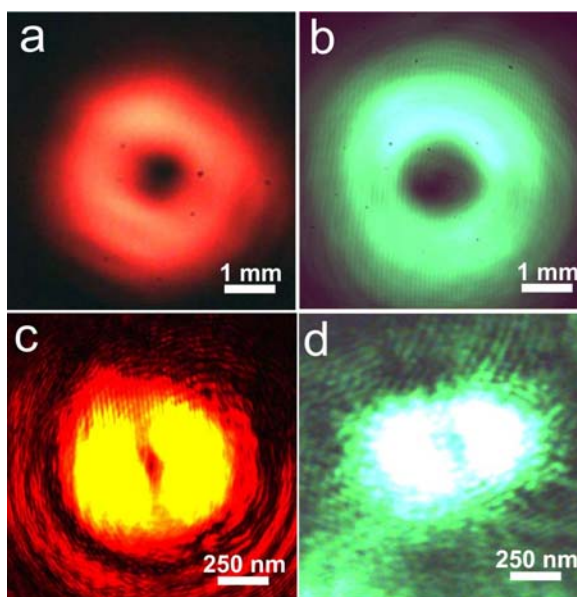
Figure 2.12 Radially polarized (a) 632.8 nm laser projected at a CCD camera before reaching the microscope objective(b) 532 nm laser projected at a CCD camera before reaching the microscope objective(c) 632.8 nm laser focused by a x100 oil immersion objective with N.A.=1.4 (d) 532 nm laser focused by a x100 oil immersion objective with N.A.=1.4

As shown in **Figure 2.12c** and d, a high numerical aperture microscope objective could decrease the beam diameter at focal point to around 1 μm. Imperfections in the shape of

the beam (more specifically in **Figure 2.12d)** are due to phase lags caused by the multiple optical elements located on the optical path. It is noteworthy that the middle part of the doughnut which appears black in **Figure 2.12c** (dark in **Figure 2.12d**) contains the z component of the polarization. Although the intensity of this component is less than the xy components (bright areas in same image), it would get magnified by several orders of magnitude once the TERS tip interacts with the center of this doughnut mode.

2.4   TERS Experimental Procedure

To perform a TERS measurement, the sample should be deposited over a transparent substrate which also does not absorb significantly the Raman excitation laser used for the study. Thin glass or amorphous quartz cover slips are generally ideal for this purpose due to their compatibility with high numerical aperture oil immersion objectives. The sample should be deposited on the substrate in a way that it is facing upwards. This is the only way that the TERS tip approaching from above could sense the sample surface in bottom illumination TERS configuration. The TERS procedure will be described in detail in the following sections.

2.4.1   Alignment of the TERS Tip to the Laser Focal Region

Prior to any TERS experiments, it is necessary to align the TERS tip with the focused laser spot. Consequently, it is essential to exactly determine the position of the tip apex on the cantilever in order to align it with respect to the focal point of a tightly focused excitation laser. The two approaches that can be used to perform such alignment are summarized in the following sections.

First, the scattered signal from the AFM tip can be detected by a photodiode showing that the extremity of the tip scatters largely the laser light **(Figure 2.13)**. Second, the vertical deflection of an AFM tip from the focused laser can be monitored. The absorption of a tightly focused laser produce thermal fluctuations that can be sensed by an AFM tip scanning the focal region. **(Figure 2.14a)**. Last, the Raman intensity map in **Figure 2.14b** is generated by integration of the Raman signals of the strong Silicon band of the non-contact tip (Type NGS10, silicon tip). Even though the tip is coated with a 20 nm thick layer of gold, scattering of silicon is yet effective and can readily be detected. The preliminary alignement is first done with mechanical positioning of the AFM tip over the focal region. The precise alignment is then done using piezoelectric actuators that provides lateral positioning of the tip above the focal spot with sub-nanometer resolution. Once the alignment is done the position of the tip within the laser spot remains unchanged and only the sample, fixed to its own X,Y piezo stage, is moved independently.

2.4.2 Tip Alignment by Rayleigh Scattering Collection

In this method the TERS tip is scanned over the tightly focused Raman laser while it is in feedback with the sample surface. As the laser illuminates the tip it is back-scattered from the tip apex. The back-scattered light gets collected by a photodiode which is connected to an input channel on the AFM controller box.[75] This generates an image of the cantilever similar to what is shown in **Figure 2.13**.
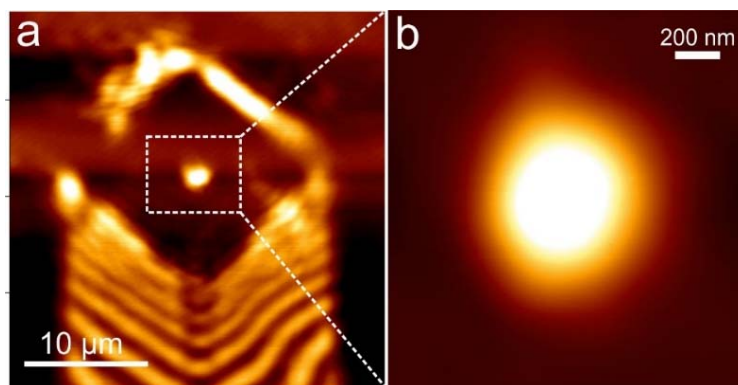
Figure 2.13 Tip alignment based on the collection of the Rayleigh scattering from the cantilever. (a) and (b) are images of an area around the tip apex proximity recorded with different zoom

In this figure, the tip apex position appears as a bright spot on the acquired image reflecting a higher scattering center. Smaller scan area and lower scan rate in general create images with better qualities where the tip apex position is estimated to be at the center of an area with 500 nm diameter. It is noteworthy that this bright area indicates the coupling of near-field scatterings into the far-field. Hence, similar spots might be detected simultaneously from other positions on the cantilever that should not be mistaken for the tip position. Since the tip is typically located in a symmetrical distance from the edges of the cantilever, the optical images of a larger area on the cantilever, similar to the image in **Figure 2.13a**, should help to discriminate other bright spots from the tip location. Meanwhile, if the tip position is not determined correctly and it is mistaken by a second bright spot on the Rayleigh scattering image, no TERS activity will be observed.

2.4.3   Tip Alignment by Raman Spectra Collection

An alternative method for alignment of the tip with respect to the Raman laser is to collect the Raman spectra of the cantilever and the tip. In this method, the vertical

deflection image of the cantilever is first collected, which shows the overall shape of the cantilever as well as the approximate tip position (**Figure 2.14a**). Once the rough position of the tip is found, Raman spectra of an area on the cantilever around the tip position are collected. The collected Raman spectra are then used to generate a Raman map of the cantilever (**Figure 2.14b**). The creation of the map is done through integration of the area below a characteristic peak in the Raman spectrum of the cantilever. For example for silicon tips the intense peak at 520 cm^{-1}, corresponding to the first optical phonon mode of silicon, is used. On this color coded map that indicates the variation of intensity of the 520 cm^{-1} mode, the position of the apex appears as a most intense pixel.
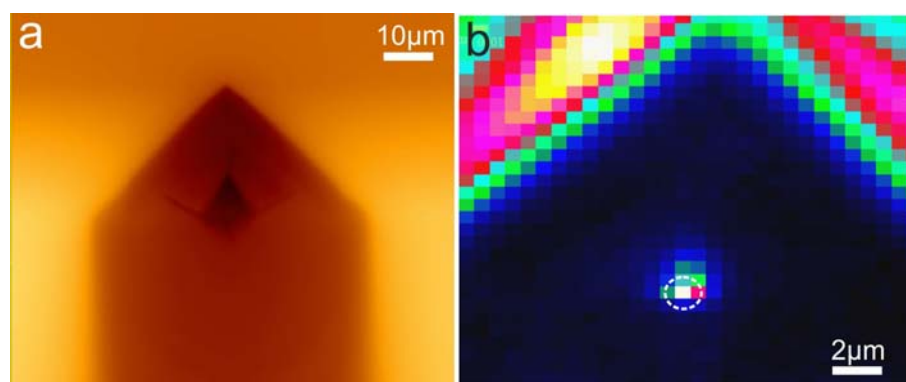
Figure 2.14 **Tip alignment by Raman spectra collection (a) image of the cantilever generated by light reflection caused by vertical deflection of the tip upon interacting with the laser (b) Raman map generated by integrating the Raman intensity in the [515-525]cm^{-1} spectral range. The pixel with the larger intensity indicates the tip location (indicated by a dashed circle in (b)).**

This method is more time consuming compared to Rayleigh scattering alignment. It is noteworthy that during the alignment process, the position of the cantilever along the z direction also gets optimized. For this purpose the thickness of the sample must be taken into account. If the thickness of the sample is more than 50 nm, the alignment process could not be done on the substrate because the z position of the tip during the TERS

measurements on the sample surface would be different from the alignment process. For this reason, when working with thicker samples, tip alignment must be carried out on top of the sample surface. However, for thinner samples, doing the alignment on the sample surface or on the substrate should not cause a significant inaccuracy. Extra care should be taken to ensure that the cantilever position along the x and y direction doesn't change during the experiment. For this reason, mechanical vibrations should be minimized in the room where the TERS measurements are being performed.

2.5   Estimation of the Enhancement Factors in TERS

Enhancement factor (EF) estimation can be determined from the TERS experiments and can be used to judge the local enhancement of the measurement for a given sample in a given geometry.[76] This factor depends on multiple factors including the experimental conditions, sample properties and preparation and ultimately, the efficiency of the TERS tip. Such enhancement is not straightforward to estimate since it needs a reliable reference and non-enhanced spectrum of the same sample. Accordingly, in the TERS literature variation of the enhancement factor reported ranges between 30 to of 10^{13}.[77,78] To calculate the enhancement factor from a given measurement, two factors should be determined. On the one hand, the spectroscopic contrast C which is a comparison between the Raman peak intensities when the tip is in contact (in near-field of the sample) and the intensities when tip is retracted (in far-field of the sample). This contrast is provided by: [Eq.2][79]

$$ C = \frac{I_{near\,field}}{I_{far\,field}} = \frac{I_{TERS} - I_{retracted}}{I_{retracted}} \qquad [2] $$

The second factor is the geometry factor that is critical to evaluate the contributions of

the far-field and near-field scattering volumes. Due to the relatively large dimensions of

laser cross-section, even when high numerical objectives are used, the investigated area

in far-field is much larger than the area that is illuminated by the tip in near-field. For this

reason the difference between the illuminated volumes in near- and far- fields should be

considered for the estimation of the experimental enhancement factor. In case of very thin

samples the volume could be replaced with area of the illumination. The far-field

scattering originate from the entire focal region of the laser therefore, $A_{\text{far field}} = r_{laser}^2 \times \pi$

with r_{laser}^2 being the radius of the laser cross-section. The area from where the near-field

signal arises can be estimated as $A_{\text{near field}} = r_{tip}^2 \times \pi$ with r_{tip}^2 being the radius of the tip.[23]

By considering the source volume, the enhancement factor of TERS can be defined

through the following equation: [Eq. 3]

$$EF_{TERS} = C \frac{A_{far\,field}}{A_{near\,field}} \quad [3]$$

Nevertheless, for a reliable comparison of various experiments, the method used for

calculation of the enhancement factor should be carefully considered. Since the Raman

intensity varies with the scattering cross-section of the sample, this enhancement has to

be considered with caution because it is sample dependent.[16,80-82]

2.6   TERS Vibrational Assignment

TERS peaks are commonly compared to conventional Raman bands; however,

presence or absence of bands, variation of their intensities and shapes should be closely

investigated. Due to the localized enhancement, TERS is a surface specific technique and

is therefore sensitive to the orientation of the Raman modes. Although the positions of the Raman bands are usually similar in TERS and conventional Raman, the intensity of the individual bands can vary significantly.[83]

2.7   Conclusion

In summary, tip-enhanced Raman spectroscopy (TERS) is a highly sensitive spectroscopic technique which combines the spatial resolution of scanning near-field techniques with the chemical specificity of vibrational spectroscopy which makes TERS a unique method to explore the nano-world. Considering its spatial resolution that surpasses the Abbe's diffraction limit of $\lambda/2$, nanoscale objects with dimensions in the 10-20 nm can be investigated with TERS. The magnitude and reproducibility of the enhancement, lateral resolution and the lifetime of the TERS tip are among the issues that remain problematic. A universal and inclusive application of the method suffers from the lack of reliable tip fabrication methods with the goal to increase the tip's TERS activity and the yield of tip reproducibility. This low reproducibility restricts the direct comparison between the TERS studies that are performed in different research groups. Despite all the challenges, TERS has shown great potential for chemical imaging of the surfaces of a large variety of the samples. At present, there is no other option at nanometer scale study to provide molecular recognition through the analysis of their fingerprints. TERS is very powerful technique that can provide information complementary to other surface specific tools such as SEM or XPS. The following Chapters report on selected examples of the applications of TERS in material and biomaterial research.

2.8   References

(1)   Saito, Y.; Kobayashi, M.; Hiraga, D.; Fujita, K.; Kawano, S.; Smith, N. I.; Inouye, Y.; Kawata, S., z-Polarization sensitive detection in micro-Raman spectroscopy by radially polarized incident light. *J. Raman Spectrosc.* **2008**, *39*, 1643.

(2)   Hayazawa, N.; Saito, Y.; Kawata, S., Detection and characterization of longitudinal field for tip-enhanced Raman spectroscopy. *Appl. Phys. Lett.* **2004**, *85*, 6239.

(3)   Yu, J.; Saito, Y.; Ichimura, T.; Kawata, S.; Verma, P., Far-field free tapping-mode tip-enhanced Raman microscopy. *Appl. Phys. Lett.* **2013**, *102*, 123110.

(4)   Rasmussen, A.; Deckert, V., Surface- and tip-enhanced Raman scattering of DNA components. *J. Raman Spectrosc.* **2006**, *37*, 311.

(5)   Wood, B. R.; Bailo, E.; Khiavi, M. A.; Tilley, L.; Deed, S.; Deckert-Gaudig, T.; McNaughton, D.; Deckert, V., Tip-Enhanced Raman Scattering (TERS) from Hemozoin Crystals within a Sectioned Erythrocyte. *Nano Lett.* **2011**, *11*, 1868.

(6)   Pluk, H.; Stokes, D. J.; Lich, B.; Wieringa, B.; Fransen, J., Advantages of indium–tin oxide-coated glass slides in correlative scanning electron microscopy applications of uncoated cultured cells. *J. Microsc.* **2009**, *233*, 353.

(7)   Pettinger, B.; Picardi, G.; Schuster, R.; Ertl, G., Surface-enhanced and STM-tip-enhanced Raman spectroscopy at metal surfaces. *Single Mol.* **2002**, *3*, 285.

(8)   Deckert-Gaudig, T.; Deckert, V., Ultraflat transparent gold nanoplates - ideal substrates for tip-enhanced Raman scattering experiments. *Small* **2009**, *5*, 432.

(9)   De Angelis, F.; Das, G.; Candeloro, P.; Patrini, M.; Galli, M.; Bek, A.; Lazzarino, M.; Maksymov, I.; Liberale, C.; Andreani, L. C.; Di Fabrizio, E., Nanoscale chemical mapping using three-dimensional adiabatic compression of surface plasmon polaritons. *Nat. Nanotechnol.* **2010**, *5*, 67.

(10)   Wang, P.; Zhang, D.; Li, L.; Li, Z.; Zhang, L.; Fang, Y., Reversible Defect in Graphene Investigated by Tip-Enhanced Raman Spectroscopy. *Plasmonics* **2012**, *7*, 555.

(11)   Stadler, J.; Schmid, T.; Opilik, L.; Kuhn, P.; Dittrich, P. S.; Zenobi, R., Tip-enhanced Raman spectroscopic imaging of patterned thiol monolayers. *Beilstein J. Nanotechnol.* **2011**, *2*, 509.

(12)   Bek, A.; De Angelis, F.; Das, G.; Di Fabrizio, E.; Lazzarino, M., Tip enhanced Raman scattering with adiabatic plasmon focusing tips. *Micron* **2011**, *42*, 313.

(13)   Chan, K. L. A.; Kazarian, S. G., Tip-enhanced Raman mapping with top-illumination AFM. *Nanotechnology* **2011**, *22*, 175701.

(14)   Nieman, L. T.; Krampert, G. M.; Martinez, R. E., An apertureless near-field scanning optical microscope and its application to surface-enhanced Raman spectroscopy and multiphoton fluorescence imaging. *Rev. Sci. Instrum.* **2001**, *72*, 1691.

(15)   Neacsu, C. C.; Dreyer, J.; Behr, N.; Raschke, M. B., Scanning-probe Raman spectroscopy with single-molecule sensitivity. *Phys. Rev. B: Condens. Matter Mater. Phys.* **2006**, *73*, 193406/1.

(16)   Pettinger, B.; Ren, B.; Picardi, G.; Schuster, R.; Ertl, G., Nanoscale Probing of Adsorbed Species by Tip-Enhanced Raman Spectroscopy. *Phys. Rev. Lett.* **2004**, *92*, 096101/1.

(17)   Mehtani, D.; Lee, N.; Hartschuh, R. D.; Kisliuk, A.; Foster, M. D.; Sokolov, A. P.; Maguire, J. F., Nano-Raman spectroscopy with side-illumination optics. *J. Raman Spectrosc.* **2005**, *36*, 1068.

(18)   Saito, Y.; Motohashi, M.; Hayazawa, N.; Iyoki, M.; Kawata, S., Nanoscale characterization of strained silicon by tip-enhanced Raman spectroscope in reflection mode. *Appl. Phys. Lett.* **2006**, *88*, 143109/1.

(19)   Roth, R. M.; Panoiu, N. C.; Adams, M. M.; Osgood, R. M.; Neacsu, C. C.; Raschke, M. B., Resonant-plasmon field enhancement from asymmetrically illuminated conical metallic-probe tips. *Opt Express* **2006**, *14*, 2921.

(20)   Anderson, M. S.; Pike, W. T., A Raman-atomic force microscope for apertureless-near-field spectroscopy and optical trapping. *Rev. Sci. Instrum.* **2002**, *73*, 1198.

(21)   Yang, Z.; Aizpurua, J.; Xu, H., Electromagnetic field enhancement in TERS configurations. *J. Raman Spectrosc.* **2009**, *40*, 1343.

(22)   Berweger, S.; Raschke, M. B., Signal limitations in tip-enhanced Raman scattering: the challenge to become a routine analytical technique. *Anal. Bioanal. Chem.* **2010**, *396*, 115.

(23)   Stadler, J.; Schmid, T.; Zenobi, R., Developments in and practical guidelines for tip-enhanced Raman spectroscopy. *Nanoscale* **2012**, *4*, 1856.

(24)   Asghari-Khiavi, M.; Wood, B. R.; Hojati-Talemi, P.; Downes, A.; McNaughton, D.; Mechler, A., Exploring the origin of tip-enhanced Raman scattering; preparation of efficient TERS probes with high yield. *J. Raman Spectrosc.* **2012**, *43*, 173.

(25)   Johnson, P. B.; Christy, R. W., Optical Constants of the Noble Metals. *Phys. Rev. B* **1972**, *6*, 4370.

(26)   Johnson, P. B.; Christy, R. W., Optical constants of the noble metals. *Phys. Rev. B* **1972**, *6*, 4370.

(27)   Hayazawa, N.; Inouye, Y.; Sekkat, Z.; Kawata, S., Metallized tip amplification of near-field Raman scattering. *Opt. Commun.* **2000**, *183*, 333.

(28)   Stockle, R. M.; Suh, Y. D.; Deckert, V.; Zenobi, R., Nanoscale chemical analysis by tip-enhanced Raman spectroscopy. *Chem. Phys. Lett.* **2000**, *318*, 131.

(29)   Rodriguez, R. D.; Anne, A.; Cambril, E.; Demaille, C., Optimized hand fabricated AFM probes for simultaneous topographical and electrochemical tapping mode imaging. *Ultramicroscopy* **2011**, *111*, 973.

(30)   Ren, B.; Picardi, G.; Pettinger, B., Preparation of gold tips suitable for tip-enhanced Raman spectroscopy and light emission by electrochemical etching. *Rev. Sci. Instrum.* **2004**, *75*, 837.

(31)   Kharintsev, S. S.; Hoffmann, G. G.; Fishman, A. I.; Salakhov, M. K., Plasmonic optical antenna design for performing tip-enhanced Raman spectroscopy and microscopy. *J. Phys. D: Appl. Phys.* **2013**, *46*, 145501.

(32)   Park, J.; Hong, T. S.; Lee, N. S.; Kim, K. B.; Seo, Y., Viscosity dependence of electrochemical etching for gold tip fabrication. *Curr. Appl. Phys* **2011**, *11*, 1332.

(33)   Williams, C.; Roy, D., Fabrication of gold tips suitable for tip-enhanced Raman spectroscopy. *J. Vac. Sci. Technol., B: Microelectron. Nanometer Struct.--Process., Meas., Phenom.* **2008**, *26*, 1761.

(34)   Eligal, L.; Culfaz, F.; McCaughan, V.; Cade, N. I.; Richards, D., Etching gold tips suitable for tip-enhanced near-field optical microscopy. *Rev. Sci. Instrum.* **2009**, *80*, 033701.

(35)   Bailo, E.; Deckert, V., Tip-enhanced Raman scattering. *Chem. Soc. Rev.* **2008**, *37*, 921.

(36)   Neacsu, C. C.; Berweger, S.; Raschke, M. B., Tip-Enhanced Raman Imaging and Nanospectroscopy: Sensitivity, Symmetry, and Selection Rules. *NanoBiotechnology* **2009**, *3*, 172.

(37)   Lehmann, V. In *Electrochemistry of Silicon*; Wiley-VCH Verlag GmbH: 2002, p 183.

(38)   Dickmann, K.; Demming, F.; Jersch, J., New etching procedure for silver scanning tunneling microscopy tips. *Rev. Sci. Instrum.* **1996**, *67*, 845.

(39)   Zhu, L.; Atesang, J.; Dudek, P.; Hecker, M.; Rinderknecht, J.; Ritz, Y.; Geisler, H.; Herr, U.; Geer, R.; Zschech, E., Experimental challenges for approaching local strain determination in silicon by nano-Raman spectroscopy. *Mater. Sci.-Pol.* **2007**, *25*, 19.

(40)   Lopes, M.; Toury, T.; de La Chapelle, M. L.; Bonaccorso, F.; Giuseppe Gucciardi, P., Fast and reliable fabrication of gold tips with sub-50 nm radius of curvature for tip-enhanced Raman spectroscopy. *Rev. Sci. Instrum.* **2013**, *84*, 073702.

(41)   Gingery, D.; Buhlmann, P., Single-step electrochemical method for producing very sharp Au scanning tunneling microscopy tips. *Rev. Sci. Instrum.* **2007**, *78*, 113703/1.

(42)   Nicklaus, M.; Nauenheim, C.; Krayev, A.; Gavrilyuk, V.; Belyaev, A.; Ruediger, A., Note: Tip enhanced Raman spectroscopy with objective scanner on opaque samples. *Rev. Sci. Instrum.* **2012**, *83*, 066102/1.

(43)   Xu, G.; Liu, Z.; Xu, K.; Zhang, Y.; Zhong, H.; Fan, Y.; Huang, Z., Constant current etching of gold tips suitable for tip-enhanced Raman spectroscopy. *Rev. Sci. Instrum.* **2012**, *83*, 103708/1.

(44)   Fotino, M., Tip sharpening by normal and reverse electrochemical etching. *Rev. Sci. Instrum.* **1993**, *64*, 159.

(45)   Fotino, M., Nanotips by reverse electrochemical etching. *Appl. Phys. Lett.* **1992**, *60*, 2935.

(46)   Bailo, E.; Deckert, V., Tip-enhanced Raman spectroscopy of single RNA strands: towards a novel direct-sequencing method. *Angew. Chem., Int. Ed.* **2008**, *47*, 1658.

(47)   Schmid, T.; Burkhard, J.; Yeo, B.-S.; Zhang, W.; Zenobi, R., Towards chemical analysis of nanostructures in biofilms I: imaging of biological nanostructures. *Anal. Bioanal. Chem.* **2008**, *391*, 1899.

(48)   Watanabe, H.; Ishida, Y.; Hayazawa, N.; Inouye, Y.; Kawata, S., Tip-enhanced near-field Raman analysis of tip-pressurized adenine molecule. *Physical Review B* **2004**, *69*, 155418.

(49)   Cui, X.; Zhang, W.; Yeo, B.-S.; Zenobi, R.; Hafner, C.; Erni, D., Tuning the resonance frequency of Ag-coated dielectric tips. *Opt. Express* **2007**, *15*, 8309.

(50)   Yeo, B.-S.; Schmid, T.; Zhang, W.; Zenobi, R., Towards rapid nanoscale chemical analysis using tip-enhanced Raman spectroscopy with Ag-coated dielectric tips. *Anal. Bioanal. Chem.* **2007**, *387*, 2655.

(51)   Deckert-Gaudig, T.; Deckert, V., Tip-enhanced Raman scattering (TERS) and high-resolution bio nano-analysis-a comparison. *Phys. Chem. Chem. Phys.* **2010**, *12*, 12040.

(52)   Zhang, W.; Cui, X.; Martin, O. J. F., Local field enhancement of an infinite conical metal tip illuminated by a focused beam. *J. Raman Spectrosc.* **2009**, *40*, 1338.

(53)   Roy, D.; Williams, C. M.; Mingard, K., Single-crystal gold tip for tip-enhanced Raman spectroscopy. *J. Vac. Sci. Technol., B: Nanotechnol. Microelectron.: Mater., Process., Meas., Phenom.* **2010**, *28*, 631.

(54)   Barrios, C. A.; Malkovskiy, A. V.; Hartschuh, R. D.; Kisliuk, A. M.; Sokolov, A. P.; Foster, M. D., Extending lifetime of plasmonic silver structures designed for high-resolution chemical imaging or chemical and biological sensing. *Proc. SPIE* **2008**, *6954*, 69540C/1.

(55)   Barrios, C. A.; Malkovskiy, A. V.; Kisliuk, A. M.; Sokolov, A. P.; Foster, M. D., Highly Stable, Protected Plasmonic Nanostructures for Tip Enhanced Raman Spectroscopy. *J. Phys. Chem. C* **2009**, *113*, 8158.

(56)   Rodriguez, R. D.; Sheremet, E.; Mueller, S.; Gordan, O. D.; Villabona, A.; Schulze, S.; Hietschold, M.; Zahn, D. R. T., Compact metal probes: A solution for atomic force microscopy based tip-enhanced Raman spectroscopy. *Rev. Sci. Instrum.* **2012**, *83*, 123708/1.

(57)   Kumar, N.; Stephanidis, B.; Zenobi, R.; Wain, A. J.; Roy, D., Nanoscale mapping of catalytic activity using tip-enhanced Raman spectroscopy. *Nanoscale* **2015**, *7*, 7133.

(58)   Steffens, C.; Leite, F. L.; Bueno, C. C.; Manzoli, A.; Herrmann, P. S. D. P., Atomic Force Microscopy as a tool applied to nano/biosensors. *Sensors* **2012**, *12*, 8278.

(59)   Futamata, M.; Maruyama, Y.; Ishikawa, M., Local Electric Field and Scattering Cross Section of Ag Nanoparticles under Surface Plasmon Resonance by Finite Difference Time Domain Method. *J. Phys. Chem. B* **2003**, *107*, 7607.

(60)   Verma, P.; Yamada, K.; Watanabe, H.; Inouye, Y.; Kawata, S., Near-field Raman scattering investigation of tip effects on C60 molecules. *Phys. Rev. B: Condens. Matter Mater. Phys.* **2006**, *73*, 045416/1.

(61)   Zhang, W.; Yeo, B. S.; Schmid, T.; Zenobi, R., Single Molecule Tip-Enhanced Raman Spectroscopy with Silver Tips. *J. Phys. Chem. C* **2007**, *111*, 1733.

(62)   Zhang, W.; Cui, X.; Yeo, B.-S.; Schmid, T.; Hafner, C.; Zenobi, R., Nanoscale Roughness on Metal Surfaces Can Increase Tip-Enhanced Raman Scattering by an Order of Magnitude. *Nano Lett.* **2007**, *7*, 1401.

(63)   Zhang, W.; Schmid, T.; Yeo, B.-S.; Zenobi, R., Near-Field Heating, Annealing, and Signal Loss in Tip-Enhanced Raman Spectroscopy. *J. Phys. Chem. C* **2008**, *112*, 2104.

(64)   Nordlander, P.; Oubre, C.; Prodan, E.; Li, K.; Stockman, M. I., Plasmon Hybridization in Nanoparticle Dimers. *Nano Lett.* **2004**, *4*, 899.

(65)   Yeo, B.-S.; Stadler, J.; Schmid, T.; Zenobi, R.; Zhang, W., Tip-enhanced Raman Spectroscopy - Its status, challenges and future directions. *Chem. Phys. Lett.* **2009**, *472*, 1.

(66)   Cao, Y. C.; Jin, R.; Mirkin, C. A., Nanoparticles with Raman spectroscopic fingerprints for DNA and RNA detection. *Science (Washington, DC, U. S.)* **2002**, *297*, 1536.

(67)   Burda, C.; Chen, X.; Narayanan, R.; El-Sayed, M. A., Chemistry and Properties of Nanocrystals of Different Shapes. *Chem. Rev. (Washington, DC, U. S.)* **2005**, *105*, 1025.

(68)   Huang, X.; El-Sayed, I. H.; Qian, W.; El-Sayed, M. A., Cancer Cell Imaging and Photothermal Therapy in the Near-Infrared Region by Using Gold Nanorods. *J. Am. Chem. Soc.* **2006**, *128*, 2115.

(69)   Sudeep, P. K.; Joseph, S. T. S.; Thomas, K. G., Selective detection of cysteine and glutathione using gold nanorods. *J. Am. Chem. Soc.* **2005**, *127*, 6516.

(70)   Novotny, L.; Sánchez, J. E.; Sunney Xie, X., Near-field optical imaging using metal tips illuminated by higher-order Hermite–Gaussian beams. *Ultramicroscopy.* **1998**, *71*, 21.

(71)   Kazemi-Zanjani, N.; Vedraine, S.; Lagugné-Labarthet, F., Localized enhancement of electric field in tip-enhanced Raman spectroscopy using radially and linearly polarized light. *Opt. Express* **2013**, *21*, 25271.

(72)   Dorn, R.; Quabis, S.; Leuchs, G., Sharper Focus for a Radially Polarized Light Beam. *Phys. Rev. Lett.* **2003**, *91*, 233901/1.

(73)   Schadt, M.; Helfrich, W., Voltage-dependent optical activity of a twisted nematic liquid crystal. *Appl. Phys. Lett.* **1971**, *18*, 127.

(74)   Stalder, M.; Schadt, M., Linearly polarized light with axial symmetry generated by liquid-crystal polarization converters. *Opt Lett* **1996**, *21*, 1948.

(75)   Pashaee, F.; Hou, R.; Gobbo, P.; Workentin, M. S.; Lagugne-Labarthet, F., Tip-Enhanced Raman Spectroscopy of Self-Assembled Thiolated Monolayers on Flat Gold Nanoplates Using Gaussian-Transverse and Radially Polarized Excitations. *J. Phys. Chem. C* **2013**, *117*, 15639.

(76)   Pettinger, B.; Schambach, P.; Villagomez, C. J.; Scott, N., Tip-enhanced Raman spectroscopy: near-fields acting on a few molecules. *Annu. Rev. Phys. Chem.* **2012**, *63*, 379.

(77)   Yano, T.-A.; Inouye, Y.; Kawata, S., Nanoscale Uniaxial Pressure Effect of a Carbon Nanotube Bundle on Tip-Enhanced Near-Field Raman Spectra. *Nano Lett.* **2006**, *6*, 1269.

(78)   Sonntag, M. D.; Klingsporn, J. M.; Garibay, L. K.; Roberts, J. M.; Dieringer, J. A.; Seideman, T.; Scheidt, K. A.; Jensen, L.; Schatz, G. C.; Van Duyne, R. P., Single-Molecule Tip-Enhanced Raman Spectroscopy. *J. Phys. Chem. C* **2012**, *116*, 478.

(79)   Schmid, T.; Opilik, L.; Blum, C.; Zenobi, R., Nanoscale Chemical Imaging Using Tip-Enhanced Raman Spectroscopy: A Critical Review. *Angew. Chem., Int. Ed.* **2013**, *52*, 5940.

(80)   Cancado, L. G.; Hartschuh, A.; Novotny, L., Tip-enhanced Raman spectroscopy of carbon nanotubes. *J. Raman Spectrosc.* **2009**, *40*, 1420.

(81)   Budich, C.; Neugebauer, U.; Popp, J.; Deckert, V., Cell wall investigations utilizing tip-enhanced Raman scattering. *J. Microsc. (Oxford, U. K.)* **2008**, *229*, 533.

(82)   Hennemann, L. E.; Meixner, A. J.; Zhang, D., Surface- and tip-enhanced Raman spectroscopy of DNA. *Spectroscopy (Amsterdam, Neth.)* **2010**, *24*, 119.

(83)   Blum, C.; Schmid, T.; Opilik, L.; Weidmann, S.; Fagerer, S. R.; Zenobi, R., Understanding tip-enhanced Raman spectra of biological molecules: a combined Raman, SERS and TERS study. *J. Raman Spectrosc.* **2012**, *43*, 1895.

Chapter 3

3 Synthesis of Metal Substrates

3.1 Introduction

Metallic nanoparticles, such as gold (Au) and silver (Ag), have been intensely studied in the past decade due to their unique optical and electronic properties that can be finely tuned by altering their shapes and sizes. Their possible applications in fields such as catalysis, photovoltaics, biomedical diagnostics and imaging, and many other related fields, has fostered new synthetic approaches yielding a large variety of shape and sizes for these structures.[1-9] For example, nanomaterials exhibiting absorption bands in the near-infrared region have shown potential use in cancer hyperthermia, biological assays, cell imaging, as well for higher efficiency solar cells.[10-12] In order to tune the absorption band(s) in the desired spectral range, bottom-up and top-down fabrication methods can be used to tailor the optical and electronic properties of a variety of nanoscale materials. The opto-geometric parameters of nano-scale materials can therefore be optimized for a specific application.[13-16]

The synthesis, characterization and application of spherical metal nanoparticles have been actively explored over the past few decades.[17-19] Some examples of nanomaterials include nano-wires, prisms, cubes, plates, disks, and belts.[20,21] Interestingly by changing the shape of these materials, new optical and electronic enhanced properties have been observed. For example, nanotriangles appear to be more proficient catalysts than nanoparticles or nanowires for the oxidation of small organic molecules.[22] Nanotriangles or nanoplates are also interesting because of their intense plasmon resonance in the visible and the near-infrared regions which are sensitive to small geometric changes of the

substrate or its surrounding environment. Additionally, these nanotriangles show anisotropic electrical conductivity,[23] a localized enhancement of electric field at the vertices,[10] which makes them potential candidates for applications in photonics, optical sensing, imaging, and surface enhanced spectroscopies.[1,2]

Several synthetic methods have been reported to prepare gold and silver triangles and plates, including seed-mediated synthesis at room temperature,[9,24] polymer-assisted synthesis,[25] microwave heating,[26-28] and thermal aqueous solution approach,[29-31] yielding nanoscale structures with a variety of shapes and with a broad dispersion in size. The development of synthetic methods for the control of the shape and the size of nanomaterial with an excellent reproducibility and mono dispersity is currently a challenge. Since the physical properties of a given structure vary with its size and shape, it is therefore critical to have a very good control over the polydispersity of the desired material. This has been accomplished in very few instances using solution-chemistry routes based on adequate capping agents.[32]

For metallic nanoplates, the most widely proposed growth mechanism involves the confinement of metallic nanoparticles into a plate like morphology through surfactant capping (CTAB) or polymer adsorption (PVP) onto the (111) faces of the developing nanoplates.[26,33-35] The possible effects of reaction temperature, kinetics, and byproduct formation are also considered.[36,37] In this chapter, the synthesis of gold and silver nanoplates, ranging in dimensions from several tens of nanometers to a few microns will be discussed. In this thesis, the goal is to use such nanoplates as substrates for tip-enhanced Raman spectroscopy. These substrates have generally a low roughness preventing any intrinsic surface-mediated enhancement and can be used for gap-mode

TERS where the nanoscale object or molecule of interest is sandwiched at the interface between the metallic plate and the AFM tip. In this chapter, we are therefore investigating the chemical synthesis of gold and silver plates that was conducted in our group.

3.2 Synthesis of Gold and Silver Nanoplates

In the following paragraphs we report on the synthesis and the characterization of both gold and silver nanoplates triangles using wet chemistry synthesis. The goal is to produce nanoplates with dimensions and surface quality that are compatible with TERS experiments. Flat surfaces with small rms roughness and dimensions in the range of several micrometers are desired.

3.2.1 Chemicals, Materials, Mechanism of Synthesis

Gold Nanoplates: hydrogen tetrachloroaurate(III) trihydrate, cetyltrimethylammonium bromide (CTAB, $\geq$ 99%), aminopropyltrimethoxysilane (APTMS, 90%) and sodium citrate dehydrate (trisodium salt 99%) were purchased from Aldrich and used as received. **Silver Nanoplates:** silver nitrate, sodium borohydride, hydrogen peroxide (30 wt. %), ascorbic acid, acetonitrile and sodium citrate dehydrate (trisodium salt 99%) were purchased from Aldrich and used as received.

3.2.2 Synthesis of Gold Nanoplates

For the synthesis of hexagonal and triangular gold nanoplates with dimensions of a few micron, CTAB was used as a stabilizer. 12 mL of an aqueous solution containing 8.33×10^{-4} M(7 mg) tri-sodium citrate was heated to 50 °C and stirred in a flask over an oil bath. Separately, a solution of 1.25×10^{-3} M HAuCl$_4$ (4 mg) and 7.50×10^{-3} M CTAB

(22 mg) in 8 ml water was heated to 50 °C and once this solution reached to 50 °C, it was injected into hot tri-sodium citrate solution.

To prevent the loss of water, the solution was refluxed by connecting the flask to a condenser **(Figure 3.1).** Preheating of the two solutions before mixing decreased the reaction time and resulted in a better control of the size distribution of the nanoplates meanwhile CTAB gave a good control over the shape and the formation of the anisotropic Au structures.

After mixing the two solutions, a color change occurred after 5 min from yellow to colorless, indicating the formation of $AuBr^{2-}$ compound. After 30 minutes the solution temperature was slowly increased to 84 °C and kept at this temperature for 20 minutes to allow the reaction to fully complete and the solution became red brown, suggesting the formation of $AuBr^{4-}$ ions instead of $AuCl^{4-}$ ions. This is because Br^- ions are stronger complexation agents for Au (III) compared to Cl^- ions yielding the formation of $AuBr^{4-}$ ions. With the presence Br^- in CTAB, the Au complexes (CTA^+AuBr^{4-}) were formed rather than formation of Au colloids. Subsequently, the metastable state of $AuBr^{2-}$ was reduced to Au (0). The high reduction rate of Au (III) to Au (0) in solution, leads to the formation of Au nuclei.
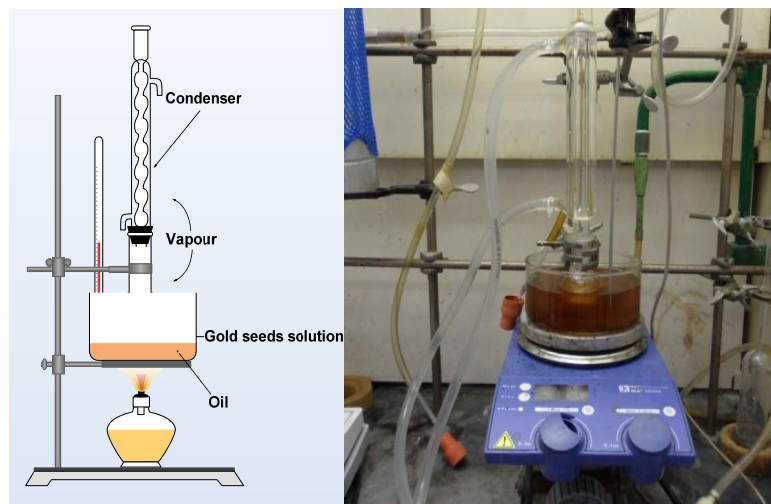
Figure 3.1 Schematic of the setup for synthesis of the nanoplate

As-prepared solution was cooled down to the room temperature over 3 hours. The golden color of the solution indicated the presence of large gold structures dispersed in the solution. According to the general growth mechanism in the literature, it was proposed that the small gold seed particles were formed initially upon introducing the surfactant (CTAB). Thereafter, the gold nanoparticles grouped together to form gold plates with specific morphologies including triangular and pentagonal nanoplates. This process directed the formation of further nanoplates as depicted in **Figure 3.2**.

$$HAuCl_4 + CTAB \longrightarrow [CTA^+AuBr^-] \longrightarrow AuBr_2^- \longrightarrow Au(0)$$

Au(III)   Au(I)   nuclei
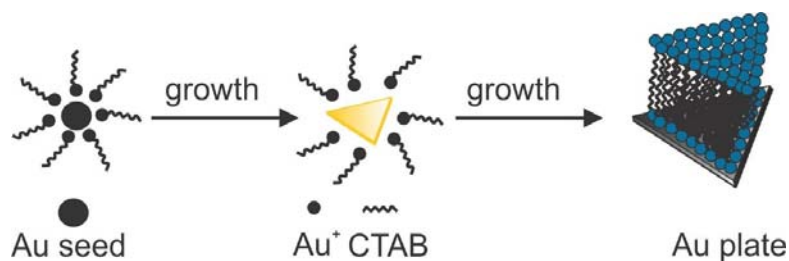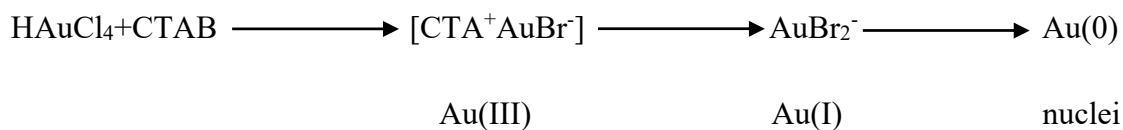
Figure 3.2 Scheme of the formation of triangular gold nanoplates

In the last step, the solution was transferred to a glass centrifuge tube that has been previously functionalized (amine inner-coated glass vials) and centrifuged at 4000 rpm for 10 minutes the solution was then removed and washed 5-6 times. The gold nanoplates after being cleaned were sonicated for few seconds and drop-casted onto clean glass cover slides.[31]

Numerous factors were taken into account, when finding the ideal reaction conditions including the reagent concentrations ([CTAB]/[HAuCl$_4$] ratio), the reaction temperature and time necessary to reinforce the nanoplate formation. For example, the discussed synthesis used a 6 to 1 molar ratio between CTAB: HAuCl$_4$. By changing this ratio the size and shape of the gold triangles can change. In this synthesis a [CTAB]/[HAuCl$_4$] ratio of 6 was used for the synthesis of gold nanoplates, the use of various reagent ratios may give lower yields of nanoplates.[38,39]

3.2.3   Preparation of Amine Inner-coated Glass Vials for Gold Nanoplates Solution

To prevent aggregation of gold nanoplates at the bottom of the centrifuge test tube, the test tubes were functionalized with amine groups to trap the gold nanoplates on the side-walls of the test tubes. In order to functionalize the inner surface of glass vial, a few drops of 3-Aminopropyl tri-methoxy silane (APTMS-less than 20 µL) were dropped in a glass Petri dish, and over the drop, a glass vial was placed upside down, with the aim to allow for the APTMS vapor to coat the internal side of the vial. The Petri dish with vials was placed into an oven at 130 °C for 2-3 hours to evaporate the silane compound and coat the surface of the vial with amine groups. The resultant vials was completely washed

with ethanol and water successively and used to contain as-prepared growth solution for the fractional precipitation.[40]

3.2.4   Characterization of Gold Nanoplates

Scanning electron microscopy was used to characterize one of the largest Au nanoplates synthesized, using the method described in section 3.2.2. A few typical images are shown in **Figure 3.3.**
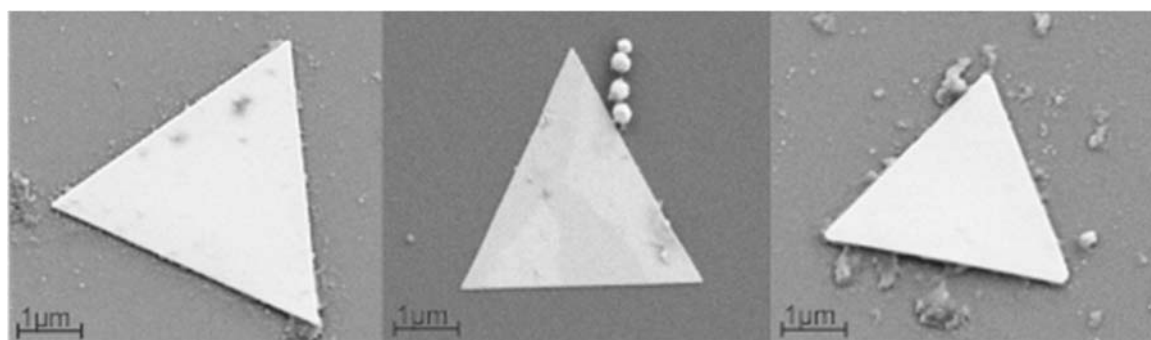
Figure 3.3 SEM images of the final nanoplates synthesized after 1h of reaction. Most of the nanoplates are several micrometers in width (typically 3 microns)

An AFM image of an isolated Au nanoplate is shown in **Figure 3.4.** Showing that the shape and the lateral sizes can vary for the different nanoplates but the thickness is quite homogeneous and is typically $\sim 20 \pm 3$ nm. The rms roughness as measured by AFM is typically around $\sim 0.5-1$ nm as compared to ~ 4 nm rms of a 20 nm thick film prepared by electron-beam evaporation. This is an important parameter to consider for TERS experiments where the nanoplates are used as substrates. Low roughness substrates prevent possible local enhancements of the electromagnetic field from the surface defects. Furthermore, a flat surface yields homogenous deposition of a structure of functionalization at its surface allowing reproducible TERS experiments.
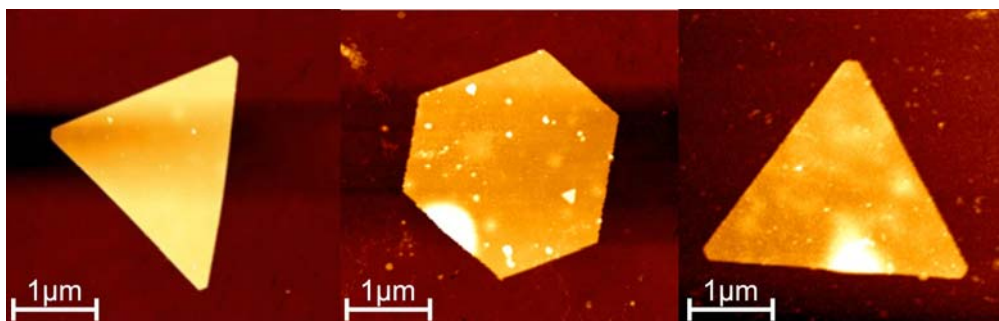
Figure 3.4 AFM images of gold nanoplate

Hexagonal nanoplates represent more than one-third of the total structures. In addition, as shown in **Figure 3.5**, few microplates with more unusual structures (like spherical gold nanoparticles and etc.) are also present which may be removed by centrifugation and washing process (hot water and organic solution). The majority of the nanoplates additionally display sharp edges and sizes that allow one to located and select them under an optical microscope.
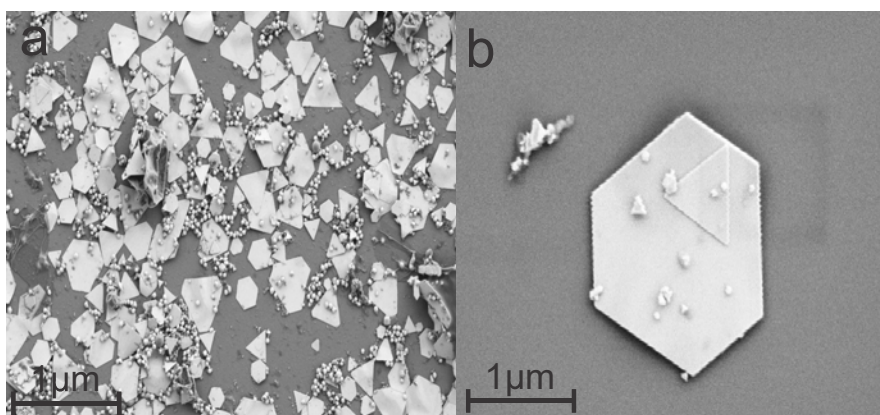
Figure 3.5 Gold nanoplates with hexagonal and truncated triangular shapes.

3.2.5   Synthesis of Silver Seed Solution

To a clean round bottomed flask sodium citrate (0.075 M, 12 mL), silver nitrate (0.1 M, 0.2 mL), and hydrogen peroxide (30 wt. %, 0.48 mL) were dissolved in 200 mL of

Millipore water and stirred for a minute. A fresh solution of sodium borohydride (0.1 M, 1.2 mL) was rapidly added to the silver solution and the seeds formed. The formation of the seed solution was determined based on the color change of the solution from yellow to orange to purple to blue. The solution was stirred for an additional 30 minutes, yielding a seed solution of AgNPs that had a diameter of ~2 nm. The solution was stored in the fridge at 5 °C until ready to use for the synthesis of silver triangles. When ready to use, the seed solution was centrifuged at 6000 rpm for 20 minute. The seed was collected and the volume was diluted to one fifth of the original volume. This proved to be problematic because the AgNPs did not fully separate at the centrifuged speed of 6000 rpm. To overcome this obstacle, the particles were later concentrated using an ultracentrifugation system that spun the sample at 38000 rpm, which completely separated the seed solution. For the following experiments the seed solution concentrated using 6000 rpm was used, unless clarified.

3.2.6   Synthesis of Silver Nanotriangles

A solution of ascorbic acid (0.1M, 0.15 mL), sodium citrate (0.075 M, 0.10 mL) and silver nitrate (0.1 M, 0.12 mL) was dispersed in acetonitrile (5 mL) and Millipore water (10 mL). This solution was cooled to 5 °C and the seed solution was added. The desired size of the nanotriangles can be altered by changing the volume of the seed solution. For example, for nanotriangles approximately 200 nm in length, 0.2 mL of the seed solution was added. As the volume of the seed solution increases, the size of the nanotriangle decreases. After the addition of the seed solution, the silver nanotriangles formed by stirring the solution for 30 minutes. The silver nanotriangles were clean by centrifugation. Here the precipitate was collected and transferred to a vial and a few

micro liters of diethyl amine was added to disperse the nanotriangles in solution. This solution was then stored in the fridge at 5 °C. **(Figure 3.6)**
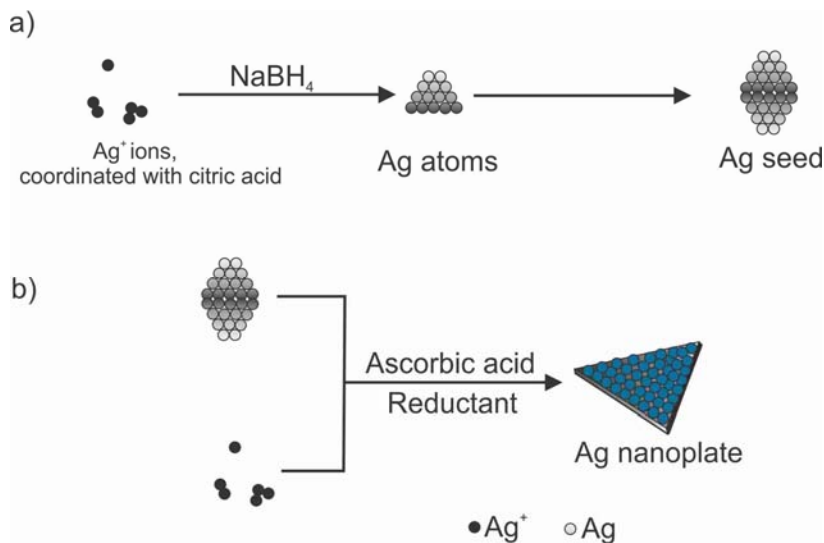
Figure 3.6 Scheme of the formation of triangular silver nanoplates (a) the formation of silver seeds and (b) the growth of silver seeds into triangular silver nanoplates.

3.2.7   Characterization of Silver Nanoplates

Four different sizes of the silver nanotriangles were synthesized. **Figure 3.7** shows that by changing the volume of the seed solution, the size of the silver triangles increases and the plasmon resonance changes accordingly yielding distinctive colors. From our observations the average size of the length of the triangles in solution A (12 mL of seed solution) is around 5 nm increasing to 700 nm for solution D, where the triangles are deformed into disks (0.04 mL of seed solution). The growth of the nanotriangles was monitored using UV-vis spectroscopy to monitor the absorption maxima of the solutions. A red shifted absorption and broadened spectrum was observed as the size of the triangle was increased **(Figure 3.8).** The absorption maximum for the seed solution was recorded

at 680 nm, was shifted to 719 nm while the triangles were formed (solution A), 903 nm

(solution B), 981 nm (solution C) and above 1000 nm for solution D
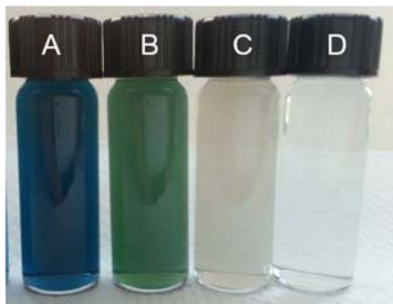
Figure 3.7 Pictures of colloidal solutions of silver nanotriangles with distinct sizes. The size was controlled by changing the initial volume of the seed solution added. The volume of seed solution is (A) 12 mL, (B) 2 mL, (C) 0.2 mL and (D) 0.04 mL
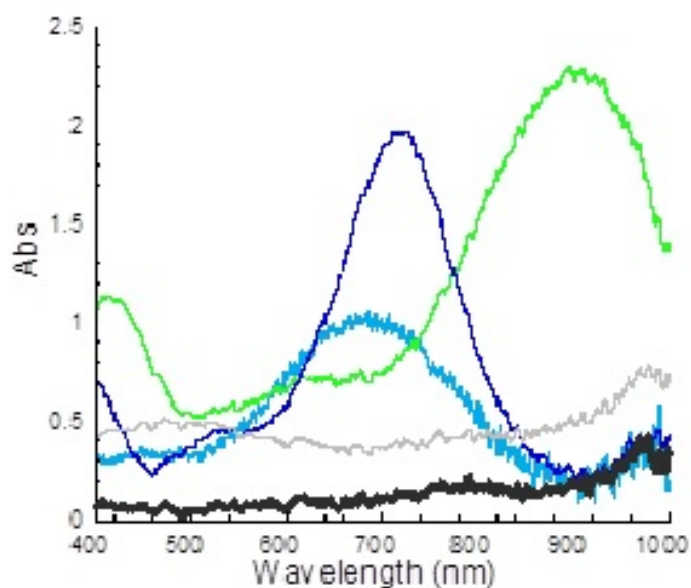
Figure 3.8 UV-vis absorption spectra of solutions changing the size of the nanotriangle. The seed solution (━), solution A (━), solution B (━), solution C (━), and solution D (━).

The silver nanotriangles prepared from 200 µL of the seed solution (solution C) were

characterized using SEM. Three different SEM samples were prepared for SEM

characterization. The first sample was obtained from a freshly prepared solution that was

directly drop casted onto a silicon wafer piece and characterized by SEM **(Figure 3.9 a, b)**. Equilateral triangles ranging in size from 160- 210 nm (edge length). The structure of these nanotriangles have very sharp vertices, yet significantly smaller than those reported in the literature for similar synthesis conditions (700 nm). One possibility may come from the starting diameter of the Ag seeds that have very small size.   The second sample was from a solution that was kept at fridge temperature (5°C) for a week before being deposited onto a silicon wafer and imaged **(Figure 3.9 c, d)**. For these structures, the resulting size is within the 200 nm range but the triangles appear to be more aggregated with smoother vertices. A third sample was examined. The sample was drop casted, dried and kept under ambient conditions during a week prior to SEM imaging **(Figure 3.9 e, f).** No clear triangles can be observed probably due to oxidation of the Ag crystals. Nevertheless, the triangles that are kept in the dark and stored in solution appear to be stable and yield the same images as for a freshly prepared sample.
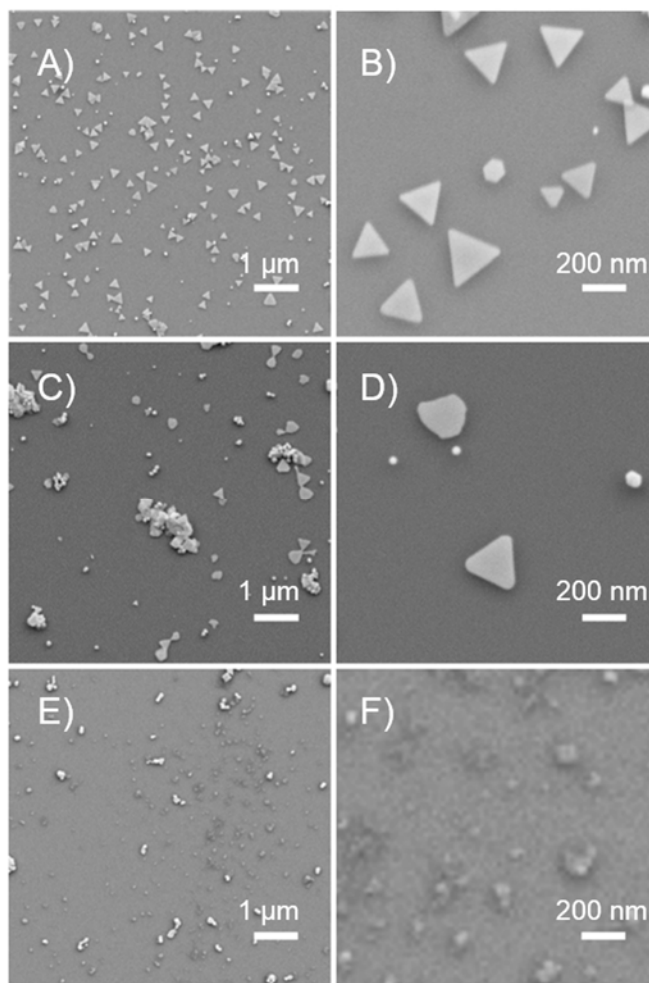
Figure 3.9 SEM images of a fresh prepared solution of nanotriangles (a & b), one week old solution (c & d) and a new solution that was dried and kept under ambient conditions for one week (e &f).

AFM was used to image the silver nanotriangles and evaluate their compatibility with possible TERS measurements. The AFM images showed a lot of aggregation occurring between different nanotriangles making it difficult to isolate individual nanotriangles as shown in **Figure 3.10**. Also, due to the size of the nanotriangles limited to 200-300 nm, it was impossible to observe the nanotriangles with our optical microscope equipped with a 100x objective. The AFM topography image shows numerous aggregates, making it challenging to find an isolated nanotriangle. When an isolated triangle was located, a higher resolution AFM image shows that this single entity

was composed of several silver nanotriangles forming an aggregate as shown on the
phase image of **Figure 3.10.** In conclusion, AgNTs were extremely hard to isolate using
drop casting method for these small silver nanotriangles. Unless an optimized method
can produce triangles with sizes of several micron range with a cleaner surface similarly
to gold nanoplates, the present silver nanotriangles are not suitable for TERS
measurements as substrates.
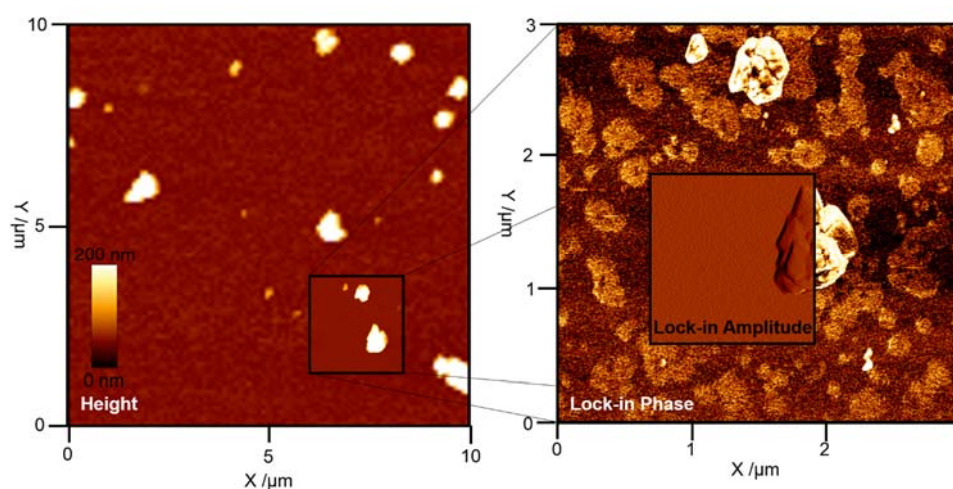
Figure 3.10 AFM image of silver nanotriangles.

An ultracentrifugation system enabling speed of 38000 round per min (rpm) was
ultimately used. After 90 min of centrifugation, the silver seeds were completely
separated and the solution was used to synthesis the silver nanotriangles. The resulting
triangles were drop casted onto a coverslip and imaged by AFM **(Figure 3.11).** The AFM
scans, illustrates the challenges in finding an isolated nanotriangle, and highlights the
concern of using these small silver nanotriangles in TERS. The zoomed view shows the
edge being 420 nm in length and the thickness of the triangle being 15 nm. Although we
were able to increase the size of the nanotriangle by a twofold factor, it was still to
challenging to use these nanotriangles for TERS due to their small sizes.
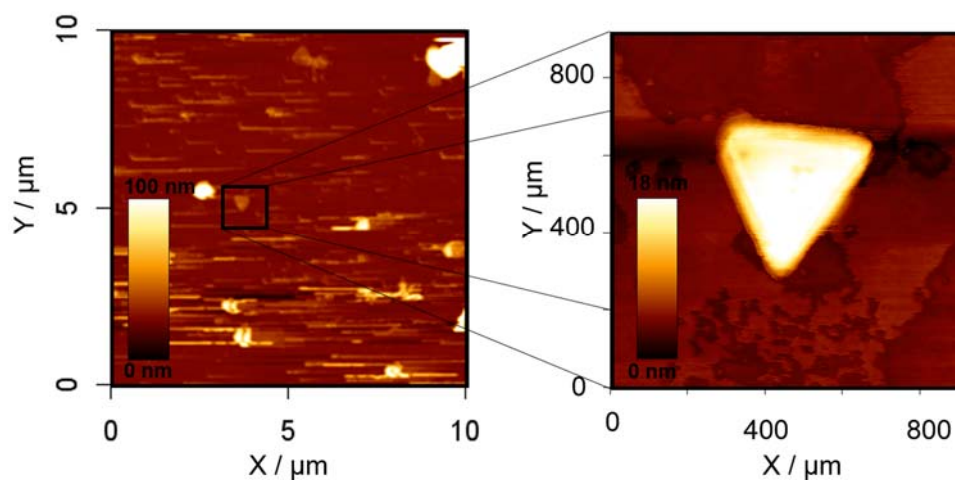
Figure 3.11 AFM image of silver nanotriangles.

3.3   Conclusion

In summary, gold and silver nanoplates were synthesized and characterized. The gold nanoplates proved to be stable over time and yielded a clean and smoother surface, ideally suited for TERS applications. The gold nanoplates were also easy to find under both optical and atomic force microscopes being a few microns in width. Though silver nanoplates are interesting material alternative as substrates in TERS experiments, they are too small in size and presence too many surface defects which prevent their use in the context of this thesis. Gold nanoplates will be used as a substrate of choice for most TERS studies reported in this manuscript.

3.4   References

(1)   Yonzon, C. R.; Stuart, D. A.; Zhang, X.; McFarland, A. D.; Haynes, C. L.; Van Duyne, R. P., Towards advanced chemical and biological nanosensors - An overview. *Talanta* **2005**, *67*, 438.

(2)   Pastoriza-Santos, I.; Liz-Marzan, L. M., Colloidal silver nanoplates. State of the art and future challenges. *J. Mater. Chem.* **2008**, *18*, 1724.

(3)   Zhang, J.; Li, X.; Sun, X.; Li, Y., Surface enhanced Raman scattering effects of silver colloids with different shapes. *J. Phys. Chem. B* **2005**, *109*, 12544.

(4)   Aslan, K.; Lakowicz, J. R.; Geddes, C. D., Rapid Deposition of Triangular Silver Nanoplates on Planar Surfaces: Application to Metal-Enhanced Fluorescence. *J. Phys. Chem. B* **2005**, *109*, 6247.

(5)   Astruc, D.; Lu, F.; Aranzaes, J. R., Nanoparticles as recyclable catalysts. The frontier between homogeneous and heterogeneous catalysis. *Angew. Chem., Int. Ed.* **2005**, *44*, 7852.

(6)   Jin, R.; Cao, Y.; Mirkin, C. A.; Kelly, K. L.; Schatz, G. C.; Zheng, J. G., Photoinduced conversion of silver nanospheres to nanoprisms. *Science* **2001**, *294*, 1901.

(7)   Seferos, D. S.; Giljohann, D. A.; Hill, H. D.; Prigodich, A. E.; Mirkin, C. A., Nano-Flares: Probes for Transfection and mRNA Detection in Living Cells. *J. Am. Chem. Soc.* **2007**, *129*, 15477.

(8)   Schmidt, J. P.; Cross, S. E.; Buratto, S. K., Surface-enhanced Raman scattering from ordered Ag nanocluster arrays. *J. Chem. Phys.* **2004**, *121*, 10657.

(9)   Kereselidze, Z.; Romero, V. H.; Peralta, X. G.; Santamaria, F., Gold Nanostar Synthesis with a Silver Seed Mediated Growth Method. *J. Vis. Exp.* **2012**, 3570.

(10)   Shankar, S. S.; Rai, A.; Ahmad, A.; Sastry, M., Controlling the Optical Properties of Lemongrass Extract Synthesized Gold Nanotriangles and Potential Application in Infrared-Absorbing Optical Coatings. *Chem. Mater.* **2005**, *17*, 566.

(11)   Xu, X.; Stevens, M.; Cortie, M. B., In Situ Precipitation of Gold Nanoparticles onto Glass for Potential Architectural Applications. *Chem. Mater.* **2004**, *16*, 2259.

(12)   Rashid, M. H.; Bhattacharjee, R. R.; Mandal, T. K., Organic Ligand-Mediated Synthesis of Shape-Tunable Gold Nanoparticles: An Application of Their Thin Film as Refractive Index Sensors. *J. Phys. Chem. C* **2007**, *111*, 9684.

(13)   Grzelczak, M.; Perez-Juste, J.; Mulvaney, P.; Liz-Marzan, L. M., Shape control in gold nanoparticle synthesis. *Chem. Soc. Rev.* **2008**, *37*, 1783.

(14)   Millstone, J. E.; Park, S.; Shuford, K. L.; Qin, L.; Schatz, G. C.; Mirkin, C. A., Observation of a Quadrupole Plasmon Mode for a Colloidal Solution of Gold Nanoprisms. *J. Am. Chem. Soc.* **2005**, *127*, 5312.

(15)   Kelly, K. L.; Coronado, E.; Zhao, L. L.; Schatz, G. C., The Optical Properties of Metal Nanoparticles: The Influence of Size, Shape, and Dielectric Environment. *J. Phys. Chem. B* **2003**, *107*, 668.

(16)   Liz-Marzán, L. M., Tailoring Surface Plasmons through the Morphology and Assembly of Metal Nanoparticles. *Langmuir* **2006**, *22*, 32.

(17)   Schmid, G., Large clusters and colloids. Metals in the embryonic state. *Chem. Rev.* **1992**, *92*, 1709.

(18)   Roucoux, A.; Schulz, J.; Patin, H., Reduced Transition Metal Colloids: A Novel Family of Reusable Catalysts. *Chem. Rev.* **2002**, *102*, 3757.

(19)   Daniel, M.-C.; Astruc, D., Gold Nanoparticles: Assembly, Supramolecular Chemistry, Quantum-Size-Related Properties, and Applications toward Biology, Catalysis, and Nanotechnology. *Chem. Rev.* **2004**, *104*, 293.

(20)   Braun, E.; Eichen, Y.; Sivan, U.; Ben-Yoseph, G., DNA-templated assembly and electrode attachment of a conducting silver wire. *Nature* **1998**, *391*, 775.

(21)   Sun, Y.; Xia, Y., Shape-Controlled Synthesis of Gold and Silver Nanoparticles. *Science* **2002**, *298*, 2176.

(22)   Goyal, R. N.; Aliumar, A.; Oyama, M., Comparison of spherical nanogold particles and nanogold plates for the oxidation of dopamine and ascorbic acid. *J. Electroanal. Chem.* **2009**, *631*, 58.

(23)   Singh, A.; Chaudhari, M.; Sastry, M., Construction of conductive multilayer films of biogenic triangular gold nanoparticles and their application in chemical vapour sensing. *Nanotechnology* **2006**, *17*, 2399.

(24)   Ward, C. J.; Tronndorf, R.; Eustes, A. S.; Auad, M. L.; Davis, E. W., Seed-Mediated Growth of Gold Nanorods: Limits of Length to Diameter Ratio Control. *J. Nanomater.* **2014**, *2014*, 7.

(25)   Parlow, J. J., Polymer-assisted solution-phase chemical library synthesis. *Curr. Opin. Drug Discovery Dev.* **2005**, *8*, 757.

(26)   Tsuji, M.; Hashimoto, M.; Nishizawa, Y.; Kubokawa, M.; Tsuji, T., Microwave-assisted synthesis of metallic nanostructures in solution. *Chem. - Eur. J.* **2005**, *11*, 440.

(27)   Wang, J.; Wang, Z., Rapid synthesis of hexagon-shaped gold nanoplates by microwave assistant method. *Mater. Lett.* **2007**, *61*, 4149.

(28)   Liang, W.; Harris, A. T., Facile size and shape control of templated Au nanoparticles under microwave irradiation. *Mater. Lett.* **2011**, *65*, 2307.

(29)   Chu, H.-C.; Kuo, C.-H.; Huang, M. H., Thermal Aqueous Solution Approach for the Synthesis of Triangular and Hexagonal Gold Nanoplates with Three Different Size Ranges. *J. Inorg. Chem.* **2006**, *45*, 808.

(30)   Lopez-Miranda, A.; Lopez-Valdivieso, A.; Viramontes-Gamboa, G., Silver nanoparticles synthesis in aqueous solutions using sulfite as reducing agent and sodium dodecyl sulfate as stabilizer. *J. Nanopart. Res.* **2012**, *14*, 1101.

(31)   Chu, H.-C.; Kuo, C.-H.; Huang, M. H., Thermal Aqueous Solution Approach for the Synthesis of Triangular and Hexagonal Gold Nanoplates with Three Different Size Ranges. *Inorg. Chem.* **2006**, *45*, 808.

(32)   Bouhelier, A.; Beversluis, M.; Novotny, L., Plasmon coupled tip-enhanced near-field optical microscopy. *J. Microsc.* **2003**, *210*, 220.

(33)   Wang, L.; Chen, X.; Zhan, J.; Chai, Y.; Yang, C.; Xu, L.; Zhuang, W.; Jing, B., Synthesis of Gold Nano- and Microplates in Hexagonal Liquid Crystals. *J. Phys. Chem. B* **2005**, *109*, 3189.

(34)   Chen, S.; Carroll, D. L., Silver Nanoplates: Size Control in Two Dimensions and Formation Mechanisms. *J. Phys. Chem. B* **2004**, *108*, 5500.

(35)   Kan, C.; Zhu, X.; Wang, G., Single-Crystalline Gold Microplates: Synthesis, Characterization, and Thermal Stability. *J. Phys. Chem. B* **2006**, *110*, 4651.

(36)   Millstone, J. E.; Metraux, G. S.; Mirkin, C. A., Controlling the edge length of gold nanoprisms via a seed-mediated approach. *Adv. Funct. Mater.* **2006**, *16*, 1209.

(37)   Xiong, Y.; Washio, I.; Chen, J.; Cai, H.; Li, Z.-Y.; Xia, Y., Poly(vinyl pyrrolidone): A dual functional reductant and stabilizer for the facile synthesis of noble metal nanoplates in aqueous solutions. *Langmuir* **2006**, *22*, 8563.

(38)   Huang, W.-L.; Chen, C.-H.; Huang, H., Investigation of the Growth Process of Gold Nanoplates Formed by Thermal Aqueous Solution Approach and the Synthesis of Ultra-Small Gold Nanoplates. *J. Phys. Chem. C.* **2007**, *111*, 2533.

(39)   Wang, C.; Kan, C.; Zhu, J.; Zeng, X.; Wang, X.; Li, H.; Shi, D., Synthesis of High-Yield Gold Nanoplates: Fast Growth Assistant with Binary Surfactants. *J. Nanomater.* **2010**, *2010*, 1.

(40)   Ha, T. H.; Kim, Y. J.; Park, S. H., Complete separation of triangular gold nanoplates through selective precipitation under CTAB micelles in aqueous solution. *Chem. Commun. (Cambridge, U. K.)* **2010**, *46*, 3164.

Chapter 4

4 Tip-enhanced Raman Spectroscopy of Self-assembled Thiolated Monolayers on Flat Gold Nanoplates using Gaussian-transverse and Radially Polarized Excitations

In this chapter, tip-enhanced Raman spectroscopy (TERS) is used to investigate self-assembled thiolated monolayers adsorbed onto surfaces with the goal to provide a better surface specificity in addition to a higher spatial resolution. We implement gap-mode TERS described in Chapter 2 and we used gold nanoplates functionalized with thiolated reference molecules such as alkoxy substituted azobenzene thiol and 4-nitrothiophenol. The monolayer is probed with a silver coated AFM tip in order to obtain the largest electromagnetic field enhancement from the surface plasmon localized between the silver tip and the functionalized gold surface. More specifically, the TERS spectra were collected from the self-assembled monolayer on gold using 532 nm excitation that is either linearly (Gaussian−transverse TEM00) or radially polarized. We also report on the nature of the collected TERS spectra for the thiolated molecules (azobenzene thiol and nitrothiophenol) that appear to be dependent on the polarization of the excitation light at the tip/substrate interface.

4.1　Introduction

TERS combines the vibrational imaging of a Raman microscope with the high spatial resolution of a scanning probe microscope. It has been used to study a variety of materials ranging from nanomaterials to biological samples [1-4] as well to induce photochemical reactions through a plasmon mediated effect.[5] The use of TERS in the biochemical and biophysical sciences is particularly attractive since, unlike other

techniques (e.g., fluorescence microscopy), it allows for sensitive analyses of very small areas of a selected sample with a high spatial resolution (better than 20 nm) in the absence of any endogenous or exogenous labels. As mentioned earlier, labelling can lead to undesired artifacts and misinformation, and sometimes requires the synthesis of endogenous fluorophores, which could perturb the native organization of the bio-system of interest.[6] Over the past decade, a number of seminal manuscripts and review papers on this topic have brought TERS to maturity for high resolution Raman imaging as well as single molecule detection when used in resonant conditions.[7-11] TERS is an extension of surface enhanced Raman spectroscopy (SERS) that makes use of rough metal (Au, Ag, Pt, Cu) substrates to enhance the Raman signature of molecules located in its vicinity through electromagnetic field local enhancement. The literature in SERS is very abundant 40 years after its discovery. Substrates such as films, electrodes, colloids, organized surfaces have demonstrated large local enhancements thus increasing the detection limit of Raman measurements. The principle of TERS is to use a single metal particle or a small aggregate of metal particle and bring it in proximity to a sample using a precise nano positioning system. The local electromagnetic enhancement serves as an antenna to local amplify both the excitation and the Raman signals. Local enhancements enabled by TERS has enabled high sensitivity of detection down to the single molecule level together with high spatial resolution limited by the tip apex dimension.[12] The collection of such locally-enhanced electromagnetic field contains the optical or spectroscopic information from the high spatial frequencies of the object (small details), and spatial resolution of spectroscopy measurements down to 12 nm has been demonstrated on ideal scatters such as carbon nanotubes.[13,14] Beyond the drastic improvement of the spatial

resolution, TERS can also be employed to probe monolayers deposited or functionalized onto flat surfaces such as self-assembled monolayers (SAMs). This detection would be very difficult using standard non-resonant Raman scattering or mid-infrared, absorption, and only surface-specific techniques such as sum-frequency generation or polarization-modulation spectroscopy could be used.[15,16] Surface enhanced Raman spectroscopy (SERS) and surface enhanced infrared absorption spectroscopy (SEIRA) are also approaches of choice for detecting monolayers using nanostructured metallic surfaces prepared by a variety of methods including metal sputtering or advanced nanofabrication methods, but they do not provide a better spatial resolution and the molecular orientation over the surface has a large distribution due to the roughness of the SERS platform or SEIRA substrate.[17-20]

Here we are investigating SAMS functionalized onto gold surface as model molecular systems using TERS with two distinct polarizations of the excitation light. More specifically, for the first time we compare, for the same functionalized object, a side-by-side series of experiments using a tightly focused linearly polarized TEM00 beam and a radially polarized beam at the selected wavelength of 532 nm.

The field enhancement strongly depends on the polarization properties of the exciting radiation with respect to the symmetry of the tip that it illuminates.[4] Ideally, a polarization component of the impinging field along the tip axis leads to larger enhancements. In reflection geometry with a large angle of incidence, it is trivial to orient the polarization of the impinging laser in the plane of incidence thus with a large polarization component along the tip axis. In transmission geometry, a longitudinal component along the tip axis can also be observed when using a tightly focused linearly

polarized beam. At the focal point, most of the intensity of the total electric field will originate from the same component of the initial transverse polarization but there will be also a weaker longitudinal field with two lobes oriented along the tip axis. In such a condition, the TERS signal arises from these two lobes that are amplified by the presence of the metallic tip. A way to decrease the transverse component and to amplify the longitudinal component is to use a radially polarized mode.[21-23] Using this approach, the cylindrical symmetry of the laser polarization is such that, when tightly focused with a high *N.A.* microscope objective, the radial components (Ex, Ey) of the electric field components overlap in phase at the focal point giving rise to a significantly larger longitudinal (Ez) component. When interacting with the metallic AFM tip, a larger amplification of the resulting electromagnetic field and a confinement at the tip extremity are observed providing the best condition for tip-enhanced spectroscopy measurements.[13,24]

We report here on the change of relative Raman intensities and the near-field nature of the TERS measurements using a transmission geometry setup using both radial and linearly polarized (TEM$_{00}$) modes. The samples investigated here are SAMs on flat gold nanoplates. More specifically we have investigated SAMS made of 4-nitrothiophenol and on 2-[4-(4-decyloxylphenylazo) - phenyl] ethyl thiol molecules adsorbed on these ultraflat nanoplates.[25,26]The choice of gold thin and flat nanoplates was driven by several factors, such as (i) the transmission geometry of the setup that requires a small thickness of gold in order to optimize the laser intensity going through the gold substrate, (ii) a flat surface of gold that can be functionalized with thiolated molecules with minimum surface enhancement effects from the nanoplate itself, and (iii) the interest to benefit from the

TERS "gap mode", where the monolayer is isolated between two metallic interfaces, i.e. the gold substrate and the metallic tip.[27] Such an approach elegantly proposed by Deckert's group shows ideal conditions when the metallized TERS tip is in interaction with another ultraflat metallic surface.[28-31] However in his work, the excitation mode is linearly polarized (TEM$_{00}$) and we demonstrate here the interest of using a radially polarized mode in conjunction with gap-mode TERS.

4.2   Material and Methods

4.2.1   Chemicals

Hydrogen tetrachloroaurate(III) trihydrate (Aldrich), cetyltrimethylammonium bromide (CTAB, $\geq$ 99%, Aldrich), sodium citrate dehydrate (tri-sodium salt 99%), and aminopropyltrimethoxysilane (APTMS, 90%) were purchased from Aldrich and used as received. 2-[4-(4-Decyloxylphenylazo)phenyl]ethyl thiol (w 398 g·mol^{-1}) was synthesized following the procedure proposed by Marquestaut et al.[18] 4-Nitrothiophenol (MW 155.17 g·mol^{-1}) was purchased from Aldrich. Ultrapure deionized water (18.3 MΩ cm^{-1}) was used for all solution preparations.

4.2.2   Self-Assembled Monolayer (SAM) Preparation

SAMs were prepared by immersion of the coverslip coated with the gold nanoplate into a 10^{-3} M solution of thiolated molecules (azobenzene thiol, 4-nitrothiophenol) in chloroform for 24 h. The functionalized nanoplates located onto the glass coverslips were washed several times with chloroform and distilled water prior drying with nitrogen.[18]

4.2.3   TERS Setup

The TERS setup is described in Chapter 2. We just highlight here deviations from

Chapter 2. Experiments were performed in transmission mode as depicted in **Figure 4.1**.

In this geometry, light is focused from below via the sample substrate onto the tip and the

sample. The tip is in feedback with the sample and interacts at the focal point with the

evanescent waves confined at the surface of the sample. Here, thin glass coverslips (120

μm thickness) were used to hold the thin gold functionalized nanoplates. The linearly

polarized light with an excitation wavelength of 532 nm (Compass 315 M laser,

Coherent) was focused with a high numerical aperture objective (PlanAPO Olympus,

N.A. = 0.95, 100X) onto the metalized AFM tip. The laser intensity at the sample and

after the 20 nm gold nanoplate was set to 300 μW. Under these conditions, no local

heating or deformation of the nanoplates was observed. No drift of the AFM topography

conducted in the presence of irradiation was observed either. The TERS probe was

attached to its own (x,y,z) piezoelectric stage and was kept a few nanometers above the

sample surface by means of a conventional AFM feedback mechanism. AFM scans are

carried out in noncontact mode, and the AFM tips (NSG 10, NT-MDT Inc., silicon tips

with a typical oscillating frequency of f = 240 kHz and a maximum force constant of k =

37.6 N/m) were coated with 20 nm of silver by means of electron-beam induced thermal

evaporation of the metal and were used within a day of the deposition or kept for a

maximum of 24 h in a desiccator purged with Argon. The typical curvature of these

commercial tips ranges from 6 to 10 nm for non-coated tips. Upon coating with the silver

thin film the measured radius is 25 nm as estimated by scanning electron microscopy

(SEM, **Figure 4.1b**, inset). The cone angle at the apex is 7°−10° as specified by the

manufacturer.
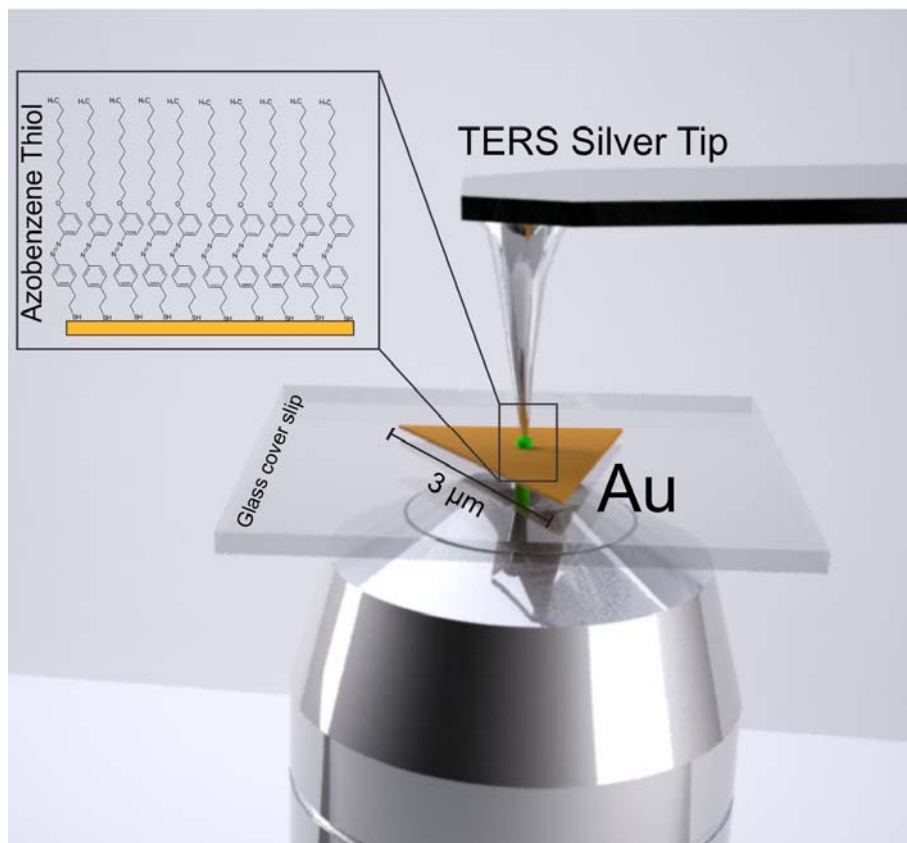
Figure 4.1 TERS setup in back reflection geometry.

The laser mode either was coming directly from the linearly polarized laser

excitation or was modified with a liquid crystal modulator with phase compensation

(ARCoptix) to generate a radially polarized mode (**Figure 4.2b**). In such a case the beam

was preliminarily expanded to a 10 mm diameter before entering the LC cell. A shear

plate was used to check that the beam was parallel before entering the cell. After coming

through the LC cell, the beam was further filtered with a spatial filter and made parallel

with a 10X microscope objective. The diameter of the beam was further reduced to a 4

mm diameter with a set of convex (f = +100 mm) and concave lenses (f = −25 mm). The

size of the beam was finally slightly adjusted so that it filled the entrance pupil of the high numerical aperture objective.
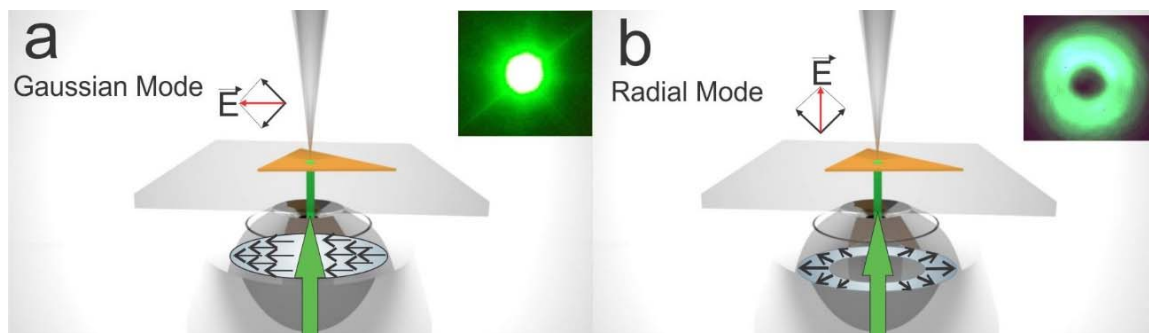
Figure 4.2 (a) Gaussian linearly polarized excitation source (b) Radial excitation source.

4.3   Results and Discussion

It is critical in TERS to perfectly align the tightly focused laser beam at the extremity of the tip. To this end, several methods can be used when using a tip mounted on its own (x, y, z) scanner which is the case for the AFM instrument used in this study. To locate the tip end, vertical deflection of the AFM can be used. For this the tip in feedback with the sample or a few nanometers above the sample must scan the region located in the focal plane. The laser intensity can be raised so that the tip vertical deflection can be monitored as shown in **Figure 4.3a** leading to the rough localization of the tip extremity. A second alternative involves the detection of the scattering of the tip extremity using a photodiode located in the path of the microscope. Here again, the tip must scan above the sample in the (xy) plane and generate typical scattering maps as shown in **Figure 4.3b**. The tip location can be here unambiguously identified. A third method involves the Raman mapping of the metal-coated silicon tip. Even though the tip is coated with only 20 nm of silver, the scattering cross section of the silicon is so large

that the intensity of the silicon peak at 520.7 cm^{-1} (first order optical phonon of bulk silicon) of the cantilever and the tip can be detected through a Raman map of the scanning probe. Here again the tip is raster scanned in the (xy) focal plane using its own piezo electric actuator. The Raman maps shown in **Figure 4.3c,** d show the variation of silicon peak intensity without or with background correction, respectively. The maximum intensity of the silicon peak maximizes the chances to locate the tip. These three methods can be further optimized by selecting smaller scanning regions around the tip position. For most experiments, we first use vertical deflection in fake feedback mode (tip away from the sample but yet scanning) to roughly determine the tip position. Scattering is then used with the tip in feedback with the sample to more precisely locate the tip, and finally the Raman signal of silicon is used to more precisely locate the tip by maximizing the Raman intensity. This ensemble of methods used to locate the tip depends on the substrate as well as the composition and the geometry of the tip. Once the tip location is found and positioned accurately at the focal point, the x,y position of the tip piezo scanner is frozen, and the sample scanner will move the sample in the lateral directions x and y while the z tip scanner maintains the feedback between the tip and the sample surface. In our experiments, flat gold nanoplates with a thickness of 20 nm were first identified on the glass coverslips.
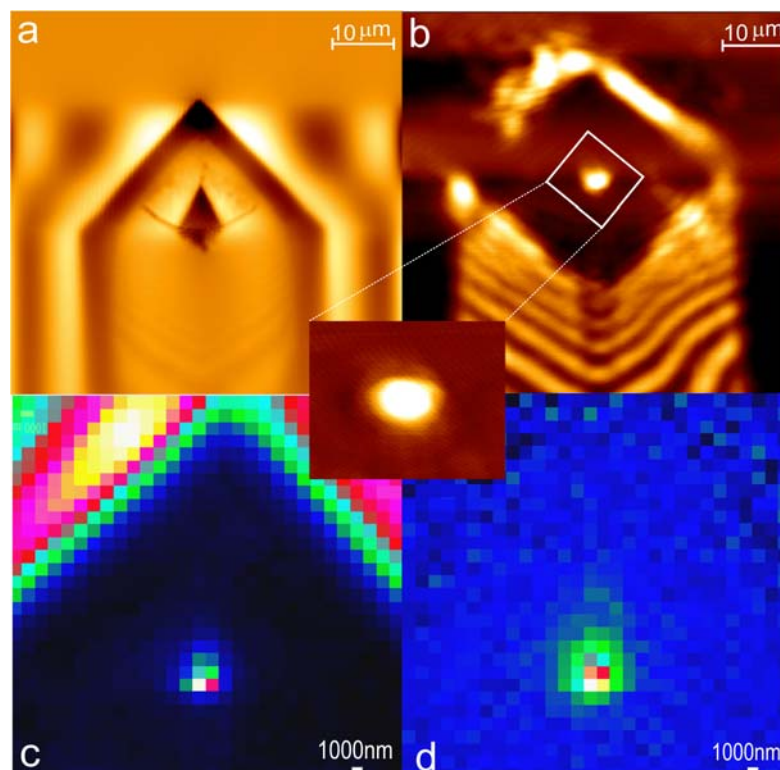
Figure 4.3 (a) Vertical deflection from the tip b) scattered laser light from the tip apex c) Raman intensity map without background correction d) Raman intensity map with background correction

A typical SEM image of a pristine gold substrate prior to functionalization with thiolated SAM is shown in **Figure 4.4a** An AFM image of an isolated Au nanoplate is shown in **Figure 4.4b**. The shape and the lateral sizes can different for nanoplates but the thickness is quite homogeneous and is typically $\sim 20 \pm 3$ nm as shown in the inset of **Figure 4.4b**. The rms roughness as measured by AFM is typically around $\sim 0.5-1$ nm as compared to ~ 4 nm rms of a 20 nm thick film prepared by electron beam evaporation. Higher features corresponding to smaller gold particles with a variety of different shapes (spherical, cubic, hexagonal) can be observed on the gold nanoplates and can be removed to some extent by subsequent washing. The height of these particles shown in **Figure 4.4b** is typically 20 nm. For the Raman measurements conducted on the SAMS, these

particles do not necessarily interfere with the measurements as long as the TERS tip can be located precisely away from these particles. This avoids any possible SERS effect from the individual particle.
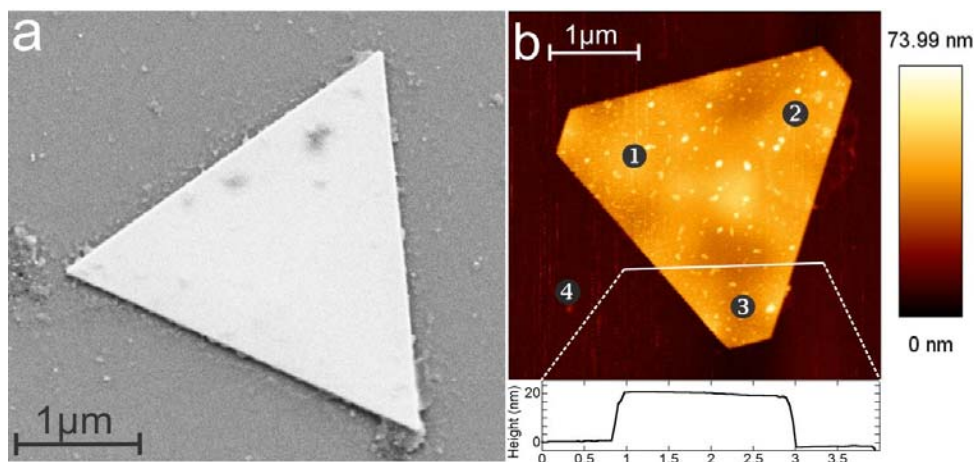
Figure 4.4 (a) SEM image of gold nanoplate (b) AFM image (with cross sections) of the Au (111). TERS spectra were acquired on selected points ❶, ❷, ❸ and ❹.

4.3.1   TERS Study of Azobenzene Thiol.

The TERS spectra of the azobenzenethiol monolayer were recorded at four different positions as indicated in **Figure 4.4b** and are presented in **Figure 4.5 a, b** for radial and transverse input polarizations, respectively. In both measurements, the intensity of the laser was similar and set to 9 mW at the entrance of the objective. This value is relatively high for a microscope measurement, but a large portion of the light is back reflected at the glass coverslip/gold interface or absorbed by the 20 nm thick gold plate. Only 300 µW effectively reaches the sample/ tip junction requesting that the acquisition time range from 10 to 45 s. Spectra reported in **Figure 4.5a** at three different locations on the metallic nanoplate (noted 1, 2, 3 in **Figures 4.4b and 4.5a**) were acquired with a 45 s acquisition and show significant enhancement of the signal due to

the proximity of the silver tip. When the tip is brought 20 nm away from the gold surface

(noted 1 (20 nm) in **Figure 4.5 a** the signal vanishes quickly while no Raman signal can

be seen from the glass coverslip eliminating any possible contamination of the AFM tip

or the presence of aggregates on the glass surface (point 4).
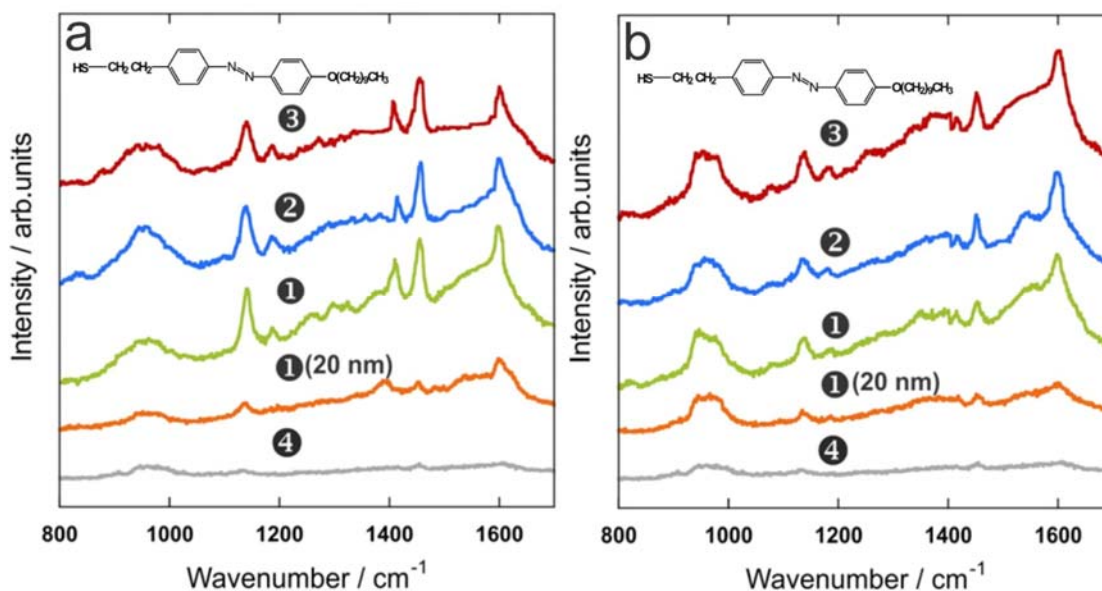
Figure 4.5 (a) Tip-enhanced Raman spectra measured with a radial polarization of an azobenzene monolayer functionalized onto a gold nanoplate (λ=532 nm, acquisition time=45 s). The TERS spectra were measured at points ❶, ❷, ❸ and ❹. Spectra was also measured with the AFM tip located 20 nm away from the surface (point ❶ (20nm)). (b) Tip-enhanced Raman spectra measured with a linear polarization of an azobenzene monolayer functionalized onto a gold nanoplate (λ=532 nm, acquisition time=45 s). The TERS spectra were measured at points ❶, ❷, ❸ and ❹. Spectrum was also measured with the AFM tip located 20 nm away from the surface (point ❶ (20 nm)).

Further intensity versus distance measurements are later discussed for the measurements

conducted on the gold nanoplate. The Raman band measured at 1141 cm^{-1} is related to

the in-phase stretching of the ν_{phenyl}−N bond, while the CH in plane bending mode

reported at 1188 cm^{-1} likely overlaps in our spectra with the 1141 cm^{-1} mode (weak right

shoulder). The modes at 1409 and 1457 cm^{-1} are mainly in-plane ring bending modes

with coupling to the N=N stretch. The C=C stretching of the phenyl rings is located at 1600 cm^{-1}. In **Figure 4.5b**, similar measurements were done with a transverse Gaussian mode. Similar laser intensities and acquisition times were used, and the spectra obtained at three distinct points (noted 1−3) are clearly weaker than in the case of a radially polarized mode. The large peak at ~1000 cm^{-1} is coming from the glass coverslip and is comparable for both radial and transverse modes. The Raman modes of the azobenzene thiol can be seen, but the relative intensities are altered. For example the shape and the relative intensity of the phenyl ring mode at 1600 cm^{-1} is different for the two input polarizations. Similarly the two peaks at 1409 and 1457 cm^{-1} are clearly identified in **Figure 4.5b** with a radial mode while only one peak at 1457 cm^{-1} appears when a transverse Gaussian mode is used. Furthermore, the difference between the far (20 nm above the surface) and near-field measurements is less marked in the case of a Gaussian mode as compared to the radial mode. The signal is increased by a factor 2−3 when Gaussian mode is used, while a 6−8 factor can be reached when using the radial mode. From these results we can conclude that (i) the radial mode appears to be more effective for TERS measurements leading to a higher enhancement, (ii) the relative intensities of the Raman modes can be affected by the input polarization of the laser source, and, last, (iii) the TERS nature of the signal is evidenced by a significant decrease of the signal when the tip is 20 nm away from the surface.

4.3.2   TERS Study of 4-Nitrothiophenol (4-NTP)

4-NTP is a model molecule that can be efficiently used for TERS measurements on the gold nanoplate. An AFM image of the isolated Au nanoplate was first acquired, and four points were selected to perform TERS measurements as indicated in **Figure 4.6a**.
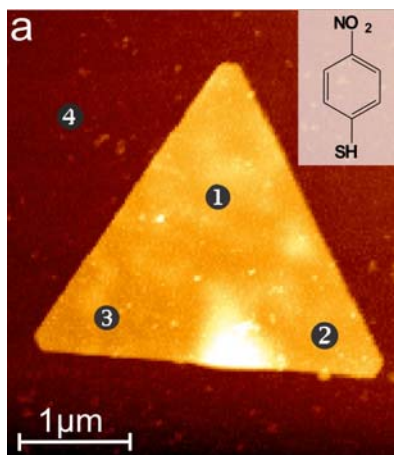
Figure 4.6 **(a) AFM map of gold nanoplate functionalized with 4-nitrothiophenol structure.**

The TERS spectra shown in **Figure 4.7 a,b** were collected using a radial mode and a transverse mode, respectively, and measured at three different locations over the gold nanoplate (points 1, 2, 3) with a 45 s acquisition time. In both cases, the spectra are significantly more intense when compared to measurements when the tip is retracted by 20 nm demonstrating clearly the interest of TERS for vibrational measurements at the monolayer level. Similarly to the study of the azobenzene SAM, no TERS signal can be detected when the tip is located outside the gold nanoplate eliminating any possible contamination of the AFM tip (point 4). For 4-NTP the bands at 1140 and 1188 cm^{-1} can be attributed to the C−H stretching bending and C−H in-plane bending while the bands at 1335 and 1440 cm^{-1} are assigned to the NO$_2$ stretching vibrations.
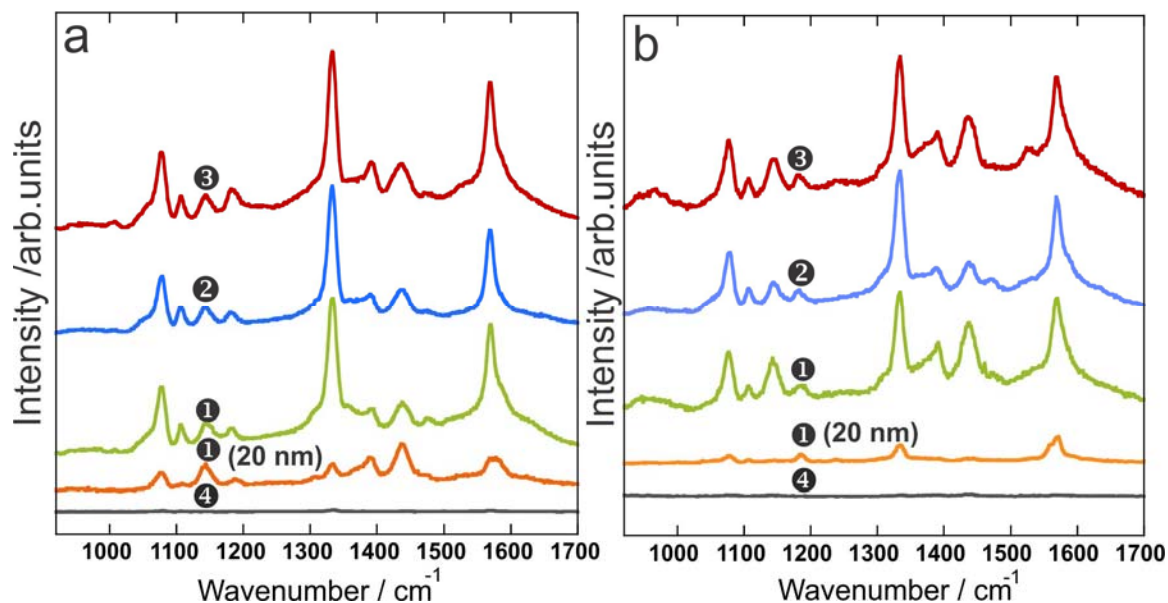
Figure 4.7 **(a) Tip-enhanced Raman spectra measured with a radial polarization of a 4-NTP monolayer functionalized onto a gold nanoplate (λ=532 nm, acquisition time=45 s). The TERS spectra were measured at points ❶, ❷, ❸ and ❹. Spectrum was also measured with the AFM tip located 20 nm away from the surface (point ❶ (20nm)). (b) Tip-enhanced Raman spectra measured with a linear polarization of a 4-NTP monolayer functionalized onto a gold nanoplate (λ=532 nm, acquisition time=45 (s). The TERS spectra were measured at points ❶, ❷, ❸ and ❹. Spectrum was also measured with the AFM tip located 20 nm away from the surface (point ❶ (20 nm)).**

It is noteworthy that the relative intensities of the Raman bands are here again dependent on the input polarization. More specifically, when using the transverse mode, the relative intensity of the Raman peak at 1140 cm^{-1} appears to increase when compared to peaks at 1188 and 1107 cm^{-1} while the peak at 1335 cm^{-1} is less intense compared to when the radial mode is used. Such changes in intensities have been observed in several studies and are related to the photo reduction of the 4-NTP into a 4,4′-dimercaptoazobisbenzene molecule anchored at both ends to the gold surface.[32] Such spectral changes do not seem to be observed when the radial mode is used. This observation indicates that the efficiency of the photo reduction of 4-NTP is therefore dependent on the input polarization. When considering that, on similar types of molecules

such as benzene thiol, the average molecular orientation of the benzene group is tilted

with a 30° angle with respect to the (111) gold surface,[33] there is a correlation between

the orientation of the nitro group undergoing photo reduction and the irradiation laser

source polarization. In other terms, the photo induced reduction of the NTP monolayer

appears to be less efficient when a larger longitudinal field is used, although the

orientation of the NO_2 stretching mode has also a larger component along the normal

direction with respect to the gold (111) surface. This observation implies that either the

average orientation could be larger than 30° in particular if multiple layers are formed

over the gold surface. A long functionalization time (24 h) and a high concentration of

the NTP in chloroform (1 mM) are critical factors that may be responsible for a large

orientation distribution of molecules on the gold surface.

Last, in order to ascertain the near-field nature of the enhancement, the Raman

intensities of several bands were measured as a function of the axial z position of the tip

with respect to the sample plane. At z = 0 the tip is in feedback with the sample, while, at

increasing z positions, the tip is brought away from the functionalized surface. Such

experiments were conducted for both thiolated azobenzene and 4-nitrothiophenol as

probed by radial and linearly polarized excitations and are reported in **Figure 4.8** for the

most intense modes in both compounds. The tip−sample separation distance was set to z

= 0, 5, 7, 10, 20, 50, 100, 500, 1000 nm using the piezo electric actuator of the tip. At 500

nm of separation, no signal can be observed for most modes. The variation of intensities

between 0 and 500 nm were fitted with a $1/r^{5\pm1}$ law, with r being the separation distance

between the tip and the surface of the sample, as shown in the inset of **Figure 4.8 c, d** for

4-NTP (mode at 1335 cm^{-1}) with radial and transverse Gaussian modes, respectively.

Similar behavior was observed for both Gaussian and radial modes confirming the very fast decay of the near field enhancement due to the presence of the tip. Within the first 10 nm the signal of the maximum Raman intensity decreases by 90−95% thus confirming the near-field nature of the TERS experiments when using transverse and radial modes.
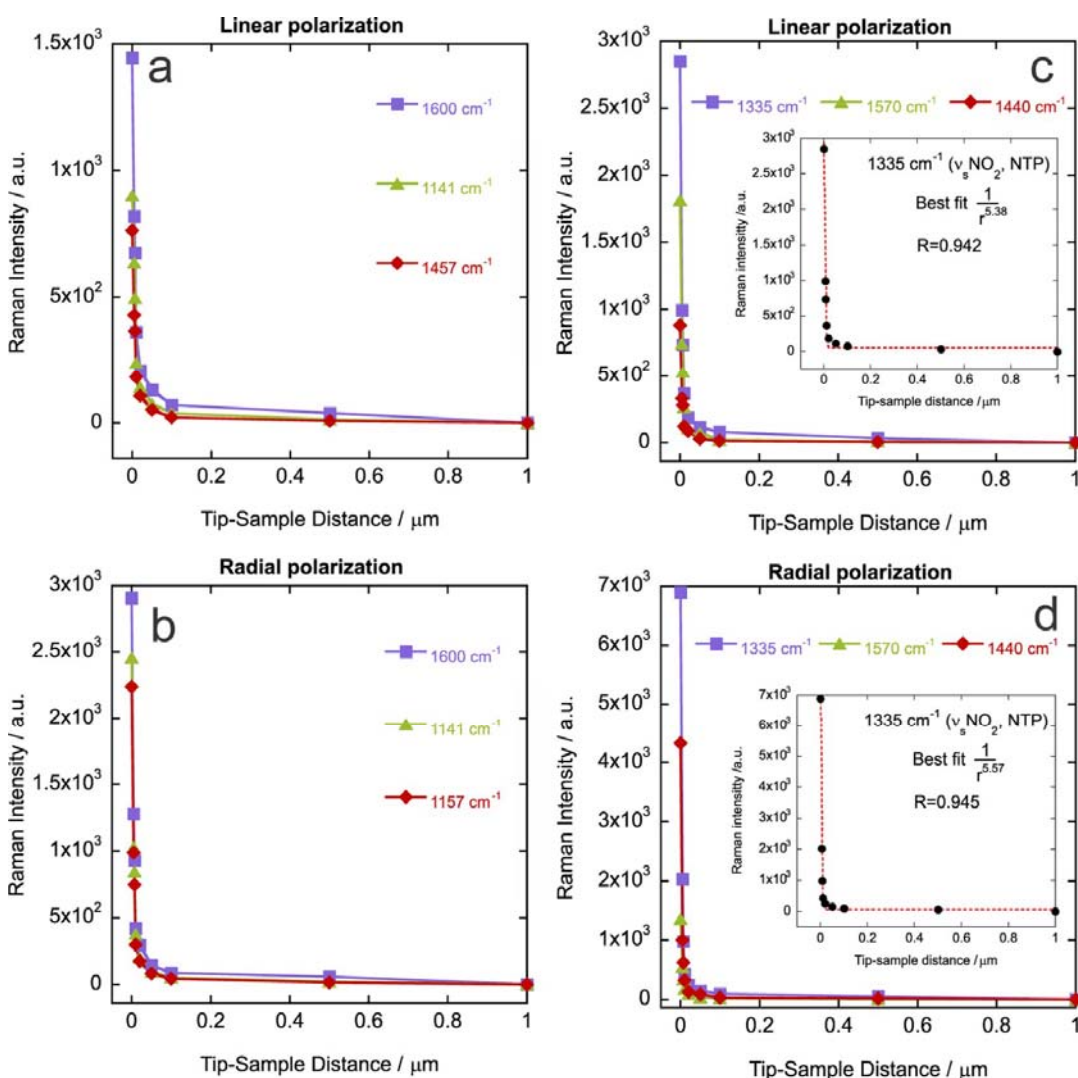
Figure 4.8 Raman intensity versus tip-sample distance using linearly polarized light and radially polarized light conditions for gold nanoplate functionalized with azobenzene thiol (a,b) and 4-nithiophenol (c,d). The inset of c and d show the fitting curve used for the $\nu_s NO_2$ mode at 1335 cm^{-1}.

4.4   Conclusion

In summary, self-assembled monolayers were investigated by tip-enhanced Raman spectroscopy using linearly or radially polarized excitations for the input excitation. Thin (20 nm) and ultraflat gold (111) nanoplates were functionalized with thiolated azobenzene and 4-NTP. The TERS nature of the collected signal from the functionalized monolayer was demonstrated by changing the tip−sample distance revealing the fast decay of the near-field when the tip is brought out of contact. More importantly, for similar laser irradiance, the use of the radial mode with a strong longitudinal electric field component seems to yield more intense TERS spectra as well as to minimize possible photochemical processes occurring at the surface of gold. This is shown specifically in the case of 4- NTP where reduction of the nitro group seems to be inhibited as compared to irradiation with the transverse mode. Last, it is noteworthy that we have deliberately measured TERS on selected points over the gold nanoplates with minimum roughness in order to avoid altering the polarization of the excitation source. Specifically, we avoided the sharp edges of the gold nanoplates as well as the gold nanoparticles located over the nanoplate. Nevertheless, these features could be utilized to provide additional enhancement effects through SERS and the localized surface plasmon located at the apexes and edges of the nanoplates. High-resolution TERS mapping could be of interested to provide the distribution of the electromagnetic field enhancement over a single nanoplate.

4.5   References

(1)   Hermann, P.; Hecker, M.; Chumakov, D.; Weisheit, M.; Rinderknecht, J.; Shelaev, A.; Dorochkin, P.; Eng, L. M., Imaging and strain analysis of nano-scale SiGe structures by tip-enhanced Raman spectroscopy. *Ultramicroscopy* **2011**, *111*, 1630.

(2)   Pozzi, E. A.; Sonntag, M. D.; Jiang, N.; Klingsporn, J. M.; Hersam, M. C.; Van Duyne, R. P., Tip-Enhanced Raman Imaging: An Emergent Tool for Probing Biology at the Nanoscale. *ACS Nano* **2013**, *7*, 885.

(3)   Kawata, S., Plasmonics for Nanoimaging and Nanospectroscopy. *Appl. Spectrosc,* **2013**, *67*, 117.

(4)   Hartschuh, A.; Qian, H.; Meixner, A. J.; Anderson, N.; Novotny, L., Tip-enhanced optical spectroscopy for surface analysis in biosciences. *Surf. Interface Anal.* **2006**, *38*, 1472.

(5)   van Schrojenstein Lantman, E. M.; Deckert-Gaudig, T.; Mank, A. J. G.; Deckert, V.; Weckhuysen, B. M., Catalytic processes monitored at the nanoscale with tip-enhanced Raman spectroscopy. *Nat. Nanotechnol.* **2012**, *7*, 583.

(6)   Deckert-Gaudig, T.; Deckert, V., Tip-enhanced Raman scattering (TERS) and high-resolution bio nano-analysis-a comparison. *Phys. Chem. Chem. Phys.* **2010**, *12*, 12040.

(7)   Yeo, B.-S.; Stadler, J.; Schmid, T.; Zenobi, R.; Zhang, W., Tip-enhanced Raman Spectroscopy – Its status, challenges and future directions. *Chem. Phys. Lett.* **2009**, *472*, 1.

(8)   Domke, K. F.; Pettinger, B., Studying Surface Chemistry beyond the Diffraction Limit: 10 Years of TERS. *Chem.Phys.Chem.* **2010**, *11*, 1365.

(9)   Hartschuh, A., Tip-Enhanced Near-Field Optical Microscopy. *Angew. Chem. Int. Ed.* **2008**, *47*, 8178.

(10)   Neacsu, C.; Berweger, S.; Raschke, M. B., Tip-Enhanced Raman Imaging and Nanospectroscopy: Sensitivity, Symmetry, and Selection Rules. *Nanobiotechnol.* **2007**, *3*, 172.

(11)   Stadler, J.; Schmid, T.; Zenobi, R., Developments in and practical guidelines for tip-enhanced Raman spectroscopy. *Nanoscale* **2012**, *4*, 1856.

(12)   Stockle, R. M.; Suh, Y. D.; Deckert, V.; Zenobi, R., Nanoscale chemical analysis by tip-enhanced Raman spectroscopy. *Chem. Phys. Lett.* **2000**, *318*, 131.

(13)   Cançado, L. G.; Hartschuh, A.; Novotny, L., Tip-enhanced Raman spectroscopy of carbon nanotubes. *J. Raman. Spectrosc.* **2009**, *40*, 1420.

(14)   Cançado, L. G.; Jorio, A.; Joselevitch, E.; Hartschuh, A.; Novotny, L., Mechanism of Near-Field Raman Enhancement in One-Dimensional Systems. *Phys. Rev. Lett.* **2009**, *109*, 186101/1.

(15)   Pagliusi, P.; Lagugné-Labarthet, F.; Shenoy, D. K.; Dalcanale, E.; Shen, Y. R., Sensing Vase-to-Kite Switching of Cavitands by Sum-Frequency Vibrational Spectroscopy. *J. Am. Chem. Soc.* **2006**, *128*, 12610.

(16)   Blaudez, D.; Buffeteau, T.; Cornut, J. C.; Desbat, B.; Escafre, N.; Pézolet, M.; Turlet, J. M., Polarization modulation FTIR spectroscopy at the air-water interface. *Thin Solid films* **1994**, *242*, 146.

(17)   Zheng, Y. B.; Payton, J. L.; Chung, C.-H.; Liu, R.; Cheunkar, S.; Pathem, B. K.; Yang, Y.; Jensen, L.; Weiss, P. S., Surface-Enhanced Raman Spectroscopy to Probe Reversibly Photoswitchable Azobenzene in Controlled Nanoscale Environments. *Nano Lett.* **2011**, *11*, 3447.

(18)   Marquestaut, N.; Martin, A.; Talaga, D.; Servant, L.; Ravaine, S.; Reculusa, S. p.; Bassani, D. M.; Gillies, E.; Lagugné-Labarthet, F. o., Raman Enhancement of Azobenzene Monolayers on Substrates Prepared by Langmuir−Blodgett Deposition and Electron-Beam Lithography Techniques. *Langmuir.* **2008**, *24*, 11313.

(19)   Galarreta, B. C.; Norton, P. R.; Lagune-Labarthet, F., SERS Detection of Streptavidin/Biotin Monolayer Assemblies. *Langmuir* **2011**, *27*, 1494.

(20)   Merklin, G. T.; He, L.-T.; Griffiths, P. R., Surface-enhanced infrared absorption spectrometry of p-nitrothiophenol and its disulfide. *Appl. Spectrosc.* **1999**, *53*, 1448.

(21)   Quabis, S.; Dorn, R.; Eberler, M.; Glöckl, O.; Leuchs, G., Focusing to a tighter spot. *Optics Commun.* **2000**, *179*, 1.

(22)   Novotny, L.; Beverluis, M. R.; Youngworth, K. S.; Brown, T. G., Longitudinal Field Modes Probed by Single Molecules. *Phys. Rev. Lett.* **2001**, *86*, 5251.

(23)   Lieb, M. A.; Meixner, A. J., A high numerical aperture parabolic mirror as imaging device for confocal microscopy *Opt. Express* **2001**, *8*, 458.

(24)   Bouhelier, A.; Beversluis, M.; Novotny, L., Plasmon coupled tip-enhanced near-field optical microscopy. *J. Microsc.* **2003**, *210*, 220.

(25)   Stadler, J.; Schmid, T.; Opilik, L.; Kuhn, P.; Dittrich, P. S.; Zenobi, R., Tip-enhanced Raman spectroscopic imaging of patterned thiol monolayers. *Beilstein J. Nanotechnol.* **2011**, *2*, 509.

(26)   Picardi, G.; Chaigneau, M.; Ossikovski, R.; Licitra, C.; Delapierre, G., Tip enhanced Raman spectroscopy on azobenzene thiol self-assembled monolayers on Au(111). *J. Raman. Spectrosc.* **2009**, *40*, 1407.

(27)   Yang, Z.; Aizpurua, J.; Xu, H., Electromagnetic field enhancement in TERS configurations. *J. Raman Spectrosc.* **2009**, *40*, 1343.

(28)   Deckert-Gaudig, T.; Deckert, V., Ultraflat Transparent Gold Nanoplates—Ideal Substrates for Tip-Enhanced Raman Scattering Experiments. *Small.* **2009**, *5*, 432.

(29)   Deckert-Gaudig, T.; Bailo, E.; Deckert, V., Tip-enhanced Raman scattering (TERS) of oxidised glutathione on an ultraflat gold nanoplate. *Phys. Chem. Chem. Phys.* **2009**, *11*, 7360.

(30)   Treffer, R.; Lin, X.; Deckert-Gaudig, T.; Deckert, V., Distinction of nucleobases - a tip-enhanced Raman approach. *Beilstein J. Nanotechnol.* **2011**, *2*, 628.

(31)   Deckert-Gaudig, T.; Rauls, E.; Deckert, V., Aromatic Amino Acid Monolayers Sandwiched between Gold and Silver: A Combined Tip-Enhanced Raman and Theoretical Approach. *J. Phys. Chem. C* **2010**, *114*, 7412.

(32)   Huang, Y. F.; Wu, D. Y.; Zhu, H. P.; Zhao, L.-B.; Liu, G.-K.; Ren, B.; Tian, Z.-Q., Surface-enhanced Raman spectroscopic study of p-aminothiophenol. *Phys. Chem. Chem. Phys.* **2012**, *14*, 8485.

(33)   Wan, L.-J.; Terashima, M.; Noda, H.; Osawa, M., Molecular orientation and ordered structure of benzenethiol adsorbed on gold(111). *J. Phys. Chem. B* **2000**, *104*, 3563.

Chapter 5

5 Tip-enhanced Raman Spectroscopy of Graphene Layers on Flat Gold Nanoplates Substrate

In this study, tip-enhanced Raman spectroscopy (TERS) is used to characterize graphene layers using the gap-mode geometry. Such geometry provides larger enhancement of the local electromagnetic field since the small distance between the TERS tip and the Au substrate provides access to sub 10 nm gap sizes thus providing higher local confinement in the vicinity of the interface formed by the tip and the gold flat surface. Few-layer graphene platelets are deposited onto ultra-flat gold substrates using a surfactant assisted method. A gold coated AFM tip is subsequently used to probe specific substrate regions occupied by the platelets. TERS spectra were collected on distinctive points on the graphene layers using radially or linearly polarized excitation sources, with an excitation wavelength of 632.8 nm. The position, width and intensity of G, D, and 2D Raman-active modes of graphene are discussed as a function of the incident light polarization and for distinct positions on the graphene layer. We report here on the nature of the collected TERS spectra focusing in particular on the edges of the graphene platelets.

5.1 Introduction

Carbon-based materials play a major role in today's science and technology. In particular, graphene is well known for its unique electrical and mechanical (robustness, flexibility) properties. The scalability of graphene devices to nanoscale dimensions makes them promising candidates for applications in nano-optoelectronics.[1,2] Ideally, characterization tools suitable for investigating graphene-based materials should be fast and non-destructive. They must offer high spatial and spectral resolution, provide

structural and electronic information, and should be applicable at both laboratory and mass production scales.

In the last two decades, Raman spectroscopy has emerged as a powerful and non-destructive technique to characterize the electronic properties and vibrational modes of a wide range of carbon nanostructures, including graphene. The micro-Raman spectrum of few-layer graphene has been studied in great detail as a function of the number of layers by Ferrari et al.[3-5] Raman spectra are relatively similar in graphene and graphite but some differences exist due to the missing interactions between stacked layers in graphene. Raman spectroscopy is one of the most widely used methods to investigate carbon materials.[6-10] However, at the scale of a single graphene flake, micro-Raman spectroscopy is limited in terms of spatial resolution by the Abbe's criterion.[11,12] Although not yet a turn-key instrument, tip-enhanced Raman spectroscopy has matured over the past decade as a characterization probe with sub-wavelength imaging capabilities and is becoming a suitable tool for leading to spatial resolutions in the 10-50 nm range in optimal conditions.[13-17]

TERS appears as a unique characterization technique combining the capabilities of Raman spectroscopy to reveal the chemical composition of solids with the high spatial resolution of scanning probe microscopy (SPM). It can be used to obtain spectroscopic analysis of a large variety of materials and biomaterials with a resolution merely depending on the probe geometry.[13,18-22] In TERS experiments, signal enhancement is generated by the excitation of surface plasmon localized at a metallic SPM tip apex by means of its coupling with the Raman modes of the specimen. Interaction between the tip apex and the near-field component of the Raman-scattered radiation is achieved by

approaching the tip to within a few nanometers of the sample's surface, which creates an increase in the observed Raman signal originating from a region determined by the radius of the tip's apex that is scanning the surface. Tip apices used for TERS are typically in the 10-20 nm diameter range for commercial SPM probes coated with a thin metallic layers such as gold or silver. In addition of improved surface sensitivity due to local electromagnetic field enhancement in the vicinity of the tip, another interesting effect is associated with TERS and specifically, the increase in spatial resolution which could extend far beyond the optical diffraction limit giving the possibility to explore the physical and chemical properties of materials at the nanoscale level.[23-25]

In this report, we present TERS analysis of few-layer graphene flakes deposited onto gold nanoplates.[26,27] In particular, the enhancement of the Raman signals allows TERS to detect subtle structural features at the edges of the graphene platelets. Furthermore, we evaluate the effect of polarization of the input excitation beam using a tightly focused linearly polarized or a radially polarized beam at the selected wavelength of 632 nm.

5.2   Material and methods

Graphene was exfoliated following the procedure proposed by Sharifi et al.[28] from highly oriented pyrolitic graphite (Sigma Aldrich Inc) using ribonucleic acid extracted from torula utilis (Aldrich) as a non-ionic surfactant. Ultrapure deionized water (18.3 MΩ cm^{-1}) was used for all solution preparations.

5.2.1 Exfoliation and Deposition of Graphene Flakes on Gold Nanoplates.

Few-layer graphene flakes were deposited on glass substrates decorated with gold nanoplates using the method originally developed by Wu et al.[29] for single-wall carbon nanotubes, adapted by Eda at al.[30] for graphene oxide and further developed by Sharifi et al.[28] for surfactant-exfoliated graphene flakes. Graphite used as a starting material for this process was ultra-sonicated for 24h in a 3:1 H_2SO_4:HNO_3 mixture, mildly oxidized in Piranha reagent (H_2SO_4:H_2O_2=4:1) and subsequently dried prior to further use. 6 mg of the resulting material were ultra-sonicated for 4h in a 0.6 g/L water solution of RNA that acts as a non-ionic surfactant to exfoliate graphite in thin sheets of graphene.[28] The slurry produced by ultra-sonication was left to sediment overnight at 2˚C in a beaker. The top three-quarters of the suspension were centrifuged at 6000 rpm for 1h, and the supernatant, largely consisting in weakly oxidized and well dispersed few- and single-layer graphene flakes,[28] was collected and used for graphene flake deposition.

The deposition process basically consists in three steps: i) 5 ml of water suspension of graphene flakes and RNA is vacuum-filtrated through a 220-nm pore size nitro-cellulose filtration membrane, which leads to the deposition of graphene flakes on the membrane if sufficiently small amounts of diluted suspensions are used to prevent re-aggregation of the flakes; ii) the filtration membrane loaded with graphene flakes is subsequently transferred onto the requisite substrate, previously decorated with gold nanoplates and is dried under load in a vacuum desiccator. iii) finally the filtration membrane is etched in consecutive acetone and methanol baths, leaving behind a random distribution of graphene domains and RNA aggregates on their substrate.

The samples were annealed on a hot plate at 540 ˚C for 30 min inside a VAC Nexus glovebox purged with nitrogen, at oxygen and moisture levels less than 2 ppm. The annealing process is known to remove the residuals of RNA from graphene.[28] Extensive characterization, including atomic force microscopy, scanning electron microscopy and conventional Raman spectroscopy was previously used to investigate the results of this process, which results in more than 50% clean graphene flakes with less than 5 layers.[28] In our case, some of these flakes are situated on top of the gold platelets and have been used for tip-enhanced Raman studies.

5.2.2   TERS setup

The TERS setup is described in Chapters 2 and 4. We used a He-Ne laser as an excitation source with an intensity set to 100 µW at the sample using the transmission setup. This power value takes into account the light absorbed by the 20 nm-thick gold nanoplates on the top of which our graphene flakes are located.
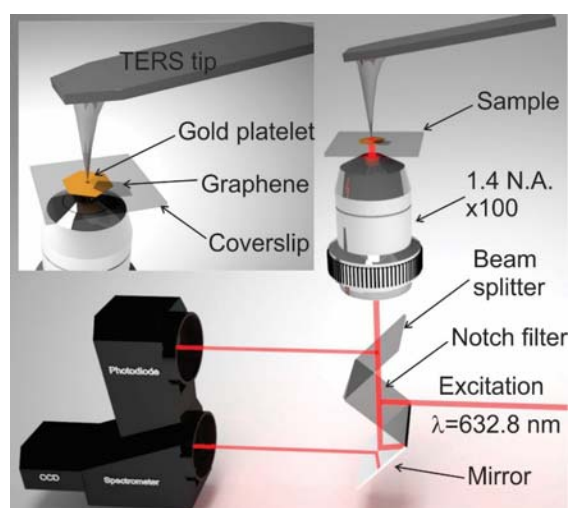
Figure 5.1 **TERS setup in back-scattering geometry.**

For this study, the AFM tip used for these experiments were prepared from commercially available silicon cantilever (NCL, NANO WORLD Innovative Technologies, typical oscillating frequency of these cantilevers are about 190 kHz with a maximum force constant of k=48 N/m. These tips have been coated with a 20 nm-thick gold layer using electron-beam induced thermal evaporation. A preliminary 3 nm layer of Ti was deposited to improve Au adhesion on Si. The Rayleigh scattering was used to align the tip as described in Chapter 2.

TERS measurements were performed for various tip-sample distances ranging from the optical near-field to far-field. Line scan measurements were performed at nanoscale resolution using step of 5 nm between two adjacent points. All Raman spectra were recorded in the 1000–3000 cm^{-1} spectral range. Laser excitation was polarized either linearly or radially for the Raman measurements. The size of the beam was adjusted to fill the entrance pupil of the high numerical aperture objective.

5.3   Results and Discussion

5.3.1   TERS Tip Alignment

In TERS, it is critical that the laser beam is tightly focused at the apex of the metallized tip. To align the laser beam coincidentally with the AFM probe, we first measured the Rayleigh scattering from the tip that scans the fixed focal volume of the excitation beam. The scattering map allows one to map the position of the tip apex and then, using the X,Y piezoelectric positioning stage of the tip, to align it exactly at the centre of the focal point. **Figure 5.2a** and **2b** show the scattering maps measured from a radial and linearly polarized beams, respectively.
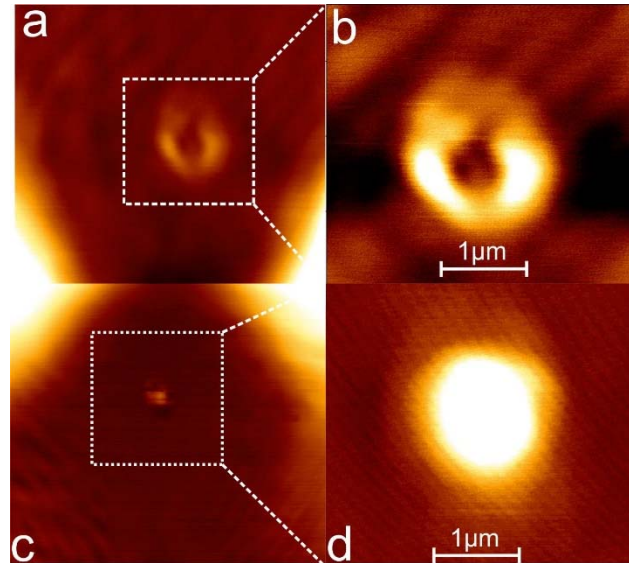
Figure 5.2 Scattered laser light from the tip apex under radial (a) and linearly polarized (b) polarization configurations.

Once the tip is coincidental with respect to the excitation light and brought in feedback with the surface of the sample, the sample stage is used to scan the sample along the X and Y directions while the Z feedback of the tip is maintained using the Z piezo actuator of the tip. In our experiments, flat gold nanoplates with thickness of around 20 nm were used as substrates onto which graphene flakes were deposited. **Figure 5.3a** and **3b** show an AFM image and topographical profile of a few-layer graphene flake placed over an isolated Au nanoplate. As shown in **Figure 5.3b**, the thickness of the flake is ~5 nm which corresponds to a number of layers ranging from 3 to 10 graphene layers. It was not possible to isolate a single-layer graphene over the gold nanoplates because of the small height contrast. For the TERS gap-mode experiments, we therefore used in this study few-layer graphene platelets deposited on Au substrate.
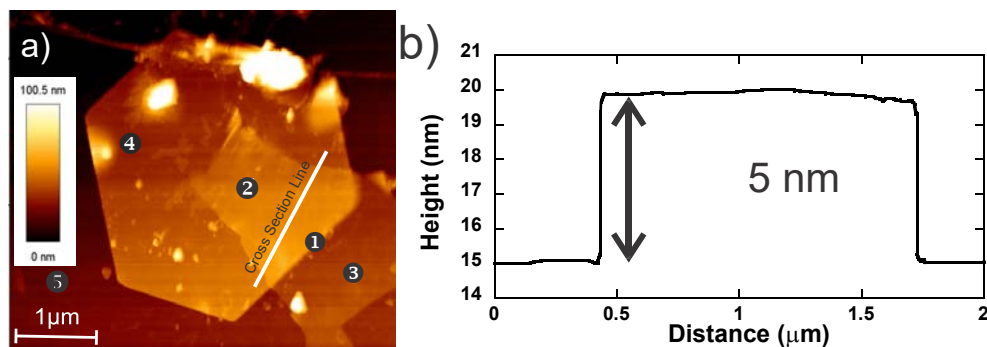
Figure 5.3 **(a) Atomic force microscopy (b) images of gold nanoplate partially covered with a graphene flake. (c) Cross section of the few-layer graphene flake deposited onto the gold nanoplate. TERS spectra were acquired on selected points 1, 2, 3, 4, 5.**

5.3.2   TERS Study of Graphene on Flat Gold Nanotube

The TERS spectra were recorded at five different positions as indicated in **Figure 5.3b** and are presented in **Figure 5.4a, b** for both radially and linearly polarized excitations, respectively.
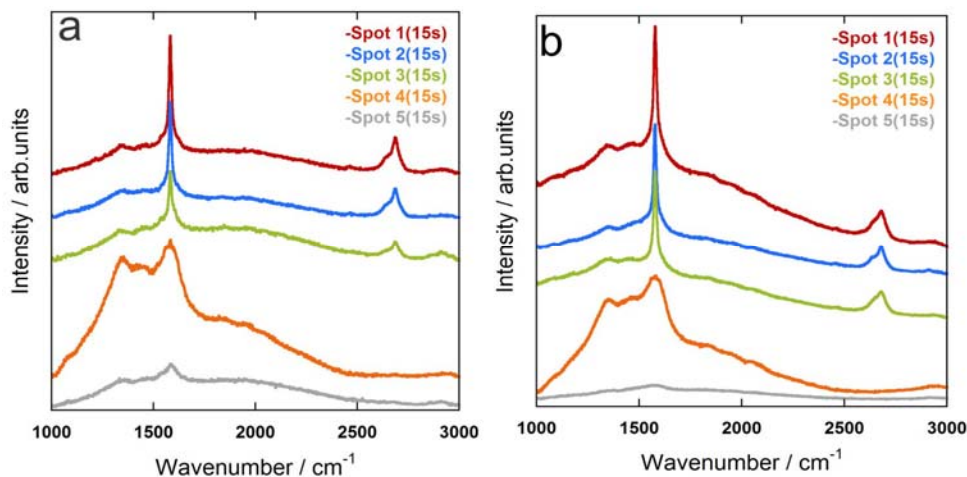
Figure 5.4 **Tip-enhanced Raman spectra measured in 5 distinct locations shown in Fig. 3a with a radially (a) and linearly (b) polarized excitation (λ = 632 nm, acquisition time = 15 s).**

The spectra reported in **Figure 5.4 a,b** were measured at five different locations on the graphene flake located on glass and on Au nanoplate (noted 1, 2, 3 in **Figure 5.3a**)

using a 15 s acquisition time. The background signal from the gold nanoplate (point 4) and for the glass coverslip (point 5) were also collected. The strongest TERS response was recorded when the tip was positioned on the edge of gold nanoplate indicated by location in spot 1 in **Figure 5.3a**. Enhancement at this specific edge may be a direct indicator of a large number of lattice defects induced by the bending of the graphene flake over the edge of the gold nanoplate. Additionally, increased sensitivity may occur on this feature because of the change in orientation of the graphene layer relative to the tip and resulting polarization of the enhanced field.
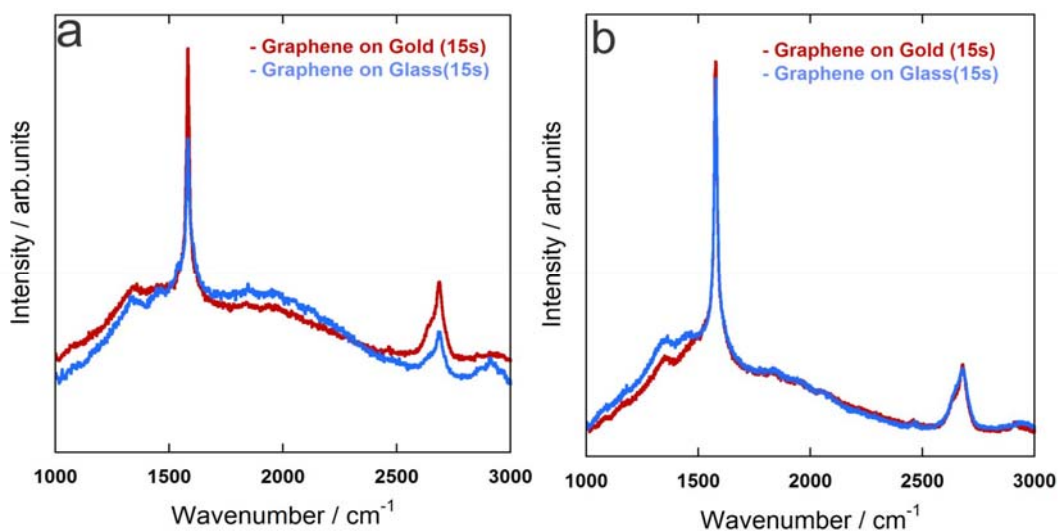
Figure 5.5 Selected TERS spectra of graphene deposited on gold and on glass acquired using radially (a) and linearly (b) polarized excitations

The TERS spectra shown in **Figure 5.5 a, b** were collected using radial and linearly polarized modes for graphene flakes located on gold and on glass coverslip. Considering the transmission geometry of our setup and the thickness of the gold nanoplate (~20 nm), a significant portion of the 632.8 nm excitation is actually absorbed by the gold nanoplate. The collected TERS signal should be corrected from the gold nanoplate absorption. Even though the measured spectra have the same magnitude, the

spectrum obtained using radial polarization is in reality obtained with much less light intensity **Figure 5.5b** also highlight that the spectra show comparable magnitude when measured with linearly polarized light meanwhile the radially polarized light shows enhanced contrast. We can therefore conclude that, in this specific geometry, the radial mode on gold nanoplate substrate appears more effective for TERS measurements yielding a higher enhancement of Raman signal from the graphene flake compared to using a linear polarization under the same conditions. All experiments described below were performed using a radially polarized mode.

The Raman spectrum of graphite and multilayer graphene consists of three fundamentally different sets of Raman phonon modes referenced as D, G and 2D. The fundamental defect mode appearing at 1333 cm^{-1} and is sensitive to the presence of defect in the graphene structure. Interestingly, The D peak behaves in a different way compared to the G (1580 cm^{-1}) and 2D (2684 cm^{-1}), because it is used to determine the number and orientation of layers, the quality and types of edge, and the effects of perturbations, such as electric and magnetic fields, strain, doping, disorder and functional groups.[31,32] In graphene study, defects play a critical role and their identification, quantification and manipulation allows one to enable a wider range of promising applications. The defect induced D band occurs because of a double resonance process that requires elastic scattering from a defect and inelastic scattering by a phonon. Thus, the maximum Raman intensity of the D mode, I(D), should be measured when the focused laser beam crosses the edges. Edges are preferred sites to attach functional groups, and their electronic and magnetic properties are different from the bulk.[32] Practically the intensity of the D band is dependent on edge type, such as whether it takes a zigzag or armchair conformation

and its Raman intensity also varies with the incident polarization. For ideal edges, the D peak is absent for zigzag configuration and large for armchair, allowing in principle the use of Raman spectroscopy as a sensitive tool to determine the edge orientation. In reality, the D to G ratio does not always show a significant dependence on edge orientation.[33] The ratio of the D to G peak intensity I(D)/I(G) may be used to identify zigzag edges, which give very low I(D)/I(G) values near 0.05 for graphene flakes obtained by micromechanical exfoliation, in contrast to intensity ratios near 0.3 reported for armchair edges.[34] For graphene flakes with only pure zigzag or armchair edges the angles formed between the edges are 2n×30º (with n = 1, 2, 3 ...). In contrast, graphene flakes with neighboring zigzag and armchair edges will have angles of (2n- 1) × 30 º (e.g., 30 º, 90 º, 150 º).[35] This angle implies, for ideal edges, that if one edge is zigzag the other must be armchair or vice-versa, but the two edges cannot have the same chirality.[36] We report in **Figure 5.6 a-c** the Raman spectra and associated I(D)/I(G) ratio for both zig-zag and armchair configurations that are 0.05 and 0.13, respectively. The Raman intensities used to calculate these ratios were integrated in the [1303-1348] cm^{-1} and the [1520-1642] cm^{-1} spectral ranges for the D and G modes, respectively.
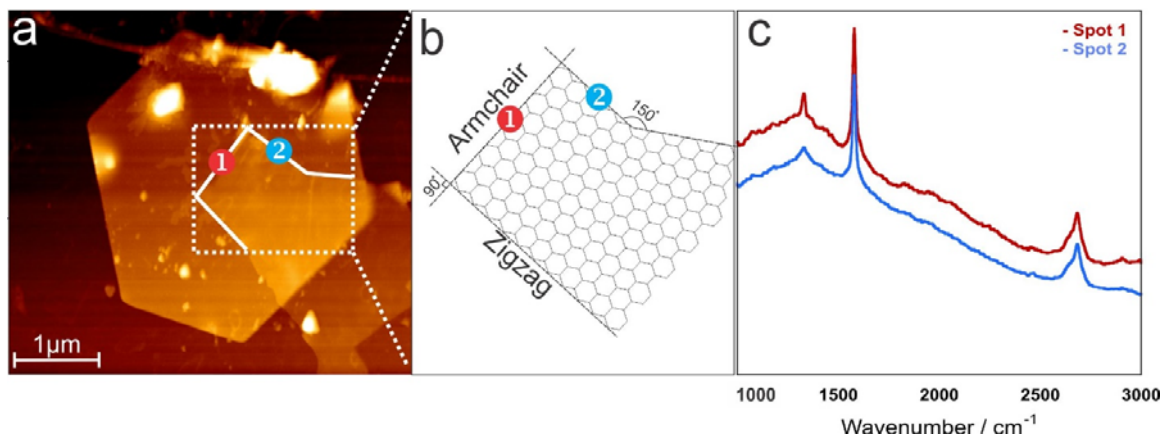
Figure 5.6 (a) AFM image (b) Schematic view of angles formed between two graphene edges. (c) TERS spectra measured at red and blue points.

The intensity of the D band also strongly depends on the angle between incident polarization and the graphene edge. It is maximum for polarization parallel to the edge and minimum when the polarization orientation is perpendicular to the edge.[35] Besides the relative orientation of the graphene plane with respect to the input polarization, it is also critical to evaluate the anisotropic effect due to the enhancement of the field along the direction normal to the surface (z direction). Although excited by a focused linearly polarized Gaussian beam, the plasmon of the metallic tip can yet be excited due to the small z component of the field along the z direction.[37] Such polarization-dependent enhancement has significant implication on the polarized Raman spectrum of the graphene. Depending on the angle of the input polarization and the overlap of the enhanced field with the graphene layer, the detected local intensity of specific flakes can be drastically different.

The other characteristic G peak appears around 1580 cm^{-1} and is observed in all graphitic forms and carbon structures having sp^2 hybridization(C–C bond). The intensity

of the G-band should, in principle, vary linearly with the number of layers. However, it is not exactly proportional to the layer number n. Since this mode is much stronger compared to other modes, it is possible that small changes due to the variation of a small number of layers are buried under the strong intensity and are not clearly visible in the experiment.
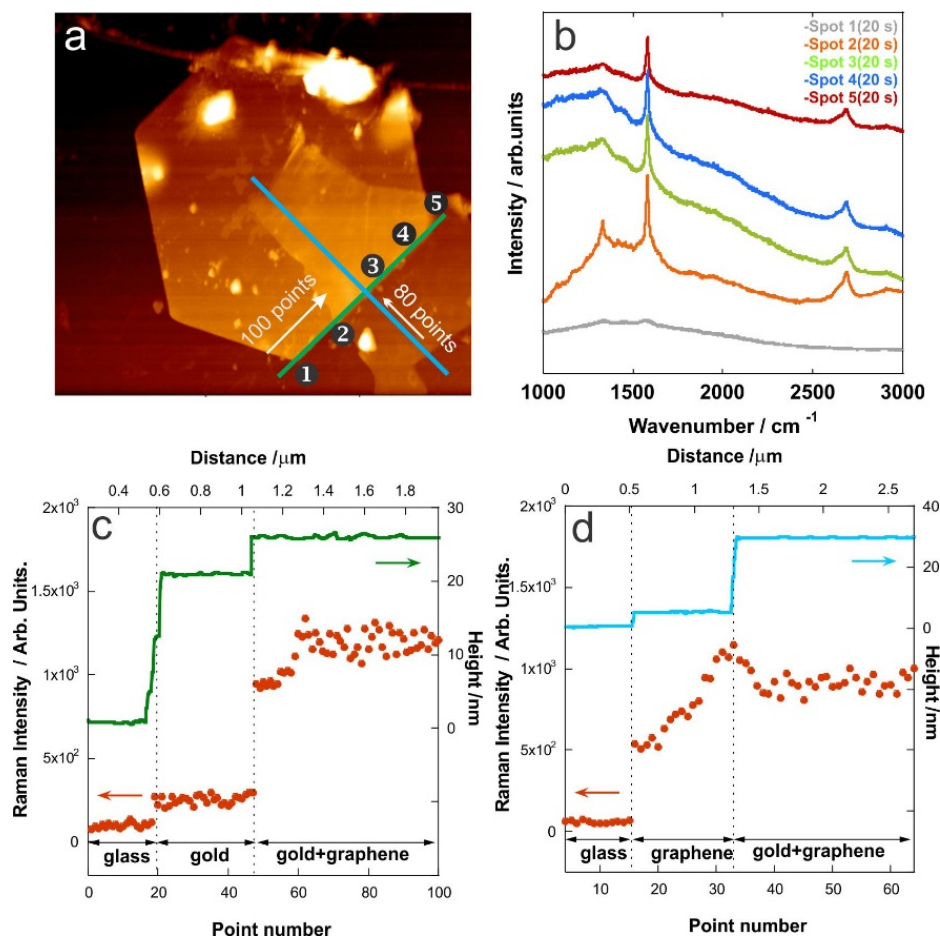
Figure 5.7(a) **AFM image with two cross Sections on edge boundaries and regions away from the edges. (b)TERS spectra were acquired on selected points 1,2,3,4,5 .(c) Cross Sections of sample and TERS signal of G band along the scanning directions indicated in green line. (d) Cross Sections of sample and TERS signal of G band along the scanning directions indicated in blue line**

The peak around 2685 cm $^{-1}$ is the so-called 2D band (or G band) and is observed in all graphitic structures. This second order resonance that appears as a doublet process

is quite sensitive to lattice perturbations affecting the vibration and electronic properties of graphene. Its position depends on the excitation energy but the shape of this peak gives information about the thickness of graphene. In measurements where the 2D band appears as a single peak indicates that we are in the presence of a single layer graphene. When a shoulder appears at lower wavenumber of the shifted 2D main peak then it can be deduced that the graphene sheet is comprised of more than one layer Ultimately the number of layers can be deduced by analyzing the shape of the peak **(Figure 5.7).** As depicted **Figure 5.7a** we measured TERS signal across the edge boundaries (green line) and across an isolated graphene layers (blue line) to investigate the vibrational and electronic properties with a nanoscale spatial resolution corresponding to the tip position during the measurements at 100 points and 80 points along the arrow in two directions. The spacing between two adjacent points is ~8 nm. **Figure 5.7b** shows selected TERS spectra of a graphene flake located along the edge of a gold flake. When going from the outside (point 1) to the inside of the graphene sheet (point 2), the intensity of the defect peak I(D) first increases, and then decreases whereas I(G) increased moving from inside to outside the flake. In **Figure 5.7c** we show the variation of intensity of the G mode together with the variation of the topography along the edge of the Au nanoplate. Further, point spectra were taken on the green line in **Figure 5.7a**. Flat regions away from the edges or structural distortions typically show no enhancement of the D peak and just enhancement in the G peak and 2D peak (Spot 3, 4, 5). **Figure 5.7d** shows a significant increase of the G mode at the edge formed by the assembly of graphene and gold platelet. The signal decrease once on the flat portion of the assembly.
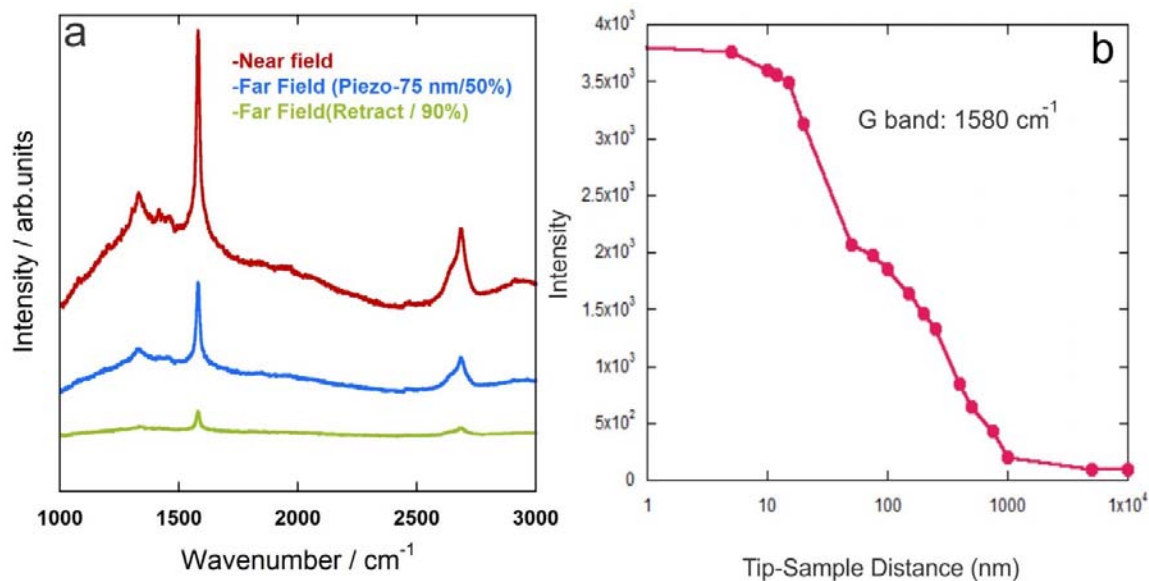
Figure 5.8 (a) Tip-enhanced Raman spectra measured in Near-field and Far-field (b) log Raman intensity versus tip-sample distance

The spectra shown in **Figure 5.8a** shows the influence of the gold tip proximity from the graphene layer varying from near-field (tip in feedback) to far-field (tip 90 and 1000 nm away from the surface). A series of Raman spectra was acquired by changing the distance between the tip and the sample while the tip was kept in feedback. These results clearly demonstrate that the highest intensity of the Raman signal is obtained when the tip is in proximity with the graphene flake. The z-distance dependence of the Raman signal graph (G mode at 1580 cm^{-1}, 20 s acquisition time per spectrum) for tip−sample separation varying from z = 5, 10, 12, 15, 20, 25, 50, 75, 100, 150, 200, 250, 400, 500, 750, 1000 nm is shown in **Figure 5.8b** using a log scale. These measurements were done using the piezo electric actuator of the tip, yet keeping the feedback at all time. Additional measurements performed when the tip is out of feedback and retracted from the surface were done at z=5000 and 10000 nm. **Figure 5.8b** highlights that the extension of the Raman signal decays rapidly after the near -field region.

5.4   Estimation of the Enhancement Factor

At 1000 nm of separation, no signal can be observed for most modes. Actually experiments have shown gap-mode enhancement to decay strongly within 20 nm and almost vanish within $1\mu m$. Thus, the increased signals could at first glance be attributed to an unambiguous TERS signal. Further experiments were performed to estimate an enhancement factor of the TERS experiments. Enhancement factors (EF) were calculated for the G band using the approach described in Chapter 2. Briefly, the contrast was first determined using equation [Eq. 1]

$$C = \frac{I_{TERS} - I_0}{I_0} \qquad [1]$$

where I_0 and I_{TERS} represent the intensity of the Raman signal with the tip away and in contact with the sample, respectively. The EF can then be estimated using Equation [Eq. 2]

$$Ef = C . \frac{d_L^2}{d_{tip}^2} \qquad [2]$$

where d_L=1 μm and d_{tip}= 0.01μm are the diameters of laser spot and tip, respectively. Contrast factors calculated using C(G) = 18 with I_{TERS}=3960 and I_0=206, provides a crude approximation of the enhancement factor in the range of $\sim 20 \times 10^4$ for the G band. The overall enhancement factor is dependent on the relative illumination volume in the near-field and far-field regimes. This allows the variations in TERS contrast to be accounted for by considering the specific volumes determining the signal and thus can explain the increase in TERS contrast for localized features such as defects on two-dimensional (2D) graphene.[38]

5.5   Conclusion

In this study, we have shown that the sensitivity of TERS is well adapted to study graphene material. The spatial resolution provided by TERS allows one to probe specifically the edges of graphene flakes. Due to the large scattering cross section of graphene and in general carbon-containing materials, TERS was successfully used to probe few-layers graphene flakes deposited on gold nanoplates. The gap mode TERS associated with distinct polarizations of the excitation beam allowed one to discriminate the edges of an individual graphene flake composed of a few layers. The analysis of the Raman spectra and intensity ratio of the D/G Raman modes provides valuable information to determine edge type and orientation of the graphene flakes. TERS appears as a critical surface technique providing surface molecular information signal as well as high spatial resolution in the 10 nm range. Future work on functionalized graphene or decorated graphene with metallic particles will be conducted using this approach.

5.6   References

(1)   Zhang, Y.; Tan, Y.-W.; Stormer, H.; Kim, P. Experimental observation of the quantum Hall effect and Berry's phase in graphene. *Nature.* **2005**, *438*, 201-204.

(2)   Geim, A.; Novoselov, K. The rise of graphene. *Nat.Mater. .* **2007**, *6*, 183-191.

(3)   Ferrari, A.; Meyer, J.; Scardaci, V.; Casiraghi, C.; Lazzeri, M.; Mauri, F.; Piscanec, S.; Jiang, D.; Novoselov, K.; Roth, S.; Geim, A. Raman spectrum of graphene and graphene layers. *Phys. Rev. Lett. .* **2006**, *97*, 187401/187401-187401/187404.

(4)   Andrea, C. F. Raman spectroscopy of graphene and graphite: Disorder, electron–phonon coupling, doping and nonadiabatic effects. *Solid. State. Commun. .* **2007**, *143*, 47–57.

(5)   Zhou, L.; Gu, H.; Wang, C.; Zhang, J.; Lv, M.; He, R. Study on the synthesis and surface enhanced Raman spectroscopy of graphene-based nanocomposites decorated with noble metal nanoparticles. *Colloids Surf., A* **2013**, *430*, 103-109.

(6)   Schedin, F.; Lidorikis, E.; Lombardo, A.; Kravets, V. G.; Geim, A. K.; Grigorenko, A. N.; Novoselov, K. S.; Ferrari, A. C. Surface-Enhanced Raman Spectroscopy of Graphene. *ACS Nano.* **2010**, *4*, 5617-5626.

(7)   Xu, W.; Ling, X.; Xiao, J.; Dresselhaus, M. S.; Kong, J.; Xu, H.; Liu, Z.; Zhang, J. Surface enhanced Raman spectroscopy on a flat graphene surface. *Proc. Natl. Acad. Sci. .* **2012**, *109*, 9281-9286.

(8)   Zhao, Y.; Liu, X.; Lei, D. Y.; Chai, Y. Effects of surface roughness of Ag thin films on surface-enhanced Raman spectroscopy of graphene: spatial nonlocality and physisorption strain. *Nanoscale.* **2014**, *6*, 1311-1317.

(9)   Sidorov, A. N.; Sławiński, G. W.; Jayatissa, A. H.; Zamborini, F. P.; Sumanasekera, G. U. A surface-enhanced Raman spectroscopy study of thin graphene sheets functionalized with gold and silver nanostructures by seed-mediated growth. *Carbon.* **2012**, *50*, 699-705.

(10)   Zhang, D.; Wang, P.; Fang, Y. The Surface-Enhanced Raman Spectroscopy of Graphene Deposited by Silver Nanoparticle Islands. *Integr Ferroelectr.* **2013**, *147*, 90-96.

(11)   Boon-Siang, Y.; Johannes, S.; Thomas, S.; Renato, Z.; Weihua, Z. Tip-enhanced Raman Spectroscopy – Its status, challenges and future directions. *Chem. Phys. Lett. .* **2009**, *472*, 1–13.

(12)   Zhang, S. G.; Zhang, X. W.; Liu, X.; Yin, Z. G.; Wang, H. L.; Gao, H. L.; Zhao, Y. J. Raman peak enhancement and shift of few-layer graphene induced by plasmonic coupling with silver nanoparticles. *Appl. Phys. Lett.* **2014**, *104*, 121109-121101 / 121109-121105.

(13)   Stockle, R. M.; Suh, Y. D.; Deckert, V.; Zenobi, R. Nanoscale chemical analysis by tip-enhanced Raman spectroscopy. *Chem. Phys. Lett.* **2000**, *318*, 131-136.

(14)   Hayazawa, N.; Inouye, Y.; Sekkat, Z.; Kawata, S. Near-field Raman scattering enhanced by a metallized tip. *Chem. Phys. Lett.* **2001**, *335*, 369-374.

(15)   Verma, P.; Ichimura, T.; Yano, T.; Saito, Y.; Kawata, S. Nano-imaging through tip-enhanced Raman spectroscopy: Stepping beyond the classical limits. *Laser. Photonics. Rev.* **2010**, *4*, 548-561.

(16)   Catalin, C. N.; Samuel, B.; Markus, B. R. Tip-Enhanced Raman Imaging and Nanospectroscopy: Sensitivity, Symmetry, and Selection Rules. *J. Nanobiotechnology.* **2009**, *3*, 172–196.

(17)   Stadler, J.; Schmid, T.; Zenobi, R. Nanoscale chemical imaging using top-illumination tip-enhanced Raman spectroscopy. *Nano Lett.* **2010**, *10*, 4514-4520.

(18)   Hartschuh, A. Tip-enhanced near-field optical microscopy. *Angew. Chem. .* **2008**, *47*, 8178-8191.

(19)   Hartschuh, A.; Qian, H.; Georgi, C.; Böhmler, M.; Novotny, L. Tip-enhanced near-field optical microscopy of carbon nanotubes. *Anal. Bioanal. Chem.* **2009**, *394*, 1787-1795.

(20)   Suzuki, T.; Itoh, T.; Vantasin, S.; Minami, S.; Kutsuma, Y.; Ashida, K.; Kaneko, T.-a.; Morisawa, Y.; Miura, T.; Ozaki, Y. Tip-enhanced Raman spectroscopic measurement of stress change in the local domain of epitaxial graphene on the carbon face of 4H-SiC(000-1). *Phys. Chem. Chem. Phys.* **2014**, *16*, 20236-20240.

(21)   Vantasin, S.; Tanabe, I.; Tanaka, Y.; Itoh, T.; Suzuki, T.; Kutsuma, Y.; Ashida, K.; Kaneko, T.; Ozaki, Y. Tip-Enhanced Raman Scattering of the Local Nanostructure of Epitaxial Graphene Grown on 4H-SiC (000Ī). *J. Phys. Chem. C'.* **2014**.

(22)   Kazemi-Zanjani, N.; Chen, H.; Goldberg, H. A.; Hunter, G. K.; Grohe, B.; Lagugne-Labarthet, F. Label-Free Mapping of Osteopontin Adsorption to Calcium Oxalate Monohydrate Crystals by Tip-Enhanced Raman Spectroscopy. *J. Am. Chem. Soc.* **2012**, *134*, 17076-17082.

(23)   Yeo, B.-S.; Amstad, E.; Schmid, T.; Stadler, J.; Zenobi, R. Nanoscale probing of a polymer-blend thin film with tip-enhanced Raman spectroscopy. *Small* **2009**, *5*, 952-960.

(24)   Taka-aki, Y.; Prabhat, V.; Yuika, S.; Taro, I.; Satoshi, K. Pressure-assisted tip-enhanced Raman imaging at a resolution of a few nanometres. *Nat.Photonics.* **2009**, *3*, 473 - 477.

(25)   Deckert-Gaudig, T.; Deckert, V. Ultraflat Transparent Gold Nanoplates—Ideal Substrates for Tip-Enhanced Raman Scattering Experiments. *Small.* **2009**, *5*, 432-436.

(26)   Deckert-Gaudig, T.; Bailo, E.; Deckert, V. Tip-enhanced Raman scattering (TERS) of oxidised glutathione on an ultraflat gold nanoplate. *Phys. Chem. Chem. Phys.* **2009**, *11*, 7360-7362.

(27)   Pashaee, F.; Hou, R.; Gobbo, P.; Workentin, M. S.; Lagugne-Labarthet, F. Tip-Enhanced Raman Spectroscopy of Self-Assembled Thiolated Monolayers on Flat Gold Nanoplates Using Gaussian-Transverse and Radially Polarized Excitations. *J. Phys. Chem. C.* **2013**, *117*, 15639-15646.

(28)   Sharifi, F.; Bauld, R.; Ahmed, M. S.; Fanchini, G. Transparent and Conducting Graphene–RNA-Based Nanocomposites. *Small.* **2012**, *8*, 699-706.

(29)   Wu, Z.; Chen, Z.; Du, X.; Logan, J. M.; Sippel, J.; Nikolou, M.; Kamaras, K.; Reynolds, J. R.; Tanner, D. B.; Hebard, A. F.; Rinzler, A. G. Transparent, Conductive Carbon Nanotube Films. *Science.* **2004**, *305*, 1273-1276.

(30)   Eda, G.; Fanchini, G.; Chhowalla, M. Large-area ultrathin films of reduced graphene oxide as a transparent and flexible electronic material. *Nat. Nano.* **2008**, *3*, 270-274.

(31)   Ferrari, A. C.; Basko, D. M. Raman spectroscopy as a versatile tool for studying the properties of graphene. *Nat. Nano.* **2013**, *8*, 235-246.

(32)   Stadler, J.; Schmid, T.; Zenobi, R. Nanoscale Chemical Imaging of Single-Layer Graphene. *ACS Nano.* **2011**, *5*, 8442-8448.

(33)   Krauss, B.; Nemes-Incze, P. t.; Skakalova, V.; Biro, L. s. P.; Klitzing, K. v.; Smet, J. H. Raman Scattering at Pure Graphene Zigzag Edges. *Nano Lett.* **2010**, *10*, 4544-4548.

(34)   Casiraghi, C.; Hartschuh, A.; Qian, H.; Piscanec, S.; Georgi, C.; Fasoli, A.; Novoselov, K. S.; Basko, D. M.; Ferrari, A. C. Raman Spectroscopy of Graphene Edges. *Nano Lett.* **2009**, *9*, 1433-1441.

(35)   Wang, P.; Zhang, D.; Li, L.; Li, Z.; Zhang, L.; Fang, Y. Reversible Defect in Graphene Investigated by Tip-Enhanced Raman Spectroscopy. *Plasmonics.* **2012**, *7*, 555-561.

(36)   Luo, Z.; Kim, S.; Kawamoto, N.; Rappe, A. M.; Johnson, A. T. C. Growth Mechanism of Hexagonal-Shape Graphene Flakes with Zigzag Edges. *ACS Nano.* **2011**, *5*, 9154-9160.

(37)   Kazemi-Zanjani, N.; Vedraine, S.; Lagugne-Labarthet, F. Localized enhancement of electric field in tipenhanced Raman spectroscopy using radially and linearly polarized light. *Opt. Express.* **2013**, *21*, 25271/25271-25271/25276.

(38)   Maximiano, R. V.; Beams, R.; Novotny, L.; Jorio, A.; Cançado, L. G. Mechanism of near-field Raman enhancement in two-dimensional systems. *Phys. Rev. B.* **2012**, *85*, 235434/235431-235434/235438.

Chapter 6

6   Tip-enhanced Raman Spectroscopy of DNA for β_2-adrenergic receptor on Flat Gold Nanoplates Substrate Using Radially Polarized Excitations

In the recent literature TERS has been used as a valuable technique to investigate a variety biomolecules such as DNA (Deoxyribonucleic acid) and RNA (Ribonucleic acid). TERS provides pristine molecular information from DNA through the detection of their vibrational finger prints together with nanoscale topography. In this chapter, we use gap-mode TERS with a radially polarized laser source to probe cDNA chains deposited onto Au ultra-flat nanoplates. More specifically, adrenergic signaling that controls the contraction of cardiac myocyte cells and the beating of the mammalian heart is initiated by ligand binding to β_2-adrenergic receptors (β_2ARs) contained in nanoscale multi-protein complexes at the cellular membrane. Herein, we demonstrate that TERS appears as an ultrasensitive label-free technique for characterization of a plasmid free β_2AR cDNA along with its embedded cDNA in plasmid with an optical resolution down to 8 nm. This offers not only a tool to differentiate these two nanoscale specimens, but also to study the localization of the majority of nucleic acids present on each selected region on the cDNA strand.

6.1   Introduction

In medical and biological research it is often of importance to monitor the interaction of small molecules with DNA, such as cancer drugs intercalation the DNA chain.[1] DNA sequencing as a valuable method requires visualization and separation techniques to recognize DNA fragments.[2] More importantly, the determination of the exact nucleobase sequence of DNA is of substantial

significance for research in the life sciences.[3] The first sequencing methods were published in 1977 by Maxam and Gilbert,[4] and Sanger et al.[1] Since then, the sequencing technology has been further developed to be automated. Current advances provide a tendency towards single-molecule sequencing. This eventually results in the development of sequencing systems with expenditure of time and reasonable costs.[5]

Powerful spectroscopic techniques including Raman scattering and IR absorption have been used for the label-free determination of DNA genomic investigations.[6] Raman spectroscopy in particular provides a unique fingerprint of the molecules of interest and is therefore a highly appropriate tool to study small biomolecules such as DNA and RNA and other biological samples.[7] Many spectroscopic techniques such as conventional Raman and infrared spectroscopies, nuclear magnetic resonance (NMR) and mass-spectroscopy can provide label-free structural characterization of a biomolecule such as a protein. However, those are lacking the spatial resolution capabilities and high sensitivity and they often require large sample quantities. In this context, surface-enhanced Raman spectroscopy (SERS) and tip-enhanced Raman spectroscopy (TERS) are two possible solutions that can enable extreme spatial resolution together with a higher surface sensitivity and specificity.[8]

The use of TERS for DNA chains has been pioneered by Deckert et al.[9,10] The first investigations focused on crystals and monolayers of DNA components, such as adenine,[11] cytosine and thymine,[9] DNA base nanocrystals,[9,11,12] and a study of the hydrogen bonding between adenine and thymine on a gold substrate.[13]

Recently, TERS spectra of a single-stranded (ss) calf thymus DNA macromolecules immobilized non-specifically on a mica substrate have been studied and revealed specific bands for each nucleobase.[3]

Further field enhancement can be achieved by employing metal substrate onto which the DNA chain is deposited. The choice of gold thin and flat nanoplates was driven by several factors, such as (i) the transmission geometry of the setup that requires a small thickness of gold in order to optimize the laser intensity going through the gold substrate, (ii) a flat surface of gold that can be functionalized with biological molecules such as DNA molecules with minimum surface enhancement effects from the nanoplate itself, and (iii) the interest to benefit from the TERS "gap mode", where DNA molecule is isolated between two metallic interfaces, i.e. the gold substrate and the metallic tip.[3,14-17]

The human β_2-adrenergic receptor gene is situated on the long arm of chromosome 5. This receptor is a member of the 7-transmembrane family of receptors and is composed of 413 amino acid residues.[18] The study of β_2-adrenergic cDNA and receptors is of great interest since its agonists are used widely as bronchodilators and also in combination therapy with inhaled corticosteroids in the treatment of respiratory diseases, such as asthma and chronic obstructive pulmonary disease. Knowledge of the function, response, and regulation of the β_2-receptor is also important to the clinician in interpreting patient response to both short- and long-acting β_2-agonists. Similarly, an understanding of the mechanisms of receptor desensitization that might lead to tolerance and rescue therapy is useful.[19] Adrenergic signaling that controls the contraction of cardiac

myocyte cells and the beating of the mammalian heart is also initiated by ligand binding to β_2ARs contained in nanoscale multi-protein complexes at the cellular membrane. Considering the important roles of this specific family of receptor, basic information about the cDNA of these receptors offers wealthy information for further cell biological and physiological studies specifically in transfection process of immortalized cell lines using a cDNA. This information can also be useful for biophysical and surface chemistry applications such as cell micro patterning techniques for controlled biological studies on transfected cells.[13]

In this work, we used a gap-mode TERS with a radially polarized laser source on Au ultra-flat nanoplates to study the functionalized β_2AR cDNA strands on the nanoplates. The cDNA molecules are probed with a gold coated AFM tip in order to obtain largest electromagnetic field enhancement from the localized surface plasmon resonance (LSPR) generated between the gold tip and the functionalized flat gold surface. Herein, TERS is used for characterization of single chains of plasmid free β_2AR cDNA along with its embedded cDNA in plasmid. This provides not only a tool to differentiate these two nanoscale specimens, but also to study the localization of the majority of nucleobases present on each selected region on a cDNA strand together with a high spatial resolution.

6.2   Experimental Section

6.2.1   Preparation of Gold Nanoplate Substrates Sample Preparation

Synthesis of gold (111) nanoplates is reported in chapter 3 of this thesis. The resulting gold nanoplates used in this study were collected from a fresh batch, they

have typical thickness of 20 nm and base dimension of several microns. The gold plates were subsequently released by sonication followed by drop-casted onto clean Quartz coverslips (120 mm thickness). AFM characterization of individual nanoplates shows roughness in the range of about 500 pm.

6.2.2   cDNA Preparation and Purification

β2 adrenergic receptor (β2AR)-Flag tagged plasmid was digested using HindIII and XbaI enzymes from the Fast Digest kit (Life Technologies). About 5μg of DNA was incubated with both enzymes at 37˚C for 20 minutes. Control pcDNA1.1 plasmid without the β2AR-Flag insert was also digested using the same conditions. The digested fragments were subjected to agarose gel electrophoresis (0.7% w/v). The DNA was stained using RedSafe (FroggaBio) and the band relative to the β2AR-Flag was extracted under UV light. The expected size for the human β2AR DNA plus the Flag tag is about 1.1 Kb. The expected size for the pcDNA1.1 plasmid is 4.8 Kb. GeneRuler 1Kb plus DNA ladder was used as a reference. The β2AR-Flag band was purified using a gel extraction kit (Qiagen). Some of the purified DNA was subjected to agarose gel electrophoresis (0.7% w/v) and compared to the non-digested original plasmid.

6.2.3   Deposition of cDNA Strands on Gold Nanoplates

A coverslip was coated with 10^{-2} M of APTMS for 2 hour and it was rinsed with MilliQ water and dried under nitrogen gas. Few drops of as-prepared gold nanoplate solution was drop casted onto the coverslip for 30 min with subsequent rinse with MilliQ water to prevent the aggregation of non-attached gold nanoplates. A 10-15 μL of the cDNA solution was drop casted onto the as-

prepared substrate of gold nanoplates for 5 min. The substrate was then rinsed few times with MilliQ water to remove any remaining of the solvent of cDNA.

6.2.4   TERS Tip Preparation

A deposition of 5 nm Ti with subsequent 30 nm of Au was conducted on a commercial silicon AFM tip (NCL50) for the preparation of a TERS tip. As-prepared TERS tip was annealed for 30 min at 180°C to generate more uniform gold Island at the apex of the TERS tip. This step was added to the process to maintain the integrity of the TERS tip during AFM imaging and collecting TERS signals.

6.2.5   TERS Setup

The TERS setup used in this study is described in Chapter 2. The AFM tip used for these experiments was prepared from commercially available silicon cantilever (NCL, NANO WORLD Innovative Technologies, f = 190 kHz, k = 48 N m^{-1}). These tips have been coated with a 5 nm of Titanium as an adhesion layer followed by 30 nm of gold using electron-beam evaporation. All Raman spectra were recorded in the 1000–3000 cm^{-1} spectral range. Laser excitation was either linearly polarized or was modified using a liquid crystal modulator with phase compensation (ARCoptix) to obtain radially polarized light. The size of the beam was adjusted to fill the entrance pupil of the objective.

6.3   Results and Discussion

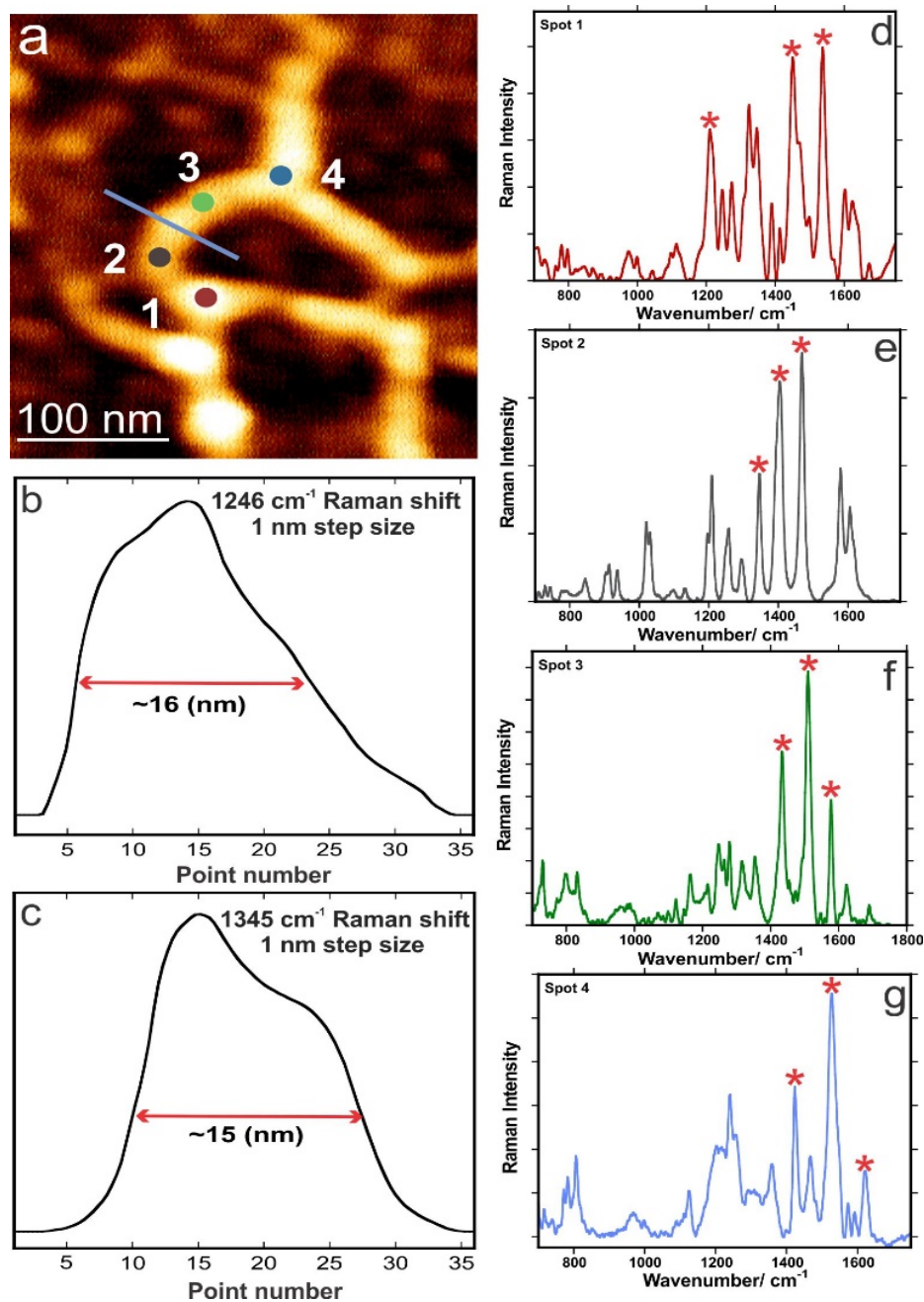### 6.3.1   Nanoscale Topography and Fingerprint of Plasmid-free β_2AR cDNA

TERS experiments appears ideally suited to probe and possibly identify nanoscale structures as DNA and RNA.[20] Prior to any TERS measurement, an AFM scan of the surface allows to distinguish topographical features with nanoscale resolution such as the individual cDNA chains deposited onto the surface This provides the accurate topographical regions to be selected and further probed with TERS. As mentioned earlier, ultra-smooth gold nanoplates with thicknesses of ~20 nm were used as substrate onto which cDNA strands were deposited. An AFM topographical image of a single hexagonal nanoplate deposited onto a quartz window is shown in **Figure 6.1a.**

A random assortment of cDNA strands is also shown both on the gold nanoplate and also on the bare quartz in **Figure 6.1b, c**. Although the random assortment of cDNAs introduces a difficulty of finding them on the substrate, this localization can be used for two-fold purposes including i) conducting the TERS experiment on the cDNA strands located on the nanoplates and ii) using the cDNAs located on the quartz surface as a non-TERS control experiment. A single plasmid-free cDNA strand located onto the gold plate is presented in **Figure 6.1d** along with its topographical cross section shown in inset. Based upon this cross section, a 4 nm height with widths of 17 and 18 nm was observed for this specific plasmid-free cDNA. The measured width are convoluted with the AFM tip geometry and the height of the cDNA is the most accurate measurement to determine an average diameter which in good agreement with previous published studies obtained on similar objects. [21]
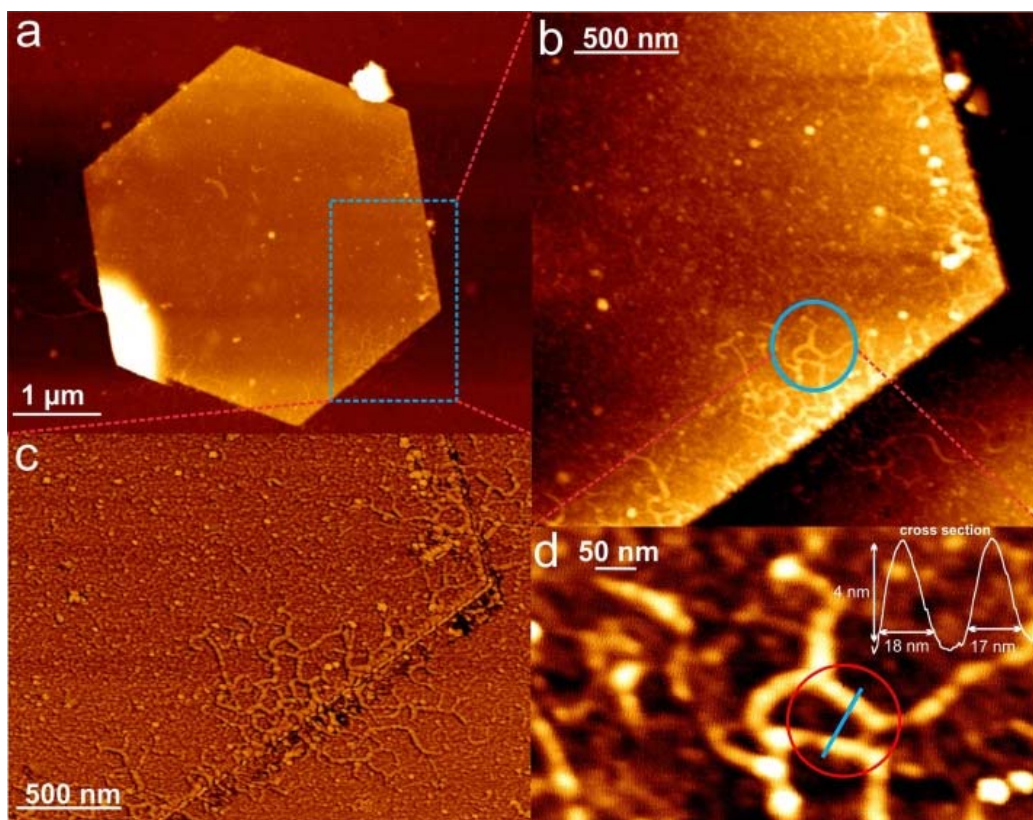
Figure 6.1 AFM nanoscale topography of plasmid-free β2AR cDNA. a) AFM height image of single isolated Au nanoplate; b, c) AFM height and phase images of the selected region in (a), respectively; d) AFM height image showing a cDNA strand adsorbed on the Au nanoplate; and the cross section of DNA is shown in inset, presenting the nanoscale topography of the cDNA.

Subsequent to the AFM scans, TERS is conducted to provide vibrational information of the selected regions indicated in **Figure 6.2a**. A preliminary TERS scanning of the sample was performed to evaluate the spatial resolution performance of the used tip. For this, the tip was scanned across the orthogonal direction with respect to the chain axis and the signal of an intense Raman mode was integrated as shown in **Figure 6.2b, c** for the modes at 1246 and 1345 cm^{-1}, respectively.

Figure 6.2 Nanoscale TERS spatial resolution and chemical fingerprint of plasmid-free β₂AR cDNA. (a) AFM topography image of a cDNA strand adsorbed on a gold nanoplate. (b,c) TERS intensity profiles derived from integration of TERS bands of 1246, and 1345 cm⁻¹. (d-g) TERS fingerprint of different spots on the cDNA strand, respectively.

Table 6-1 TERS chemical assignment of plasmid-free β₂AR cDNA[3,9,22-29] Raman modes are named: ν (stretching), δ (bending), s (symmetric). Abbreviations: s (strong), m (medium), w (weak)

1	2	3	4	Assignment (plasmid-free cDNA)	Ref
665w		670w	672m	G (ring breathing)	[1, 2]
-	687w	683w	699m	C C_5C_4-N_3C_4	[11]
709w	709w		716w	A (in-plane ring breathing)	[1, 3]
		730m	738w	A Ring stretching	[11]
762w	742w			T Ring breathing	[1,4,5]
		773w	770m	T Ring breathing	[11]
			782m	C Ring breathing	[10]
		802w	806m	Tris-HCl	[3]
		855w	851w	G N_7C_5-$N_1C_2N_3$	[11]
869w				Deoxyribose ring	[1,6,10]
		906w		A/C/G ρ (NH_2) NH_2 Rocking; Deoxyribose	[1,2,10]
940w	936w			A/C/G δ (NH_2) NH_2 Rocking + δ(C–H) + δ(ring)	[1, 2, 4]
974w				T ν_s (C-C), ν_s (C-O), ribose	[1, 7]
998w			997w	T Out-of-plane δ(NH_2) wagging	[1,4]
-	1020m			C NH_2 + C_6-H	[11]
	1028m		1028w	A ν_s(N-C) N-Sugar Stretching A NH_2 + N_9-H	[1,2,11]
1043w		1042w	1046w	T Out-of-plane δ(CH_3) wagging	[4]
1113m		1099w	1089w	PO_2	[1]
		1122m	1124m	C ν(C_5C_6–C_6N_1) + δ(C_5H) in-plane A N_3C_2 + N_9-H	[4,11]
	1131w			A ν(C_8–N_9), δ(N_9–H, C_8–H)	[1,4]
	1166w	1164m		A/G ν_s(C_5-C_6) C-C Stretching	[1, 2]
	1196m			C	[1,8]
1210s	1208s		1202s	T ν_s(C-C) Ring-CH_3 Stretching	[1,2,7]
		1216m		T in-plane ν_s(C–CH_3)	[1,4]
1246s	1256s	1246m	1240s	A δ(C_8–H, N_9–H), ν(N_7–C_8) C ν_s(C-C) Ring-CH_3 Stretching G ν_s(C_8–N_9) C-N Stretching T In-plane ν(ring)	[1,2,4,5]
1274s		1278s		C ν(C–NH_2) + in-plane ν(ring) T Ring + CH G C_8N_7-N_1C_6 + N_7C_5	[1,4,11]
	1296m		1291s	C ν_s (C_2-N_3) C-N Stretching	[1,2,9]
		1314m		A ν (C_2–N_3, N_1–C_2, C_5–C_6, C_5–N_7) G ν_s (C-N) C-N Stretching (Im)	[2,4]
1324s			1336w	A/G Ring mode	[1,6]
1346s	1345s	1353s		T N_3H-C_4=O	[11]
			1359m	A/C/T/G ν_s (C-N) C-N Stretching (py)	[1,2]

1390s	1403s		1398w	T δ(NH) deformation δ(CH$_3$) CH$_3$ deformation	[1,2,4]
1413m				A δ(C$_2$–H, N$_9$–H), ν(C$_8$–N$_9$, C$_4$–N$_9$) C ν_s(C$_4$-C$_5$) C-C Stretching T δ(NH) + in-plane ν(ring)	[1,2,4]
		1433s	1423s	C	[11]
1451s		1455w		A C$_2$H-N$_1$C$_2$ + N$_3$C$_2$ / G N$_1$C$_2$-N$_1$C$_6$	[11]
	1468s	1473w	1467s	A ν_s(C=N) C=N Stretching (Py) T –N$_1$C$_2$ + C$_2$N$_3$	[1,2,11]
1499m				G ν_s(C=N) C=N Stretching (Im)	[1,2]
		1509s	1527s	C δ (NH$_2$) NH$_2$ Deformation G C$_4$C$_5$-C$_4$N$_9$	[1,2,11]
1538s		1547w		T in-plane ring stretching	[1,4]
	1578s	1577s	1573m	A/C/G/T Ring Stretching (Py)	[1,2]
1602s	1605s	1603w	1592m	A/C/G δ(NH$_2$) NH$_2$ Deformation	[1,2,4,11]
1672w			1669w	A β_s(NH$_2$) NH$_2$ Scissoring	[1,2]
		1683m		G C$_6$=O + C$_5$C$_6$	[11]

These peak at 1246 cm^{-1} represents several possible contributions such as δ(C$_8$–H, N$_9$–H), ν(N$_7$–C$_8$), C ν_s(C-C) Ring-CH$_3$ stretching, G ν_s (C$_8$–N$_9$) C-N stretching, T in-plane ν(ring), and the peak at 1345 cm^{-1} represents T N$_3$H-C$_4$=O.The analysis of the optical signal of these two modes provides valuable information on the optical resolution of the local measurement. The full width at half height in the curves shown in **Figure 6.2b,c** highlights a spatial resolution of roughly 15 nm. From this, several spectra were then collected on the cDNA chain and tentative assignment is reported in **Table 6.1**. As shown in **Figure 6.2d-g**, distinct spectra are recorded from distinct selected area (noted 1,2,3,4 on **Figure 6.2a**) from the cDNA chain. Considering the fact that a cDNA strand is composed of just four nucleobases of Adenine (A), Cytosine (C), Guanine (G), and Thymine (T) with different sequences, comparable fingerprint are expected albeit with distinct intensities of the individual bands since it depends on the spatial distribution of the bases located under the tip.
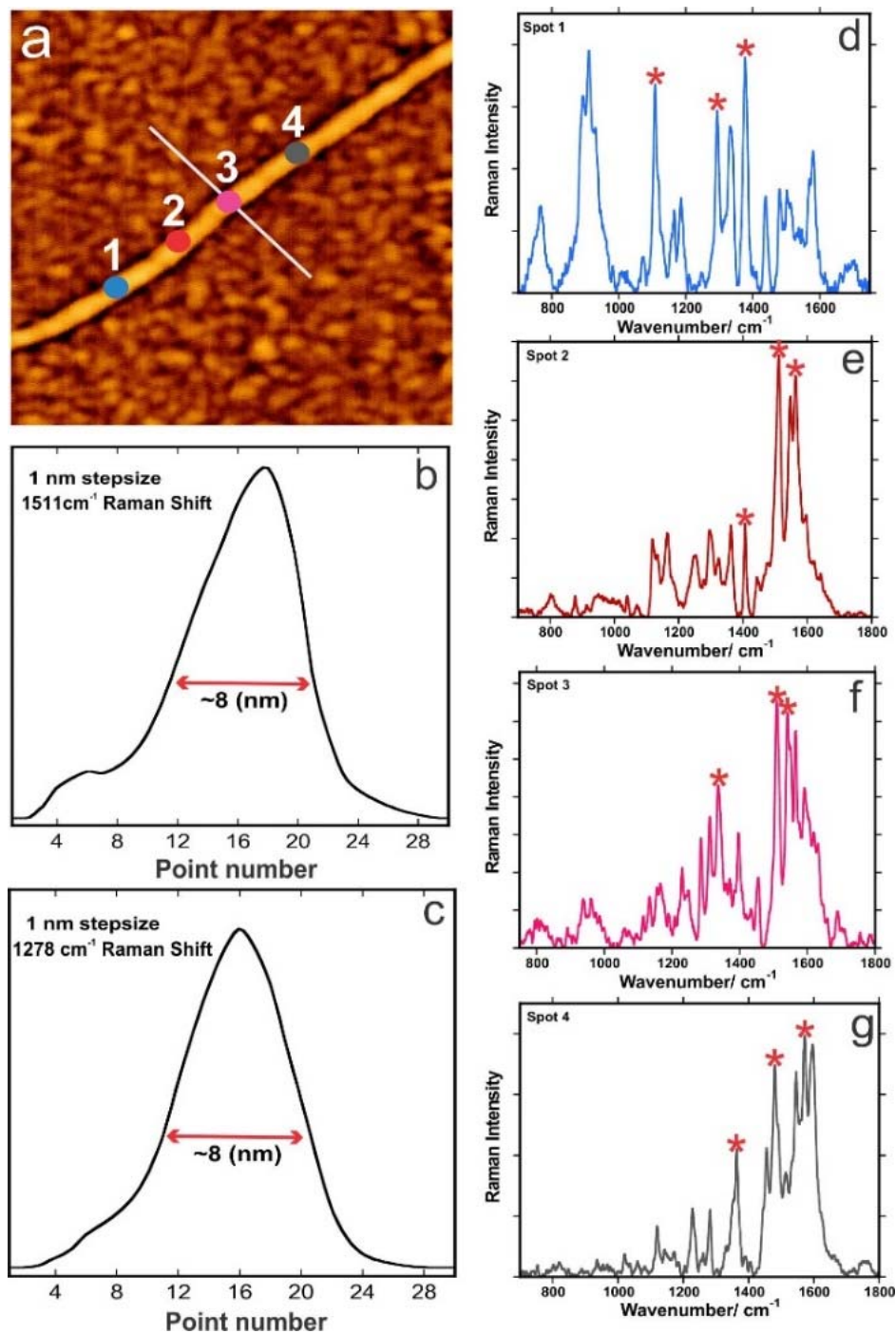
6.3.2 Nanoscale Topography and Fingerprint of Embedded β₂AR cDNA in plasmid

The same study has been conducted onto embedded cDNA in plasmid and compared with plasmid-free cDNA. As shown in **Figure 6.3,** the topographical features of embedded cDNA in plasmid is comparable with plasmid-free cDNA as expected with a height of 4 nm and width of 18 nm. However the embedded cDNA shows a more anisotropic morphology as opposed to random coil-like topography of plasmid-free cDNA.
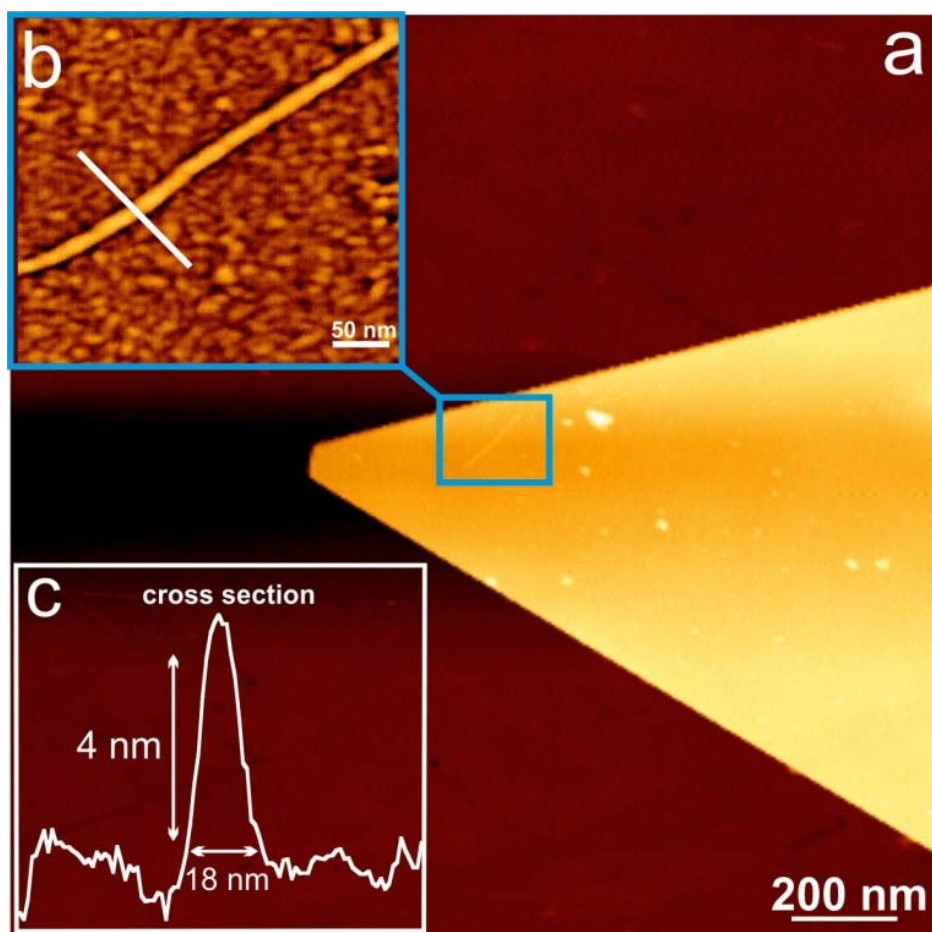
Figure 6.3 AFM nanoscale topography of embedded β₂AR cDNA in plasmid. a) AFM height image of single isolated Au nanoplate; (b) AFM phase image of the selected region in (a); (c) Cross section of cDNA, presenting the nanoscale topography of the cDNA.

The TERS spectra of different regions **(Figure 6.4a)** on an embedded cDNA in plasmid show quite different fingerprints in terms of intensities and location of peaks as shown in **Figure 6.4.** However, an improved spatial resolution up to 8 nm is observed on this sample **(Figure 6.4 b,c)** for major peaks of 1511 and 1278 cm^{-1}. This is possibly obtained due to the higher density of nucleobases provided by the surrounding plasmid generating stronger signals with improved signal-to-noise ratio. The spatial resolutions for both with and without plasmid are obtained with 30-36 points with step size of 1 nm. The peak at 1511 cm^{-1} represents the C δ (NH$_2$), and G C$_4$C$_5$-C$_4$N$_9$. The peak at 1278 cm^{-1} represents C ν_s(C–NH$_2$) + in-plane ν_s(ring), T Ring + CH, and G C$_8$N$_7$-N$_1$C$_6$ + N$_7$C$_5$. The obtained spatial resolution is not sufficient enough to ascertain the exact sequence of cDNA based on the fingerprint; however, it is still possible to determine the presence of the major nucleobase(s) present at the selected local spot of measurement under the tip. The major peaks of the spectrum in each selected regions on cDNA strand are indicated by asterisks in both **Figure 6.3** and **6.4**. The determination of the major nucleobase at each spot using these peaks will be discussed in the following section. The full assignment of the embedded cDNA in plasmid has been shown in detail in **Table 6.2.** It also has been compared with the assignment of plasmid which represents less intense peaks due to the lower density of nucleobases present at the local region of measurement. This is in good agreement with the expected higher density of nucleobases in cDNA embedded in plasmid compared to the plasmid-free cDNA leading to stronger TERS signals and an improved spatial resolution.

Figure 6.4 Nanoscale TERS spatial resolution and chemical fingerprint of embedded β2AR cDNA in plasmid. a) AFM topography image of a cDNA strand adsorbed on a gold nanoplate. b,c) TERS intensity profiles derived from integration of TERS bands of 1511, and 1278 cm⁻¹, respectively. d-g) TERS fingerprint of different spots on the cDNA strand.

Table 6-2 TERS chemical assignment of embedded β₂AR cDNA in plasmid and pure plasmid[3,9,22-29]
Raman modes are named : ν (stretching), δ (bending), s (symmetric). Abbreviations: s (strong), m (medium), w (weak),

1	2	3	4	Plasmid	Assignment (cDNA+plasmid)	Ref
729w	729w	716w			A (in-plane ring breathing)	[1, 3]
743w	741w	749w	772w		T Ring breathing	[1,4,5]
782w					T Ring breathing	[11]
816s	802w	813w	804w		T N_1C_2+N_1--H+C_5C_4+N_1C_6+N_3C_4 TRIS-HCL	[3,11]
847w		844w			G N_7C_5-$N_1C_2N_3$	[11]
	877m	869w	884w		Deoxyribose ring	[1, 6, 10]
942s		937m			A/C/G δ (NH_2) NH_2 Rocking + δ(C–H) + δ(ring)	[1, 2, 4]
960s		960m			C δ(NH) out-of-plane wagging	[4]
		976w			T ν_s (C-C) ν_s (C-O), and ribose	[1, 7]
980s		986w			C C_5H	[11]
1031w	1039w	1026w			A ν_s(N-C) N-Sugar Stretching A $\nu(NH_2)$ + N_9-H C ν(Ring) + δ(C–H) in-plane	[1,2,4,11]
	1077w	1072w	1065m		G [1,2]	[1,2]
1122m	1118s	1114m	1124m		C $\nu(C_5C_6$–$C_6N_1)$ + $\delta(C_5H)$ in-plane A N_3C_2 + N_9-H	[4.11]
	1133m	1133m	1144m		A $\nu(C_8$–$N_9)$, $\delta(N_9$–H, C_8–H)	[1,4]
1157s		1155m			G C_8N_7 + N_9H-C_4N_3	[11]
	1164s	1165m	1174w	1162w	A/G $\nu_s(C_5$-$C_6)$ C-C Stretching	[1, 2]
		1191w	1195m		C	[1,8]
		1207w			T ν_s(C-C) Ring-CH_3 Stretching	[1,2,7]
1216s		1219w		1217s	T in-plane ν_s(C–CH_3)	[1,4]
1235s		1230s	1230w		C	[11]
1259w	1252m	1249w	1264w		A $\delta(C_8$–H, N_9–H), $\nu(N_7$–$C_8)$ C ν_s(C-C) Ring-CH_3 Stretching G $\nu_s(C_8$–$N_9)$ C-N Stretching T In-plane ν(ring)	[1,2,4,5]
1275w	1278w	1286s			C ν_s(C–NH_2) + in-plane ν_s(ring) T Ring + CH [11] G C_8N_7-N_1C_6 + N_7C_5	[1,4,11]
1296w	1296s		1303m		C ν_s (C_2-N_3) C-N Stretching	[1,2,9]
	1324w	1312s		1312w	A ν (C_2–N_3, N_1–C_2, C_5–C_6, C_5–N_7) G ν_s (C-N) C-N Stretching (Im)	[2,4]
		1337s	1328w	1334w	A/G Ring mode	[1,6]
1344s			1343w		T N_3H-C_4=O	[11]
			1353s		G vs (C-N) C-N Stretching (py)	[2]
	1362s	1370w	1370w		A/C/T/G ν_s (C-N) C-N Stretching (py)	[1,2]
1383s			1386w		G C_2N_3-C_2	[11]

		1396s		1390w	T δ(NH) deformation δ(CH$_3$) CH$_3$ deformation	[1,2,4]
1427s		1432w	1417m	1410m	C	[11]
	1443m		1443w	1439w	T C$_5$-Me	[11]
1461w					A ν_s(C=N) C=N Stretching (Py) C$_2$H-N$_1$C$_2$ + N$_3$C$_2$ G N$_1$C$_2$-N$_1$C$_6$	[2,11]
	1477w				A ν_s(C=N) C=N Stretching (Py) T –N$_1$C$_2$ + C$_2$N$_3$	[1,2,11]
1488s			1488w		C N$_1$C$_6$ + N$_3$C$_4$	[11]
	1511s	1509s	1517s	1505s	C δ (NH$_2$) NH$_2$ Deformation G C$_4$C$_5$-C$_4$N$_9$	[1,2,11]
1543w	1546s	1541s	1539w		T in-plane ring stretching A Ring Stretching (Py)	[1,2]
1563m	1563s	1565s	1560s	1563m	A/C/G/T Ring Stretching (Py)	[1,2]
1581w			1580sw	1581m	A δ (NH$_2$) NH$_2$ Deformation C C$_4$C$_5$-C$_5$C$_6$ T N$_3$C$_4$+N$_1$C$_2$+C$_6$C$_5$-N$_1$C$_6$ G N$_3$C$_4$-C$_4$C$_5$	[2,11]
1596w	1596w	1591s	1609w		A/C/G δ(NH$_2$) NH$_2$ Deformation	[1,2,4,11]
	1641w	1632m	1637m	1621s	C/G/T ν_s (C=O) , ν_s (C=C)	[1,2,7]
	1659w			1658s	T C$_4$=O + C$_5$-C$_6$	[11]
1666w					A β_s(NH$_2$) NH$_2$ Scissoring	[1,2]

6.3.3   TERS Sensitivity of the Nanoplates

Figure 6.5 a-c shows TERS experiments with the tip located within the near-field of the sample and 100 nm above the surface of the sample (Far-field) for the three samples, namely plasmid-free cDNA, embedded cDNA in plasmid referred as cDNA, and pure plasmid. In the near-field spectra, a vibrational signature is collected for all the specimens, whereas in far-filed, no detectable peaks were observed. This supports the necessity of the tip to be located within the close surface of the sample to yield a reproducible signal-to-noise ratio. Noteworthy, the acquired spectra for plasmid-free cDNA and cDNA compared to plasmid are significantly stronger due to the lower density of nucleobases for plasmid.

As shown in **Figure 6.5 d-f**, the obtained signals of these three specimens are compared for both quartz and gold nanoplate substrates. As shown in **Figure 6.5 d-f**, the obtained signal of cDNA on quartz is quite similar to the quartz background signal without the presence of cDNA that suggests the lack of sensitivity of this approach When using the gold nanoplate in a gap-mode geometry, a clear spectrum of the cDNA t with strong signal-to-noise ratio is observable highlighting the importance of the functioning mode of TERS for a selected sample
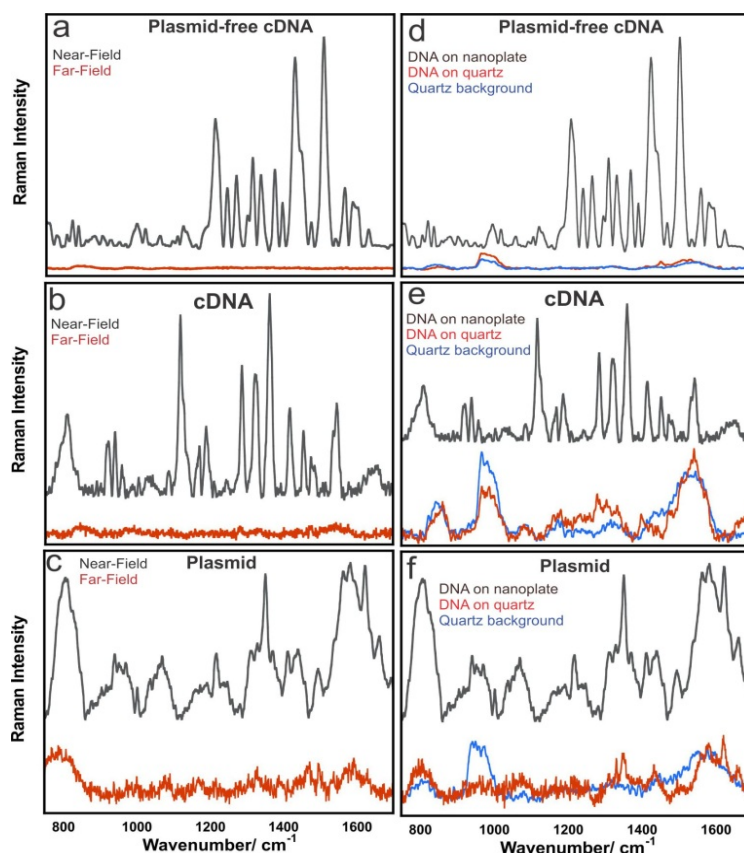
Figure 6.5 **TERS activity of the nanoplates for cDNA detection (a) TERS signal of plasmid-free cDNA on gold nanoplate in approach with tip (Near-field) and for retracted tip (Far-field); (b) TERS signal of embedded cDNA in plasmid on gold nanoplate in approach with tip (Near-field) and for retracted tip (Far-field); (c) TERS signal of plasmid on gold nanoplate in approach with tip (Near-field) and for retracted tip (Far-field); TERS signal of plasmid-free cDNA (d), embedded cDNA in plasmid (e), and plasmid (f) on gold nanoplate and quartz substrate along with background signal of the substrate.**

6.3.4 Towards Nucleic Acid Localization on cDNA Strand Probed by TERS

Based on the size of a nucleobase, a complete turn of a DNA is 3.4 nm ca. with 0.34 nm ca. distance between each adjacent nucleobase.[18] Considering the apex size of the tip used in this work to be 10 nm ca., ~25 nucleobases can be located under the tip during the signal acquisition. Due to this limitation, it might not be possible to ascertain the exact sequence of the cDNA at a specific location. However, one can estimate the prominent nucleobase(s) present in a specific sequence located under the tip.

For instance, in the case of the plasmid-free cDNA shown in **Figure 6. 2 d-g**, based on the dominant peaks indicated by asterisks, we can estimate the majority of the nucleobases present at those spots. As shown in **Figure 6. 2d**, spot 1, based on the selected peaks of 1210 (T), 1451 (A/G), and 1538 (T) cm^{-1}, Thymine is present with a higher content compared to other nucleobases. In spot 2 shown in Figure 6.3e, based on the selected peaks at 1345 (T), 1403(T), and 1468(A/T) cm^{-1}, the major density of nucleobases is also Thymine. For spot 3 shown in **Figure 6.2f** using major peaks of 1433(C), 1509(C/G), and 1577(A/C/T/G) cm^{-1}, the dominant nucleobase is Cytosine. In spot 4 shown in **Figure 6.2g**, based upon the peaks of 1240(G), 1423(C), and 1527(C/G) cm^{-1}, the majority includes Cytosine and Guanine distributed equally.

The same analysis can be conducted on the embedded cDNA in plasmid as shown in **Figure 6.4 d-g**. In spot 1 shown in **Figure 6.4d**, the peaks at 1157(G), 1344(T), and 1383(G) cm^{-1}, the major nucleobase present would be Thymine. In spot 2 shown in **Figure 6.4e**, the represented major peaks at 1417 (C), 1517(C/G), and 1581(A/C/G/T) cm^{-1}, the most dominant nucleobase would be Cytosine. In spot 3 of the cDNA shown in

Figure 6.4f, based on the most intense peaks of 1337 (A/G), 1511(C/G), and 1541(T/A) cm^{-1}, the major nucleobases present would be Adenine and Guanine with equal probability. The final point of spot 4 represents the major peaks of 1362(A/C/G/T), 1546(T/A), and 1596(A/C/G) cm^{-1}, offers the Adenine as the most present nucleobase at this spot.

6.3.5   Estimation of Enhancement Factor of TERS Measurements

The estimated enhancement factor (EF) for these biosamples was determined using the approach developed in Chapter 2. Using diameters of the irradiated areas of $d_L \cong 500$ nm for the far-field and $d_{tip} \cong 35$ nm for the near-field, and contrast factors for the Raman band at 1511 cm^{-1}, $C_{1511cm-1} = 309$ (with $I_{TERS} = 4948.58$ and $I_0 = 15.96$), this provides a crude enhancement factor of 6.3×10^5. Although this is a rough estimate, this valueis comparable to typical TERS enhancement values reported in the literature.[2,4]

6.4   Conclusion

In this work, plasmid DNA such β_2AR cDNA is investigated by TERS. First, AFM reveals morphological differences between plasmid-free cDNA compared to the embedded cDNA in plasmid. TERS is then employed to yield spatially resolved spectroscopic information of selected area of the DNA chains with an estimated resolution better than 10 nm in the best experiments. The collected TERS spectra are indicative of the distribution of the elementary bases (C, G, T, A) that can be estimated in selected region of the chains deposited onto a gold surface. This approach has great potential that can be further exploited in genomics studies. One question that may arise concerns the possibility to perform TERS in aqueous solution. Several work have been

published on the topic and demonstrate that TERS can technically be performed in physiological conditions.[30] In such approaches, the selection of the force constant of the tip and aqueous media will be of importance but yet should not lead to a better spatial resolution that is strictly limited by the size of the tip.

6.5   References

(1)   Sanger, F.; Nicklen, S.; Coulson, A. R., DNA sequencing with chain-terminating inhibitors. *Proc. Natl. Acad. Sci. U. S. A.* **1977**, *74*, 5463.

(2)   Dovichi, N. J., DNA sequencing by capillary electrophoresis. *Electrophoresis* **1997**, *18*, 2393.

(3)   Treffer, R.; Lin, X.; Bailo, E.; Deckert-Gaudig, T.; Deckert, V., Distinction of nucleobases – a tip-enhanced Raman approach. *Beilstein J. Nanotechnol.* **2011**, *2*, 628.

(4)   Maxam, A. M.; Gilbert, W., A new method for sequencing DNA. *Proc. Natl. Acad. Sci. U.S.A* **1977**, *74*, 560.

(5)   Treffer, R.; Deckert, V., Recent advances in single-molecule sequencing. *Curr. Opin. Biotech.* **2010**, *21*, 4.

(6)   Matthäus, C.; Bird, B.; Miljković, M.; Chernenko, T.; Romeo, M.; Diem, M. In *Methods in Cell Biology*; Dr. John, J. C., Dr. H. William Detrich, III, Eds.; Academic Press: 2008; Vol. Volume 89, p 275.

(7)   Domke, K. F.; Zhang, D.; Pettinger, B., Tip-Enhanced Raman Spectra of Picomole Quantities of DNA Nucleobases at Au(111). *J. Am. Chem. Soc.* **2007**, *129*, 6708.

(8)   Deckert-Gaudig, T.; Deckert, V., Nanoscale structural analysis using tip-enhanced Raman spectroscopy. *Curr. Opin. Chem. Biol.* **2011**, *15*, 719.

(9)   Rasmussen, A.; Deckert, V., Surface- and tip-enhanced Raman scattering of DNA components. *J. Raman Spectrosc.* **2006**, *37*, 311.

(10)   Lipiec, E.; Sekine, R.; Bielecki, J.; Kwiatek, W. M.; Wood, B. R., Molecular Characterization of DNA Double Strand Breaks with Tip-Enhanced Raman Scattering. *Angew. Chem., Int. Ed.* **2014**, *53*, 169.

(11)   Watanabe, H.; Ishida, Y.; Hayazawa, N.; Inouye, Y.; Kawata, S., Tip-enhanced near-field Raman analysis of tip-pressurized adenine molecule. *Phys. Rev. B* **2004**, *69*, 155418.

(12)   Bailo, E.; Deckert, V., Tip-Enhanced Raman Spectroscopy of Single RNA Strands: Towards a Novel Direct-Sequencing Method. *Angew. Chem. Int. Ed.* **2008**, *47*, 1658.

(13)   Johnson, R. P.; Richardson, J. A.; Brown, T.; Bartlett, P. N., A Label-Free, Electrochemical SERS-Based Assay for Detection of DNA Hybridization and Discrimination of Mutations. *J. Am. Chem. Soc.* **2012**, *134*, 14099.

(14)   Yang, Z.; Aizpurua, J.; Xu, H., Electromagnetic field enhancement in TERS configurations. *J. Raman Spectrosc.* **2009**, *40*, 1343.

(15)   Deckert-Gaudig, T.; Deckert, V., Ultraflat Transparent Gold Nanoplates—Ideal Substrates for Tip-Enhanced Raman Scattering Experiments. *Small* **2009**, *5*, 432.

(16)   Deckert-Gaudig, T.; Bailo, E.; Deckert, V., Tip-enhanced Raman scattering (TERS) of oxidised glutathione on an ultraflat gold nanoplate. *Phys. Chem. Chem. Phys.* **2009**, *11*, 7360.

(17)   Deckert-Gaudig, T.; Rauls, E.; Deckert, V., Aromatic Amino Acid Monolayers Sandwiched between Gold and Silver: A Combined Tip-Enhanced Raman and Theoretical Approach. *J. Phys. Chem. C* **2010**, *114*, 7412.

(18)   Kobilka, B. K.; Dixon, R. A. F.; Frielle, T.; Dohlman, H. G.; Bolanowski, M. A.; Sigal, I. S.; Yang-Feng, T. L.; Francke, U.; Caron, M. G.; Lefkowitz, R. J., cDNA for the human β2-adrenergic receptor: a protein with multiple membrane-spanning domains and encoded by a gene whose chromosomal location is shared with that of the receptor for platelet-derived growth factor. *Proc. Natl. Acad. Sci. U. S. A.* **1987**, *84*, 46.

(19)   Johnson, M., Molecular mechanisms of β2-adrenergic receptor function, response, and regulation. *J Allergy Clin Immunol* **2006**, *117*, 18.

(20)   Novotny, L.; Bian, R. X.; Xie, X. S., Theory of nanometric optical tweezers. *Phys. Rev. Lett.* **1997**, *79*, 645.

(21)   Treffer, R.; Lin, X.; Bailo, E.; Deckert-Gaudig, T.; Deckert, V., Distinction of nucleobases - a tip-enhanced Raman approach. *Beilstein J. Nanotechnol.* **2011**, *2*, 628.

(22)   Jang, N. H., The coordination chemistry of DNA nucleosides on gold nanoparticles as a probe by SERS. *Bull. Korean Chem. Soc.* **2002**, *23*, 1790.

(23)   Giese, B.; McNaughton, D., Surface-Enhanced Raman Spectroscopic and Density Functional Theory Study of Adenine Adsorption to Silver Surfaces. *J. Phys. Chem. B* **2002**, *106*, 101.

(24)   Badr, Y.; Mahmoud, M. A., Effect of silver nanowires on the surface-enhanced Raman spectra (SERS) of the RNA bases. *Spectrochim. Acta Mol. Biomol. Spectrosc.* **2006**, *63*, 639.

(25)   Ke, W.; Zhou, D.; Wu, J.; Ji, K., Surface-Enhanced Raman Spectra of Calf Thymus DNA Adsorbed on Concentrated Silver Colloid. *Appl. Spectrosc.* **2005**, *59*, 418.

(26)   Thomas, G. J.; Benevides, J. M.; Overman, S. A.; Ueda, T.; Ushizawa, K.; Saitoh, M.; Tsuboi, M., Polarized Raman spectra of oriented fibers of A DNA and B DNA: anisotropic and isotropic local Raman tensors of base and backbone vibrations. *Biophys. J.* **1995**, *68*, 1073.

(27)   Escobar, R.; Carmona, P.; Molina, M., Raman spectroscopic determination of thymidine nucleoside structures in nucleotides. *Analyst* **1996**, *121*, 105.

(28)   Green, M.; Liu, F.-M.; Cohen, L.; Kollensperger, P.; Cass, T., SERS platforms for high density DNA arrays. *Farad. Discuss.* **2006**, *132*, 269.

(29)   Otto, C.; van den Tweel, T. J. J.; de Mul, F. F. M.; Greve, J., Surface-enhanced Raman spectroscopy of DNA bases. *J. Raman Spectrosc.* **1986**, *17*, 289.

(30)   Schmid, T.; Yeo, B.-S.; Leong, G.; Stadler, J.; Zenobi, R., Performing tip-enhanced Raman spectroscopy in liquids. *J. Raman Spectrosc.* **2009**, *40*, 1392.

Chapter 7

7 Conclusions and Outlook

In the present thesis, we have introduced the concept of plasmon and surface plasmon resonance effects and their applications to tip-enhanced Raman spectroscopy. Tip-enhanced Raman spectroscopy technique was investigated on both theoretical and experimental aspects as a useful technique to study a variety of nanostructures. A considerable part of this PhD work dealt with the optimization and technical development of the TERS setup with the goal to achieve a higher spatial resolution of the nanoscale features along with a better surface specificity (Chapter 2). For this, we have selected the gap-mode TERS which requires the development of ultra-flat substrates onto which selected nanomaterial (graphene sheets), molecules (monolayer), biomaterial (DNA chain) were deposited. The sample being sandwiched between two metallic interfaces, larger field enhancements and confinement are enabling higher sensitivity and better spatial resolution. The ideal nanoplates used in this studied were gold nanoplates that have ideal dimensions for TERS applications. The synthesis of Ag nanoplates was also reported in Chapter 3, but we were not successful at making plates that are large enough for TERS experiments. This work is presently pursued in the Lagugné-Labarthet's group.

Chapters 4 to 6 are derived from manuscripts that are either published (Chapters 4, 5) or under preparation (Chapter 6). In particular we have investigated the polarization effect of the irradiation source by comparing the obtained spectra of a monolayer using Gaussian or Radial polarizations. We show remarkable effect that indicate that surface photochemical effect may occur yielding plasmon-mediated photoreduction of 4-NTP.

Such effect are strongly dependent on the tip-sample distance and vanish exponentially once the tip is brought far from the surface.[1]

In Chapter 5, few-layer graphene sheets have been investigated by TERS. Spatial resolution was an important criterion in differentiating the edges types of graphene flakes. Due to the large scattering cross section of graphene and in general carbon-containing materials, TERS was successfully used to probe few-layers graphene flakes deposited on gold nanoplates. Raman spectra and intensity ratio analysis of the D/G Raman modes provides valuable information to determine edge type and orientation of the graphene flakes. Sub-20 nm resolution was obtained upon these measurements but yet the reproducibility of these experiments was dependent on the tip activity.[2]

Finally, TERS technique was used to investigate of ultra-flat gold nanoplates on a quartz substrate to be used for characterization of β_2AR cDNA (Chapter 6). Owing to high topographical and spatial resolution accessible by TERS, this approach provides an ultra-sensitive promising tool for investigation of small bio-structures such as DNA and RNA. In addition, the optical resolution chemical information obtained clearly reveals details in the range of 8-20 nm, enabling the possibility to probe nanoscale biomolecules using a label-free and non-invasive method.

Future work and experimental developments can be done to push further the limit of detection down to the single molecule detection.[3] In this context, ultrahigh vacuum TERS (UHV-TERS) seems to be the next level of high resolution spectroscopy with a resolution allowing one to collect the Raman spectrum of a single molecule deposited onto a surface. The UHV conditions also prevent any oxidation processes of the metallic

tip, substrate or sample of interest and should also limit the presence of an interfacial layer of water. Actually with this combination, TERS studies on atomically clean surfaces are possible when carried out in ultrahigh vacuum.[4-7] In 2008, the first TERS measurement under UHV condition was reported by J. Steidtner and B. Pettinger.[8,9] Recently, spatial resolution of ~1 nm has been reported in UHV[4] and ~2 nm in ambient.[10] In a recent work, Wolf et al.[7] used UHV-TERS to study of graphene nanoribbons on Au(111) and observed significant blinking of the TERS signal of both the D- and G-band.[7] Similar methodology was performed recently by R.Van Duyne's research group[11] using picosecond (ps) UHV-TERS technique in an effort to acquire molecular resolution information. In this research they demonstrated the benefits of coupling of picosecond-pulsed irradiation with a UHV-TERS instrument as depicted in **Figure 7.1**.
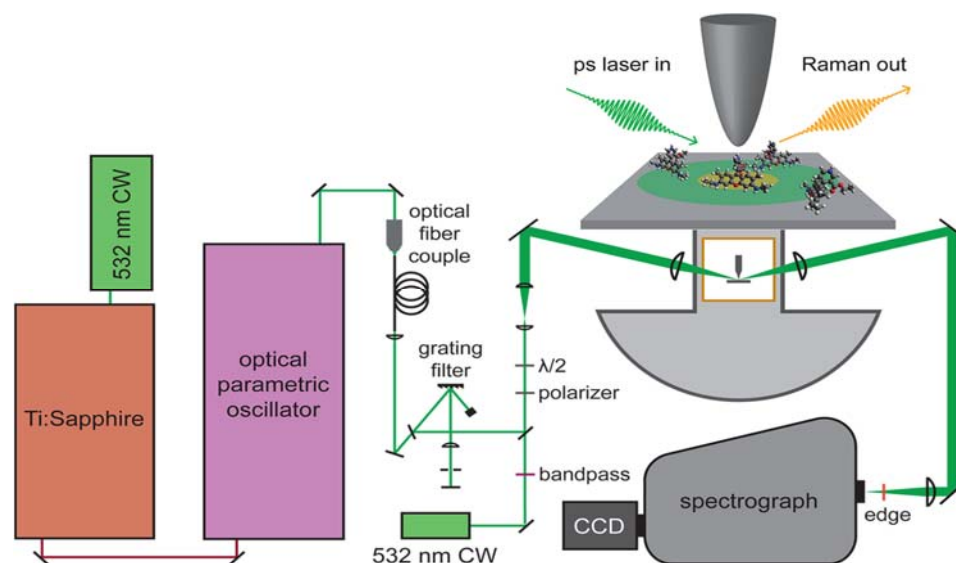
Figure 7.1 **Experimental setup of ps UHV-TERS. Laser source (532 nm) irradiation is coupled to the UHV instrument via an optical Fiber. The backscattered light from the sample gets collected and then enters the spectrometer. The image is adapted from reference 11 with permission from American Chemical Society.[11]**

Rhodamine 6G (R6G) was selected as the analyte due to its large resonant Raman cross section and compatibility with in situ-sublimation and also to benefit from electronic resonance effects using an excitation source that matches the absorption of the dye.

The development of UHV-TERS is still in progress and with further technical improvements in future, the ultrahigh sensitivity and spatial resolution of UHV-TERS method can provide information about some phenomena such as the catalysis processes, surface functionalization and organization.[12] Nevertheless, such setups are extremely complex to maintain and costly to acquire limiting their use to a few specialized research groups.

In conclusion, the use of metallic nanosized objects and more specifically the tailoring of their plasmonic properties reveals to be a fabulous source of improvements of spectroscopic techniques such as Raman spectroscopy but can also be valued for a wealth of other processes such as infrared spectroscopy,[13] fluorescence,[14] photo luminescence,[15] and nonlinear optical processes.[16] The local field-enhancement significantly improves sensitivities and spatial resolution well beyond the conventional limits of a classical optical measurement.

Specific to TERS, the reproducible fabrication of an active tip is a current challenge. The tip has to be stable in time, robust in use and with associated surface plasmon resonance that are tuned to a given excitation source for an efficient activity. Furthermore the localize surface plasmon must be excited with the proper polarization to yield larger enhancements.[17]

7.1   References

(1)   Pashaee, F.; Hou, R.; Gobbo, P.; Workentin, M. S.; Lagugne-Labarthet, F., Tip-Enhanced Raman Spectroscopy of Self-Assembled Thiolated Monolayers on Flat Gold Nanoplates Using Gaussian-Transverse and Radially Polarized Excitations. *J. Phys. Chem. C* **2013**, *117*, 15639.

(2)   Pashaee, F.; Sharifi, F.; Fanchini, G.; Lagugne-Labarthet, F., Tip-enhanced Raman spectroscopy of graphene-like and graphitic platelets on ultraflat gold nanoplates. *Phys. Chem. Chem. Phys.* **2015**, *17*, 21315.

(3)   Huang, T.-X.; Huang, S.-C.; Li, M.-H.; Zeng, Z.-C.; Wang, X.; Ren, B., Tip-enhanced Raman spectroscopy: tip-related issues. *Anal. Bioanal. Chem.* **2015**, *407*, 8177.

(4)   Zhang, R.; Zhang, Y.; Dong, Z. C.; Jiang, S.; Zhang, C.; Chen, L. G.; Zhang, L.; Liao, Y.; Aizpurua, J.; Luo, Y.; Yang, J. L.; Hou, J. G., Chemical mapping of a single molecule by plasmon-enhanced Raman scattering. *Nature (London, U. K.)* **2013**, *498*, 82.

(5)   Jiang, N.; Foley, E. T.; Klingsporn, J. M.; Sonntag, M. D.; Valley, N. A.; Dieringer, J. A.; Seideman, T.; Schatz, G. C.; Hersam, M. C.; Van Duyne, R. P., Observation of Multiple Vibrational Modes in Ultrahigh Vacuum Tip-Enhanced Raman Spectroscopy Combined with Molecular-Resolution Scanning Tunneling Microscopy. *Nano Lett.* **2012**, *12*, 5061.

(6)   Klingsporn, J. M.; Jiang, N.; Pozzi, E. A.; Sonntag, M. D.; Chulhai, D.; Seideman, T.; Jensen, L.; Hersam, M. C.; Duyne, R. P. V., Intramolecular Insight into Adsorbate-Substrate Interactions via Low-Temperature, Ultrahigh-Vacuum Tip-Enhanced Raman Spectroscopy. *J. Am. Chem. Soc.* **2014**, *136*, 3881.

(7)   Shiotari, A.; Kumagai, T.; Wolf, M., Tip-Enhanced Raman Spectroscopy of Graphene Nanoribbons on Au(111). *J. Phys. Chem. C* **2014**, *118*, 11806.

(8)   Steidtner, J.; Pettinger, B., High-resolution microscope for tip-enhanced optical processes in ultrahigh vacuum. *Rev. Sci. Instrum.* **2007**, *78*, 103104/1.

(9)   Steidtner, J.; Pettinger, B., Tip-Enhanced Raman Spectroscopy and Microscopy on Single Dye Molecules with 15 nm Resolution. *Phys. Rev. Lett.* **2008**, *100*, 236101/1.

(10)   Chen, C.; Hayazawa, N.; Kawata, S., A 1.7 nm resolution chemical analysis of carbon nanotubes by tip-enhanced Raman imaging in the ambient. *Nat.Commun.* **2014**, *5*, 3312.

(11)   Pozzi, E. A.; Sonntag, M. D.; Jiang, N.; Chiang, N.; Seideman, T.; Hersam, M. C.; Van Duyne, R. P., Ultrahigh Vacuum Tip-Enhanced Raman Spectroscopy with Picosecond Excitation. *J. Phys. Chem. Lett.* **2014**, *5*, 2657.

(12)   Sonntag, M. D.; Pozzi, E. A.; Jiang, N.; Hersam, M. C.; Van Duyne, R. P., Recent Advances in Tip-Enhanced Raman Spectroscopy. *J. Phys. Chem. Lett.* **2014**, *5*, 3125.

(13)   Brown, L. V.; Yang, X.; Zhao, K.; Zheng, B. Y.; Nordlander, P.; Halas, N. J., Fan-Shaped Gold Nanoantennas above Reflective Substrates for Surface-Enhanced Infrared Absorption (SEIRA). *Nano Letters* **2015**, *15*, 1272.

(14)   Volkov, I. L.; Ramazanov, R. R.; Ubyivovk, E. V.; Rolich, V. I.; Kononov, A. I.; Kasyanenko, N. A., Fluorescent silver nanoclusters in condensed DNA. *Chemphyschem* **2013**, *14*, 3543.

(15)   Ogawa, Y.; Katayama, K.; Minami, F., Tip-enhanced rayleigh scattering and photoluminescence from semiconductor nanoparticles. *J. Nanosci. Nanotechnol.* **2011**, *11*, 11055.

(16)   Trinh, D. T.; Mayer, L.; Hajj, B.; Lautru, J.; Zyss, J.; Shynkar, V., Full determination of single ferroelectric nanocrystal orientation by Pockels electro-optic microscopy. *Applied Optics* **2015**, *54*, 3412.

(17)   Taguchi, A.; Yu, J.; Verma, P.; Kawata, S., Optical antennas with multiple plasmonic nanoparticles for tip-enhanced Raman microscopy. *Nanoscale* **2015**, *7*, 17424.

Appendix A.

Copyrights

Copyright Clearance Center RightsLink®

Home   Account Info   Help

ACS Publications
Most Trusted. Most Cited. Most Read.

Title: Tip-Enhanced Raman Spectroscopy of Self-Assembled Thiolated Monolayers on Flat Gold Nanoplates Using Gaussian-Transverse and Radially Polarized Excitations

Author: Farshid Pashaee, Renjie Hou, Pierangelo Gobbo, et al

Publication: The Journal of Physical Chemistry C

Publisher: American Chemical Society

Date: Aug 1, 2013

Copyright © 2013, American Chemical Society

Title: Tip-enhanced Raman spectroscopy of graphene-like and graphitic platelets on ultraflat gold nanoplates

Author: Farshid Pashaee,Faranak Sharifi,Giovanni Fanchini,François Lagugné-Labarthet

Publication: Physical Chemistry Chemical Physics

Publisher: Royal Society of Chemistry

Date: Feb 10, 2015

Copyright © 2015, Royal Society of Chemistry

Order Completed

Thank you for your order.

This Agreement between farshid pashaee ("You") and Royal Society of Chemistry ("Royal Society of Chemistry") consists of your license details and the terms and conditions provided by Royal Society of Chemistry and Copyright Clearance Center.

Your confirmation email will contain your order number for future reference.

Get the printable license.

License Number	3771010802689
License date	Dec 16, 2015
Licensed Content Publisher	Royal Society of Chemistry
Licensed Content Publication	Physical Chemistry Chemical Physics
Licensed Content Title	Tip-enhanced Raman spectroscopy of graphene-like and graphitic platelets on ultraflat gold nanoplates
Licensed Content Author	Farshid Pashaee,Faranak Sharifi,Giovanni Fanchini,François Lagugné-Labarthet
Licensed Content Date	Feb 10, 2015
Licensed Content Volume	17
Licensed Content Issue	33
Type of Use	Thesis/Dissertation
Requestor type	academic/educational
Portion	figures/tables/images
Number of figures/tables/images	1
Distribution quantity	1
Format	print and electronic
Will you be translating?	no
Order reference number	None
Title of the thesis/dissertation	VIBRATIONAL IMAGING AT THE NANOSCALE: SURPASSIN THE DIFFRACTION LIMIT USING TIP-ENHANCED RAMAN SPECTROSCOPY
Expected completion	Dec 2015

Annual Review of Physical Chemistry

Order detail ID: 68771422
ISBN: 9780824310578
Publication Type: Book
Publisher: Annual Reviews

Permission Status: ✅ Granted

Permission type: Republish or display content
Type of use: Republish in a thesis/dissertation
Order License Id: 3736620743123

⊟ Hide details

Requestor type	Not-for-profit entity
Format	Print, Electronic
Portion	image/photo
Number of images/photos requested	1
Title or numeric reference of the portion(s)	fig14.Near-field Raman imaging of single-walled carbon nanotubes (a). This image was recorded by raster-scanning the sample underneath a laser-irradiated metal tip and integrating, for each image pixel, the photon counts that fall into a narrow spectral band-width centered around the G-line at
Title of the article or chapter the portion is from	NEAR-FIELDOPTICAL MICROSCOPY AND SPECTROSCOPY WITH POINTED PROBE
Editor of portion(s)	Annual Reviews
Author of portion(s)	Lukas Novotny and Stephan J. Stranick
Volume of serial or monograph	57
Page range of portion	303-331
Publication date of portion	2006
Rights for	Main product
Duration of use	Life of current edition
Creation of copies for the disabled	no
With minor editing privileges	no
For distribution to	Canada

ROYAL SOCIETY OF CHEMISTRY LICENSE
TERMS AND CONDITIONS

Oct 21, 2015

This is a License Agreement between farshid pashaee ("You") and Royal Society of Chemistry ("Royal Society of Chemistry") provided by Copyright Clearance Center ("CCC"). The license consists of your order details, the terms and conditions provided by Royal Society of Chemistry, and the payment terms and conditions.

All payments must be made in full to CCC. For payment instructions, please see information listed at the bottom of this form.

License Number	3733810409647
License date	Oct 21, 2015
Licensed content publisher	Royal Society of Chemistry
Licensed content publication	Chemical Society Reviews
Licensed content title	Tip-enhanced Raman scattering
Licensed content author	Elena Bailo,Volker Deckert
Licensed content date	Mar 31, 2008
Volume number	37
Issue number	5
Type of Use	Thesis/Dissertation
Requestor type	academic/educational
Portion	figures/tables/images
Number of figures/tables/images	1
Format	print and electronic
Distribution quantity	5
Will you be translating?	no
Order reference number	None
Title of the thesis/dissertation	VIBRATIONAL IMAGING AT THE NANOSCALE: SURPASSIN THE DIFFRACTION LIMIT USING TIP-ENHANCED RAMAN SPECTROSCOPY
Expected completion date	Dec 2015
Estimated size	180
Total	0.00 CAD

Terms and Conditions

This License Agreement is between {Requestor Name} ("You") and The Royal Society of Chemistry ("RSC") provided by the Copyright Clearance Center ("CCC"). The license consists of your order details, the terms and conditions provided by the Royal Society of Chemistry, and the payment terms and conditions.

RSC / TERMS AND CONDITIONS

Beilstein-Institut Copyright and License Agreement

In submitting a research article ('article') to a journal published by Beilstein-Institut ('Beilstein') I certify that:

1. I am authorized by my co-authors to enter into these arrangements.

2. I warrant, on behalf of myself and my co-authors, that:

   a. the article is original, has not been formally published in any other journal or book, is not under consideration by any other journal or book, except degree dissertation, and does not infringe any existing copyright or any other third party rights;

   b. I am/we are the sole author(s) of the article and have full authority to enter into this agreement and in granting rights to Beilstein are not in breach of any other obligation. If the law requires that the article be published in the public domain, I/we will notify Beilstein at the time of submission upon which clauses 3 through 6 of the Beilstein-Institut Open Access License Agreement do not apply;

   c. the article contains nothing that is unlawful, libellous, or which would, if published, constitute a breach of contract or of confidence or of commitment given to secrecy;

   d. I/we have taken due care to ensure the integrity of the article. To my/our - and currently accepted scientific - knowledge all statements contained in it purporting to be facts are true and any formula or instruction contained in the article will not, if followed accurately, cause any injury, illness or damage to the user.

3. I am aware that this Agreement is governed by the laws of the Federal Republic of Germany. Exclusive place of jurisdiction for all disputes arising from or in connection with this Agreement is Frankfurt am Main.

And I agree to the following license agreement:

Beilstein-Institut Open Access License Agreement

Brief summary of the agreement

Anyone is free:

- to copy, distribute, and display the work;
- to make derivative works;
- to make commercial use of the work;

BEILSTEIN INSTITUT

2. Fair Use Rights

Nothing in this license is intended to reduce, limit, or restrict any rights arising from fair use, first sale or other limitations on the exclusive rights of the copyright owner under copyright law or other applicable laws.

3. License Grant

Subject to the terms and conditions of this License, Licensor hereby grants You a worldwide, royalty-free, non-exclusive, perpetual (for the duration of the applicable copyright) license to exercise the rights in the Work as stated below:

a. to reproduce the Work, to incorporate the Work into one or more Collective Works, and to reproduce the Work as incorporated in the Collective Works;

b. to create and reproduce Derivative Works;

c. to distribute copies or phonorecords of, display publicly, perform publicly, and perform publicly by means of a digital audio transmission the Work including as incorporated in Collective Works;

d. to distribute copies or phonorecords of, display publicly, perform publicly, and perform publicly by means of a digital audio transmission Derivative Works;

e. For the avoidance of doubt, where the work is a musical composition:

i. **Performance Royalties Under Blanket Licenses.** Licensor waives the exclusive right to collect, whether individually or via a performance rights society (e.g. ASCAP, BMI, SESAC), royalties for the public performance or public digital performance (e.g. webcast) of the Work.

ii. **Mechanical Rights and Statutory Royalties.** Licensor waives the exclusive right to collect, whether individually or via a music rights agency or designated agent (e.g. Harry Fox Agency), royalties for any phonorecord You create from the Work ("cover version") and distribute, subject to the compulsory license created by 17 USC Section 115 of the US Copyright Act (or the equivalent in other jurisdictions).

f. **Webcasting Rights and Statutory Royalties.** For the avoidance of doubt, where the Work is a sound recording, Licensor waives the exclusive right to collect, whether individually or via a performance-rights society (e.g. SoundExchange), royalties for the public digital performance (e.g. webcast) of the Work, subject to the compulsory license created by 17 USC Section 114 of the US Copyright Act (or the equivalent in other jurisdictions).

The above rights may be exercised in all media and formats whether now known or hereafter devised. The above rights include the right to make such modifications as are technically necessary to exercise the rights in other media and formats. All rights not expressly granted by Licensor are hereby reserved.

4. Restrictions

The license granted in Section 3 above is expressly made subject to and limited by the following restrictions:

a. You may distribute, publicly display, publicly perform, or publicly digitally perform the Work only under the terms of this License, and You must include a copy of, or the Uniform Resource Identifier for, this License with every copy or phonorecord of the Work You distribute, publicly display, publicly perform, or publicly digitally perform. You may not offer or impose any terms on the Work that alter or restrict the terms of this License or the

recipients' exercise of the rights granted hereunder. You may not sublicense the Work. You must keep intact all notices that refer to this License and to the disclaimer of warranties. You may not distribute, publicly display, publicly perform, or publicly digitally perform the Work with any technological measures that control access or use of the Work in a manner inconsistent with the terms of this License Agreement. The above applies to the Work as incorporated in a Collective Work, but this does not require the Collective Work apart from the Work itself to be made subject to the terms of this License. If You create a Collective Work, upon notice from any Licensor You must, to the extent practicable, remove from the Collective Work any reference to such Licensor or the Original Author, as requested. If You create a Derivative Work, upon notice from any Licensor You must, to the extent practicable, remove from the Derivative Work any reference to such Licensor or the Original Author, as requested.

b. If you distribute, publicly display, publicly perform, or publicly digitally perform the Work or any Derivative Works or Collective Works, You must keep intact all copyright notices for the Work and give the Original Author credit reasonable to the medium or means You are utilizing by conveying the name (or pseudonym if applicable) of the Original Author if supplied; the title of the Work if supplied; to the extent reasonably practicable, the Uniform Resource Identifier, if any, that Licensor specifies to be associated with the Work, unless such URI does not refer to the copyright notice or licensing information for the Work; and in the case of a Derivative Work, a credit identifying the use of the Work in the Derivative Work (e.g., "French translation of the Work by Original Author," or "Screenplay based on original Work by Original Author"). Such credit may be implemented in any reasonable manner; provided, however, that in the case of a Derivative Work or Collective Work, at a minimum such credit will appear where any other comparable authorship credit appears and in a manner at least as prominent as such other comparable authorship credit.

5. Representations, Warranties and Disclaimer

UNLESS OTHERWISE MUTUALLY AGREED TO BY THE PARTIES IN WRITING, LICENSOR OFFERS THE WORK AS-IS AND MAKES NO REPRESENTATIONS OR WARRANTIES OF ANY KIND CONCERNING THE WORK, EXPRESS, IMPLIED, STATUTORY OR OTHERWISE, INCLUDING, WITHOUT LIMITATION, WARRANTIES OF TITLE, MERCHANTIBILITY, FITNESS FOR A PARTICULAR PURPOSE, NONINFRINGEMENT, OR THE ABSENCE OF LATENT OR OTHER DEFECTS, ACCURACY, OR THE PRESENCE OF ABSENCE OF ERRORS, WHETHER OR NOT DISCOVERABLE. SOME JURISDICTIONS DO NOT ALLOW THE EXCLUSION OF IMPLIED WARRANTIES, SO SUCH EXCLUSION MAY NOT APPLY TO YOU.

6. Limitation on Liability

EXCEPT TO THE EXTENT REQUIRED BY APPLICABLE LAW, IN NO EVENT WILL LICENSOR BE LIABLE TO YOU ON ANY LEGAL THEORY FOR ANY SPECIAL, INCIDENTAL, CONSEQUENTIAL, PUNITIVE OR EXEMPLARY DAMAGES ARISING OUT OF THIS LICENSE OR THE USE OF THE WORK, EVEN IF LICENSOR HAS BEEN ADVISED OF THE POSSIBILITY OF SUCH DAMAGES.

7. Termination

a. This License and the rights granted hereunder will terminate automatically upon any breach by You of the terms of this License. Individuals or entities who have received Derivative Works or Collective Works from You under this License, however, will not have their licenses terminated provided such individuals or entities remain in full compliance with those licenses. Sections 1, 2, 5, 6, 7, and 8 will survive any termination of this License.

BEILSTEIN INSTITUT

b. Subject to the above terms and conditions, the license granted here is perpetual (for the duration of the applicable copyright in the Work). Notwithstanding the above, Licensor reserves the right to release the Work under different license terms or to stop distributing the Work at any time; provided, however that any such election will not serve to withdraw this License (or any other license that has been, or is required to be, granted under the terms of this License), and this License will continue in full force and effect unless terminated as stated above.

8. Miscellaneous

a. Each time You distribute or publicly digitally perform the Work or a Collective Work, the Licensor offers to the recipient a license to the Work on the same terms and conditions as the license granted to You under this License.

b. Each time You distribute or publicly digitally perform a Derivative Work, Licensor offers to the recipient a license to the original Work on the same terms and conditions as the license granted to You under this License.

c. If any provision of this License is invalid or unenforceable under applicable law, it shall not affect the validity or enforceability of the remainder of the terms of this License, and without further action by the parties to this agreement, such provision shall be reformed to the minimum extent necessary to make such provision valid and enforceable.

d. No term or provision of this License shall be deemed waived and no breach consented to unless such waiver or consent shall be in writing and signed by the party to be charged with such waiver or consent.

e. This License constitutes the entire agreement between the parties with respect to the Work licensed here. There are no understandings, agreements or representations with respect to the Work not specified here. Licensor shall not be bound by any additional provisions that may appear in any communication from You. This License may not be modified without the mutual written agreement of the Licensor and You.

Copyright Clearance Center

RightsLink®

ACS Publications
Most Trusted. Most Cited. Most Read.

Title: Label-Free Mapping of Osteopontin Adsorption to Calcium Oxalate Monohydrate Crystals by Tip-Enhanced Raman Spectroscopy

Author: Nastaran Kazemi-Zanjani, Honghong Chen, Harvey A. Goldberg, et al

Publication: Journal of the American Chemical Society

Publisher: American Chemical Society

Date: Oct 1, 2012

Copyright © 2012, American Chemical Society

PERMISSION/LICENSE IS GRANTED FOR YOUR ORDER AT NO CHARGE

Hi Farshid,

Yes, you have permission to use that image in your work. However, make sure to write "Image courtesy of Erik Martinsson, Linköping University"

Good luck with finalizing your thesis.

Best,
Erik Martinsson

FP **Farshid Pashaee**   ↩ Reply all | ⌄
1
                                                                                Fri 10/23/2015 2:08 PM
Sent Items

hi
I am farshid pashaee, PhD candidate at chemistry department of Western university of Canada.This email is to acquire the permission to use an adapted version of "Fig 1: Localized surface plasmon resonance (LSPR)" a in your web page (https://www.ifm.liu.se/applphys/molphys/research/biosensing_using_nanopart/index.xml)

I will use that in my Ph.D thesis with this permission.

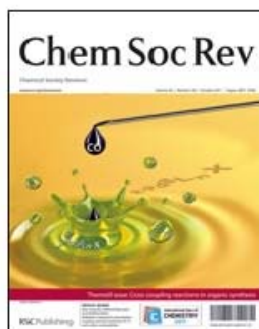I appreciate if you accept my request

best regard

farshid

Chem Soc Rev

Title: Molecularly-mediated assemblies of plasmonic nanoparticles for Surface-Enhanced Raman Spectroscopy applications
Author: Luca Guerrini, Duncan Graham
Publication: Chemical Society Reviews
Publisher: Royal Society of Chemistry
Date: Jul 26, 2012
Copyright © 2012, Royal Society of Chemistry

Order Completed

Thank you very much for your order.

Get the printable license.

License Number	3734940886499
License date	Oct 23, 2015
Licensed content publisher	Royal Society of Chemistry
Licensed content publication	Chemical Society Reviews
Licensed content title	Molecularly-mediated assemblies of plasmonic nanoparticles for Surface-Enhanced Raman Spectroscopy applications
Licensed content author	Luca Guerrini, Duncan Graham
Licensed content date	Jul 26, 2012
Volume number	41
Issue number	21
Type of Use	Thesis/Dissertation
Requestor type	academic/educational
Portion	figures/tables/images
Number of figures/tables/images	1
Distribution quantity	3
Format	print and electronic
Will you be translating?	no
Order reference number	None
Title of the thesis/dissertation	VIBRATIONAL IMAGING AT THE NANOSCALE: SURPASSIN THE DIFFRACTION LIMIT USING TIP-ENHANCED RAMAN SPECTROSCOPY
Expected completion date	Dec 2015
Estimated size	200
Total	0.00 USD

RightsLink

Title:	Compact metal probes: A solution for atomic force microscopy based tip-enhanced Raman spectroscopy
Author:	R. D. Rodriguez,E. Sheremet,S. Müller, et al.
Publication:	Review of Scientific Instruments
Volume/Issue	83/12
Publisher:	AIP Publishing LLC
Date:	Dec 19, 2012
Page Count:	8

Rights managed by AIP Publishing LLC.

Order Completed

Thank you very much for your order.

Click here for Payment Terms and Conditions.

Get a printable version for your records.

License Number	3735631213766
Order Date	Oct 24, 2015
Publisher	AIP Publishing LLC
Publication	Review of Scientific Instruments
Article Title	Compact metal probes: A solution for atomic force microscopy based tip-enhanced Raman spectroscopy
Author	R. D. Rodriguez,E. Sheremet,S. Müller, et al.
Online Publication Date	Dec 19, 2012
Volume number	83
Issue number	12
Type of Use	Thesis/Dissertation
Requestor type	Student
Format	Print and electronic
Portion	Figure/Table
Number of figures/tables	1
Title of your thesis / dissertation	VIBRATIONAL IMAGING AT THE NANOSCALE: SURPASSIN THE DIFFRACTION LIMIT USING TIP-ENHANCED RAMAN SPECTROSCOPY
Expected completion date	Dec 2015
Estimated size (number of pages)	200
Total	0.00 CAD

Curriculum Vitae

Name:	Farshid Pashaee
Post-secondary Education and Degrees:	K. N. Tousi University Tehran, Iran **2006-2008** M.Sc. Analytical Chemistry
	Mohaghegh University Ardabil, Iran **2002-2006** B.Sc. Chemistry
Honours and Awards:	first Prize for Poster Presentation in 5th Nanotechnology Student Conference- Tehran, Iran 2008
	Western Graduate Research Scholarship 2011-2015
Related Work Experience	Teaching Assistant The University of Western Ontario 2011-2015

Publications:

1. Pashaee F.; Tabatabaei M.; Caetano F.A.; Ferguson S.S and François Lagugné-Labarthet. 2016, in preparation.

2. Pashaee F.; Sharifi F.; Fanchini G. and François Lagugné-Labarthet, *Phys. Chem. Chem. Phys,* **2015**, 17, 21315

3. Wallace G. Q, Pashaee F, Hou R, Tabatabaei M, Lagugné-Labarthet F, *Proc. SPIE*, **2014**, 9126, 912610.

3. Pashaee F.; Hou R.; Gobbo P.; Workentin M.; Lagugne-Labarthet F.; *J. Phys. Chem. C*, **2013**,117, 15639

4. Kazemi-Zanjani N.; Pashaee F.; Lagugné-Labarthet F.; *Proc.SPIE*, **2012** 8412, 8412201.

5. Mostafavi M, Mohajeri A, A. Rouhollahi A, Adibi M, Pashaee F, Piryaei M.; *Asian J. Chem,* **2011**, 23, 5356.

6. Mostafavi M, Mohajeri A, A. Rouhollahi A, Adibi M, <u>Pashaee F</u>, Piryaei M.; *Asian J. Chem*, **2011**, 23, 5247.

7. Tabeshnia M, Rashvandavei M, Amini R, <u>Pashaee F</u>.; *J. Electroanal. Chem*, **2010**, 647, 181.

Seminars & Conferences

1. F. Pashaee, F. Sharifi, G. Fanchini, F. Lagugné-Labarthet, 98th Canadian Chemistry Conference, Ottawa, ON, Canada. June 2015 [Oral]

2. F. Pashaee, M. Tabatabaei, F. A. Caetano, S.S. G. Ferguson, and F. Lagugné-Labarthet, 98th Canadian Chemistry Conference, Ottawa, ON, Canada. June 2015 [Poster]

3. F. Pashaee, F. Sharifi, G. Fanchini, F. Lagugné-Labarthet, 6th Nano Ontario Conference. University of Windsor, Windsor, ON, Canada. November 2014 [Poster]

4. F. Pashaee, P. Gobbo, M. Workentin and F. Lagugné-Labarthet, 3rd CAMBR Distinguished Lecturer and Research Day, Centre for Advanced Materials and Biomaterials Research (CAMBR), Western University, London, ON, Canada. November 2013 [Poster]

5. F. Pashaee, P. Gobbo, M. Workentin and F. Lagugné-Labarthet, Western University Surface Canada Conference, London, ON, Canada. May 2013 [Oral]

6. F. Pashaee, P. Gobbo, M. Workentin and F. Lagugné-Labarthet, Western University. 24th Canadian Materials Science Conference (CMSC). London, ON, Canada. June 2012 [Poster]

7. F. Pashaee, M. Mostafavi, A. Mohajeri, A. Rouhollahi, K. N. Toosi University of Technology ”- 2nd International Congress on Nanoscience and Nanotechnology (ICNN), University of Tabriz in cooperation with the Iranian Nano Society (INS). University of Tabriz, Iran October 2008 [Poster].

8. F. Pashaee, M. Mostafavi, A. Mohajeri, A. Rouhollahi, K. N. Toosi University of Technology, 6th Aegean Analytical Chemistry Days (AACD2008), Denizli, Turkey. October 2008 [Poster]